# Brain Response to Overpressure and Recoil Loads from Discharge of Long-Range Precision Rifle

**by**

**Javier A. Maldonado-Echeverria**

A thesis

presented to the University of Waterloo

in fulfillment of the

thesis requirement for the degree of

Master of Applied Science

in

Mechanical and Mechatronics Engineering

Waterloo, Ontario, Canada, 2024

## Author's Declaration

I hereby declare that I am the sole author of this thesis. This is a true copy of the thesis, including any required final revisions, as accepted by my examiners.

I understand that my thesis may be made electronically available to the public.

# Abstract

The presence of concussion-like symptoms related to overpressure exposure and recoil forces from long-range precision rifle (LPR) training has been reported in the literature. However, the recoil head kinematics, overpressure loadings from LPR discharge, and the interaction of the two load paths have not been previously quantified.

In the present study, experiments were undertaken by the Defense Research and Development Canada (DRDC) Valcartier Research Centre, using an instrumented head form to measure the overpressure from LPR discharges and to measure head kinematics resulting from recoil using instrumented mouthguards on human volunteers. The measurements included a high-speed video to enable estimation of the relative onset timings of overpressure and recoil head kinematics. The LPR configurations encompassed both muzzle suppressor and non-suppressor configurations. Then, planar finite element (FE) head models (in the sagittal and transverse planes) were used to quantify the effects of the measured loadings on the brain response. The models were used to simulate three boundary conditions: only the overpressure, only the recoil head kinematics, and combining the two loadings to investigate the interaction of the load paths.

The overpressure resulting from discharge of the LPR was reduced significantly when the suppressor configuration was employed. The overpressure reached the head 3.6 ms after exiting the barrel of the LPR, with peaks ranging from 0.2 to 27.6 kPa with and without suppressor, respectively. The onset of recoil head kinematics varied between operators, occurring between 7.4 to 24.4 ms after the onset of overpressure loading to the head.

In addition, the FE models showed that the intracranial pressure response predicted in the head demonstrated an interaction between overpressure and head kinematics, while strain in the brain was largely governed by recoil head kinematics.

The results of this study provide important information regarding the relative severities and interaction between the overpressure and recoil head kinematics in LPR operators.

## Acknowledgments

The author gratefully acknowledges research funding from the Natural Sciences and Engineering Research Council of Canada, Defence Research and Development Canada, Valcartier Research Centre, Kapsul and Voxel.AI, and the Digital Research Alliance of Canada for computational resources. This research was undertaken, in part, thanks to funding from the Canada Research Chairs Program.

## Dedication

To my dearest parents and my sister, whose unwavering support, encouragement, and boundless love have been my guiding light throughout this academic journey. Your belief in my potential has fueled my determination.

To my esteemed professor, whose guidance, expertise, and insightful mentorship have shaped my intellectual growth. Your wisdom and dedication have been invaluable.

To my sponsor, Mr. Jorge Buitrago, whose generosity and belief in my aspirations made this pursuit possible.

This achievement stands as a testament to the collective belief and encouragement I've received from each of you. With heartfelt gratitude, I dedicate this thesis to you all.

# Table of Contents

# List of Figures

# List of Table

# 1. Introduction and Motivation

The firing of Long-Range Precision Rifles (LPRs) can have discernible repercussions on the operator, including resulting head kinematics (Ouellet & St-Onge, 2021) and exposure to overpressure (Ouellet & Philippens, 2018). Moreover, there is a documented association between LPR discharges and the manifestation of concussion symptoms (Skotak et al., 2019), which can also be observed in other contexts, such as instances of head impacts (head kinematics) (Tierney, 2021) and exposure to blast (overpressure) (Shires et al., 2020).

The head kinematics resulting from the discharge of LPRs are directly linked to the recoil forces experienced during the discharge. Specifically, a prior investigation (Ouellet & St-Onge, 2021) has indicated the presence of linear accelerations and rotational velocities at levels approximating 20-100 $m/s^2$ and 1-6 rad/s, respectively. It is important to note that these recorded head acceleration values fall below recognized thresholds for causing brain injuries (Gabler et al., 2016), but the repetitive discharges have potential cumulative effects (L. E. Miller et al., 2021).

Overpressure arises as a consequence of the discharge process due to the expulsion of gases from the muzzle (Hazell, 2021). The levels of overpressure generated by this gas expulsion are subject to stringent manufacturing standards aimed at constraining them below established thresholds associated with the safety of the operator (HEADQUARTERS, 1994). Nevertheless, it is noteworthy that the potential ramifications of the combined influence of overpressure and head kinematics, particularly within the framework of manufacturing standards, have not been comprehensively examined.

Common concussion symptoms that may be associated with sniper shots or similar events include (Mathews et al., 2020) headaches, dizziness, nausea, ringing in the ears, difficulty concentrating, and fatigue. Notably, prior research has specifically identified a correlation between LPR discharges and the occurrence of concussion symptoms during training sessions (Nakashima et al., 2022), particularly when operators engage in firing sequences of up to 15 consecutive rounds (HEADQUARTERS, 1994).

Concussion symptoms can result from the significant energy transferred to the head due to the recoil and overpressure generated by high-powered firearms like LPRs (Koptyug & Ainegren,

2015; Pal & Mitra, 2021). The specific symptoms experienced can vary depending on several factors, including the proximity to the discharge, the type of firearm, and the use of protective gear (e.g., suppressors) (M. R. Miller et al., 2022; Woodall et al., 2023).

It is worth emphasizing that the relationship between the effects of LPR discharges, encompassing head kinematics and overpressure, and the emergence of concussive symptoms (brain response) can be investigated through the application of finite element (FE) models to calculate this brain response (Corrales et al., 2020; Lyu et al., 2022; Seeburrun et al., 2023; Singh & Cronin, 2019, 2017). The response of the brain to head kinematics has been investigated using FE models of head impacts, establishing a correlation between head accelerations and rotational velocities with the manifestation of brain injury symptoms (Seeburrun et al., 2023). These FE models evaluate the brain response by employing metrics (Takhounts, Craig, Moorhouse, Mcfadden, et al., 2013) such as Maximum Principal Strain (MPS) or cumulative strain damage measure (CSDM).

The brain response to overpressure has been assessed by quantifying Intracranial Pressure (ICP) using FE models (Gabler et al., 2016b; Singh et al., 2014). These FE models predominantly target the consequences of high-level overpressures (blast events), revealing a distinct correlation between ICP levels and brain injury. It is crucial to emphasize that ICP can manifest as either positive or negative, with both manifestations affecting the brain. While the positive (compressive) ICP is associated with structural damage to the brain due to deformation (Lyu et al., 2022), the negative ICP may be linked to brain injury resulting from cavitation (Panzer et al., 2012).

The head kinematics and overpressure resulting from the discharge of LPR have not received the same level of investigation as head impacts and blast events, even though repeated exposures may lead to concussion symptoms. Consequently, this master's thesis was dedicated to measuring the head kinematics and overpressure generated by LPR discharges under various conditions and simulating the brain response to these measurements.

# 2. Background

This section serves to establish the theoretical foundation to study the risk of concussive symptoms induced by the discharge of the LPR through the application of FE analysis. To comprehensively address the necessary physical and computational knowledge, the background encompasses the recoil forces and overpressure produced by the LPR, the manifestation of concussive symptoms following its discharge, the FE models employed for simulating brain response, and the metrics essential for evaluating this brain response.

## 2.1. Recoil forces and overpressure resulting from LPR discharge.

A LPR is used for accuracy at extended distances and characterized by a caliber exceeding 0.3 inches. When these LPR are designed, both recoil and overpressure effects are important considerations due to their possible effects over the health of the operator (Béres & Kovács, 2022). Moreover, manufacturers adopt diverse design elements, including muzzle brakes, suppressors, heavy stocks, and gas management systems, to alleviate perceived recoil and mitigate overpressure, thereby ensuring optimal performance and operator comfort. Additionally, proper training and adherence to effective discharging techniques empower operators to manage recoil efficiently and uphold accuracy during precision discharge (James & Dyer, 2011).

### 2.1.1. Recoil force resulting from an LPR discharge.

Recoil in LPR is characterized by the backward movement induced by the expulsion of high-pressure gases when the projectile is propelled out of the barrel (Figure 1). As the projectile travels in one direction, an equal and opposite force is exerted in the opposite direction, resulting in the backward recoil. This phenomenon is explained with Newton's third law of motion, articulating that every action prompts an equal and opposite reaction (Hazell, 2021). The magnitude of recoil forces can vary considerably, contingent upon factors such as the firearm type, caliber, and ammunition utilized (Burns, 2012). Notably, LPRs tend to exhibit more pronounced recoil forces due to the substantial energy released when discharging larger and heavier projectiles (Sherif Said et al., 2018).


Figure 1: Projectile propulsion through the barrel and the recoil force applied over the LPR. Adapted from (Hazell, 2021)

These recoil forces generated from the backward movement of the firearm are transmitted to the body of the operator through physical contact with the stock or grip (Y. Wang et al., 2020). Injuries resulting from this recoil force can occur due to improper shooting techniques or ineffective recoil management (Maksimovic, 2021), in particular shoulder injuries. Furthermore, these forces can momentarily cause the head to move backward, inducing head acceleration (Ouellet & St-Onge, 2021b). This backward movement is usually modest relative to acute injury thresholds, but previous studies have related head accelerations with mild concussions (Tierney, 2021).

While the majority of individuals can manage the recoil without significant issues, the repetitive head movement introduces a potential risk for concussions (R et al., 2014; Tierney, 2021). The extent of recoil experienced by the shooter is contingent upon various factors, including the caliber of the rifle, the weight of the firearm, and the design of the rifle itself (Morelli et al., 2014). Consequently, several devices and accessories are specifically designed to mitigate recoil in LPRs by absorbing or redirecting the energy generated during the recoil process (Chaturvedi & Dwivedi, 2018; Liu et al., 2020).

One example of a recoil-reducing device is the muzzle brake, which is affixed to the end of the barrel. This device is equipped with a series of ports or vents designed to redirect some of the escaping gases either upward or to the sides, effectively countering the backward force of recoil (Pešić et al., 2022) (Figure 2). It is important to note, however, that while muzzle brakes are effective in reducing recoil, they can concurrently amplify noise and overpressure in the surrounding area of the operator.

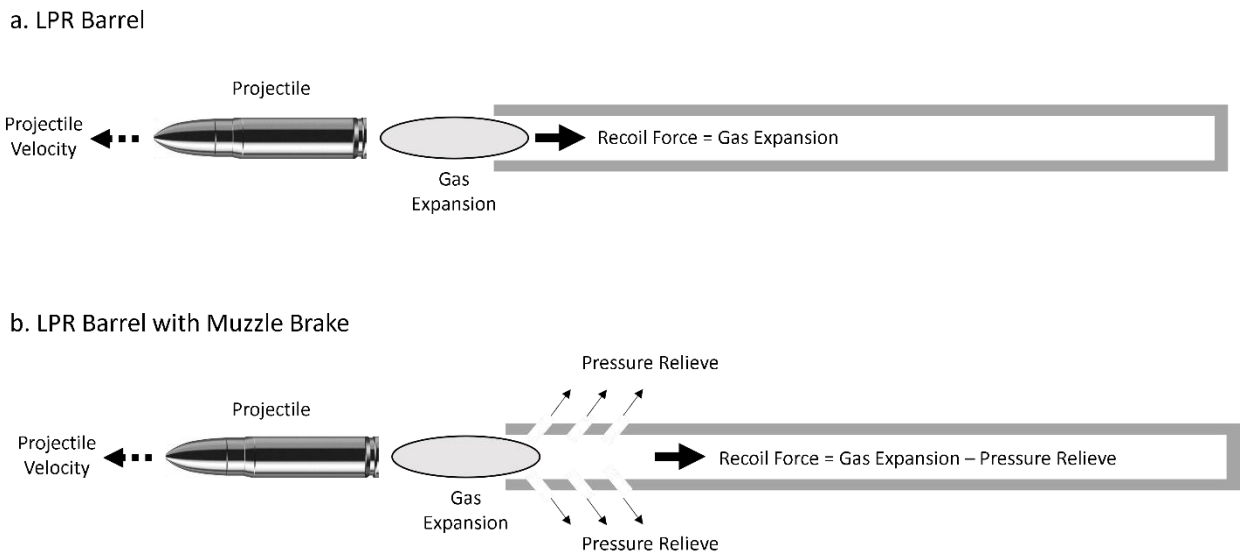


Figure 2: Comparison of forces produced by a barrel (a) without muzzle brake and (b) with muzzle brake. Adapted from (Pešić et al., 2022).

### 2.1.2. Overpressure resulting from an LPR discharge.

When the propulsion gas impulse the projectile from the muzzle, the rapid increase in air pressure is followed by a swift decrease, which generates a shock wave that propagates in all directions (Figure 3) reaching the head of the operator (Skotak et al., 2019). Due to the overpressure exposure may pose a risk of concussion (Nakashima et al., 2022), managing overpressure within safe limits is crucial to ensuring the safety of the LPR and its proper functioning (HEADQUARTERS, 1994). Nevertheless, the specific effects of overpressure have received relatively limited attention, with the majority of studies focusing on blast events, such as those involving breachers (Needham, 2018).

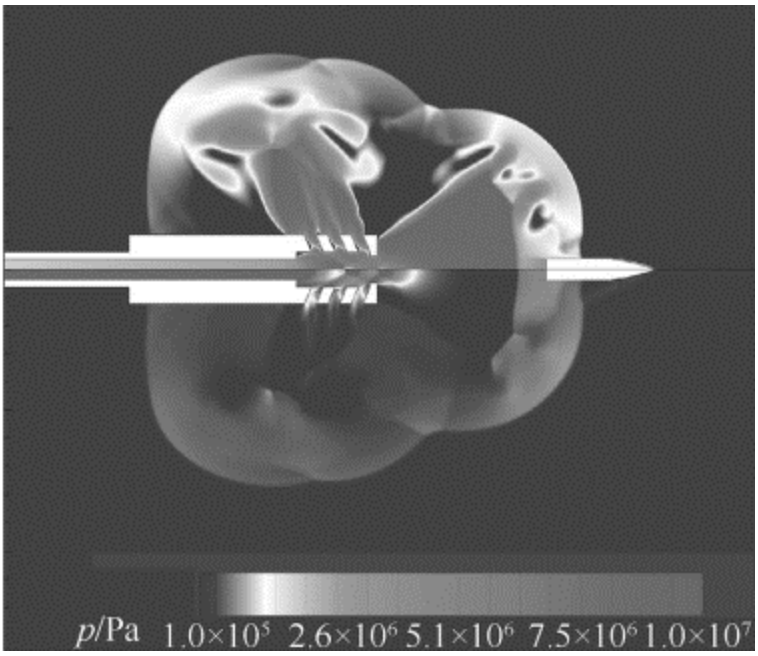


Figure 3: Simulation of overpressure produced by long rifle caliber 0.3 with a muzzle brake. Taken from (P. fei Li & Zhang, 2021) under © Attribution-NonCommercial-NoDerivs 4.0 International

To mitigate the overpressure, a suppressor can be employed to contain and decelerate the escaping gases through baffles (Figure 4), leading to a more gradual release of pressure instead of an abrupt blast (Figure 5) (Keith Hudson et al., 1996). The use of suppressors contributes to a more controlled and measured release of pressure, promoting safer operative behavior.

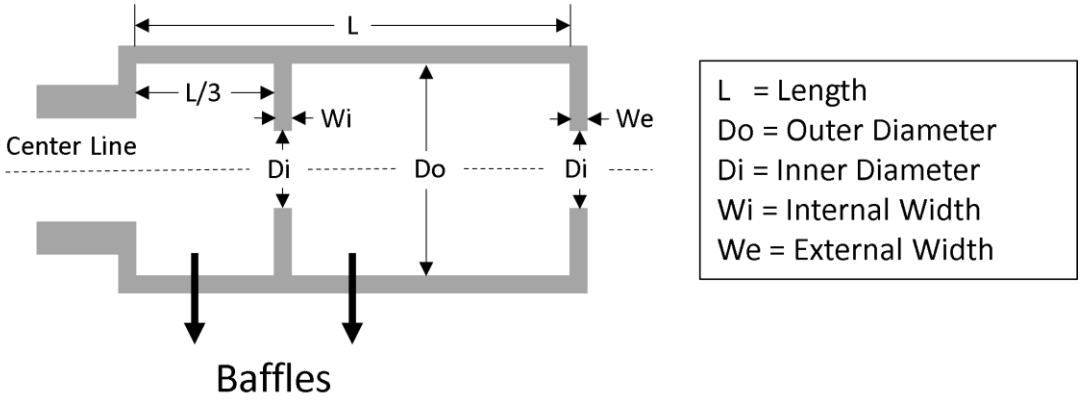


Figure 4: Cross section of suppressor sample showing the baffles used to contain and decelerate the escaping gases. Adapted from (Keith Hudson et al., 1996).

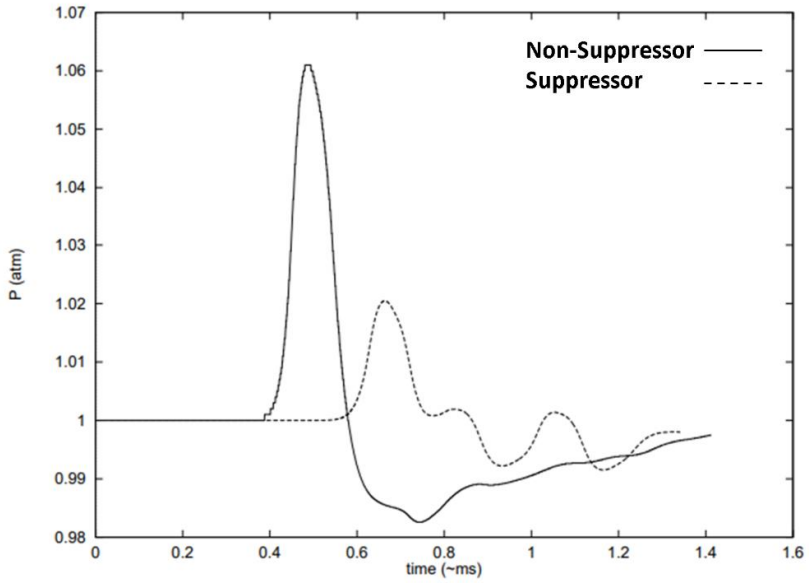


Figure 5: Overpressure measured at the muzzle of a 0.22 caliber rifle, with and without a suppressor. Taken from (Keith Hudson et al., 1996)

However, the redirection of gases within a suppressor has the potential to modify the equilibrium of forces exerted on the firearm, potentially leading to an amplified recoil (Sweeney, 2017). This impact tends to fluctuate based on various elements, including the design of the suppressor, rifle caliber, and the subjective perception of the operator (Kilikevičius et al., 2023). Despite the slight increase in recoil, the overall advantages of employing a suppressor, particularly in mitigating overpressure, typically outweigh this effect (Hazell, 2021).

## 2.2. Brain anatomy

To explain the brain anatomy, it is necessary to mention that the anatomy and position of the human body structures are described using a reference frame called the anatomy plane (Figure 6) (Cheng et al., 2012). There are three primary anatomical planes:

- Sagittal Plane: This plane divides the body or an organ vertically into left and right portions. When the sagittal plane passes directly through the midline of the body, it is referred to as the "midsagittal" or "median" plane.
- Coronal Plane (Frontal Plane): This plane divides the body or an organ into front (anterior) and back (posterior) portions.
- Transverse Plane (Horizontal Plane): This plane divides the body or an organ into upper (superior) and lower (inferior) portions. It runs horizontally, perpendicular to both the sagittal and frontal planes.

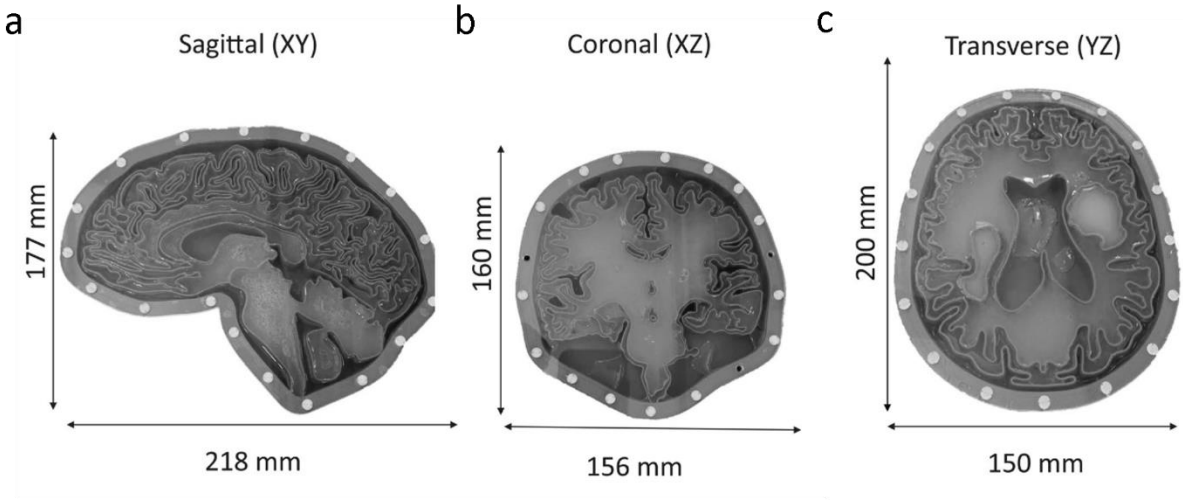


Figure 6: MRI head scan showing the sagittal (a), coronal (b), and transverse (c) planes. Taken from (de Vos et al., 2023)

### 2.2.1. Sections of the brain

The brain is formed by grey matter and white matter (Fargen, 2021) , which compound different tissues. While grey matter contains cell bodies and dendrites of neurons and is involved in processing information, white matter contains nerve fibers (neurons) that connect and communicate different parts of the brain. There are nine main sections within the brain, with their own distinct functions (Fargen, 2021):

1. Cerebrum: This is the largest part of the brain and is divided into two hemispheres (left and right). It is responsible for higher brain functions such as thinking, perceiving, producing, and understanding language, and controlling voluntary movements.
2. Cerebellum: Situated at the back of the brain beneath the cerebrum, the cerebellum is crucial for coordination, precision, and accurate timing of movements. It helps in maintaining balance and posture.
3. Brainstem: This connects the brain to the spinal cord and is essential for basic life functions such as breathing, heart rate, blood pressure, and swallowing.
4. Thalamus: Located in the center of the brain, the thalamus acts as a relay station for sensory information, directing it to the appropriate areas of the cerebral cortex for processing.
5. Hypothalamus: This region regulates many autonomic functions, including body temperature, hunger, thirst, sleep, and emotional responses. It also controls the release of hormones from the pituitary gland.
6. Pituitary Gland: This gland secretes hormones that control various bodily functions, including growth, reproduction, and metabolism.
7. Amygdala: Situated within the temporal lobes, this part of the brain is involved in the processing of emotions, particularly fear and pleasure responses.
8. Hippocampus: Vital for the formation of new memories and spatial navigation, the hippocampus is located in the temporal lobes.
9. Cerebral Cortex: This outer layer of the cerebrum is responsible for most higher brain functions, such as thinking, perceiving, planning, and language. It is divided into four lobes (Figure 7): frontal, parietal, temporal, and occipital, each associated with different

functions (e.g., frontal lobe with decision-making and motor function, temporal lobe with auditory processing).

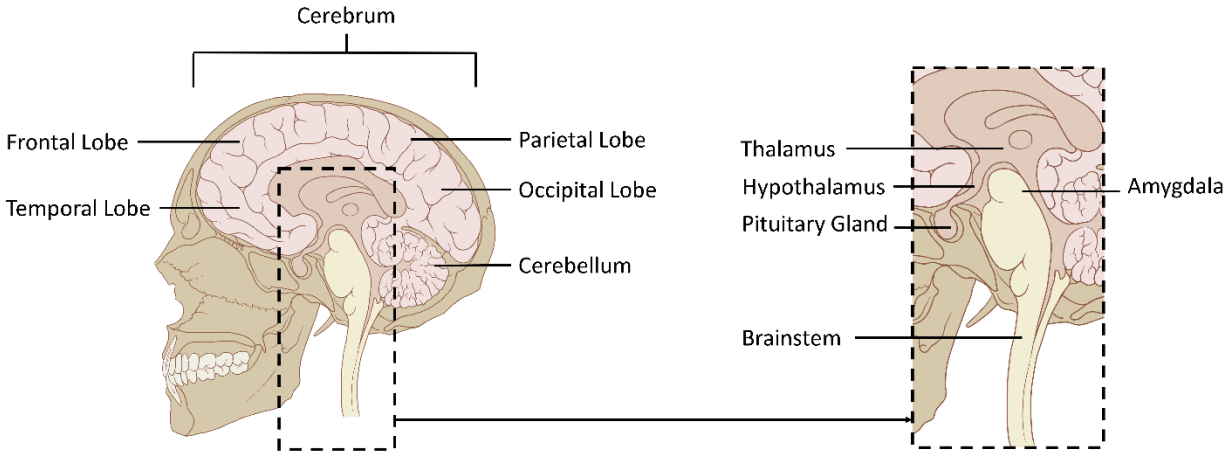


Figure 7: Sections of the brain. Adapted from (Lynch & Jaffe, 2006) © Attribution-NonCommercial-NoDerivs 2.5 International

### 2.2.2. Brain cells

The neurons are the fundamental units of the nervous system, including the brain, responsible for transmitting information as electrical and chemical signals (Popović & Sinkjær, 2013). Neurons consist of a cell body (soma), dendrites that receive signals from other neurons, an axon that transmits signals to other cells, and terminal branches that form synapses with other neurons (Demir et al., 2021).

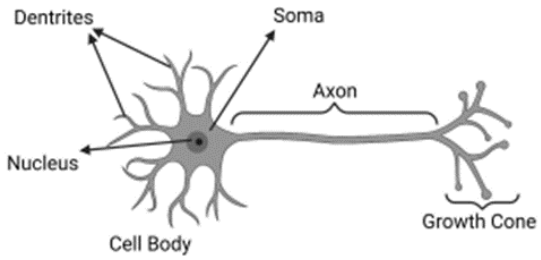


Figure 8: Neuron scheme showing the cell division. Taken from (Demir et al., 2021)

The neurons can be physically damaged under various circumstances, and this damage has significant implications for brain function (Maddy et al., 2023). This damage can be classified as:

- Axonal Injury (Bruggeman et al., 2021): This type of damage affects the axons, the long projections of neurons responsible for transmitting signals. Axonal injury can occur due to physical trauma, stretching, or shearing forces, leading to the disruption of axons.
- Dendritic Damage (Gao et al., 2011): Dendrites, the branch-like structures that receive signals from other neurons, can be damaged by physical trauma, toxins, or neurodegenerative conditions.
- Synaptic Dysfunction (Menorca et al., 2013): Neurons communicate with each other at synapses, where neurotransmitters transmit signals. Dysfunction at the synapse due to injury, toxins, or diseases can impair the release or reception of neurotransmitters, affecting signal transmission between neurons.

## 2.3. Relation of concussion symptoms with recoil forces and overpressures.

A concussion, categorized as a mild traumatic brain injury (mTBI), may occur as the result of head acceleration or exposure to overpressure, like accidents involving high-impact collisions or blast in military environments. The discharge of an LPR represents a scenario combining both overpressure and head accelerations (recoil forces), but typically at more modest levels than those associated with acute exposure leading to concussion symptoms.

### 2.3.1. Concussion symptoms

A concussion manifests when sudden and forceful loads are inflicted upon the head, resulting in brain tissue damage through deformation (Halabi, 2021). This damage in the brain tissues causes not only temporary alterations in the brain but also permanent damage to brain function (Mostofi et al., 2022). Commonly, this damage in brain function is assessed through the symptoms of a concussion, which can vary widely and may not always be immediately apparent.

Some common signs and symptoms include (Mathews et al., 2020):

- Headache or pressure in the head.
- Dizziness or balance problems.
- Nausea or vomiting.
- Sensitivity to light and noise.
- Confusion or feeling "foggy."
- Memory problems or difficulty concentrating.
- Fatigue or drowsiness.
- Changes in sleep patterns (e.g., sleeping more or less than usual).
- Irritability or changes in mood.
- Visual disturbances, such as blurred or double vision.

While most people recover from a concussion with rest and time, repeated concussions or severe concussions can lead to more significant and prolonged effects on neuronal function, potentially causing long-term cognitive issues or other neurological complications (Mostofi et al., 2022).

However, concussion prediction can be challenging due to several factors (Russo et al., 2023):

1. Heterogeneity of Concussions: Concussions can vary significantly in severity and symptoms, making it difficult to predict the outcome accurately. Different individuals may experience other symptoms, and the recovery time can vary widely from person to person.
2. Delayed Onset of Symptoms: In some cases, concussion symptoms may not immediately appear after the injury. Symptoms can manifest hours or even days after the initial event, making it challenging to predict the severity of the injury at the time of occurrence.
3. Lack of Objective Biomarkers: No widely accepted objective biomarkers or imaging techniques can definitively diagnose and predict the outcome of concussions. Diagnosis is often based on subjective symptoms the individual reports, making it harder to assess the injury.

4. Individual Factors: Various factors, such as age, gender, medical history, and genetics, can influence how an individual responds to a concussion. These complexities add to the difficulty of predicting the outcome for a specific person.
5. Cumulative Effects: Multiple concussions over time, significantly, if not fully healed from previous injuries, can lead to more severe and prolonged symptoms. The cumulative effects of concussions further complicate prediction efforts.
6. Lack of Long-Term Data: Concussions are relatively common, but there is still limited long-term data on the potential consequences of these injuries. Understanding long-term effects and the factors contributing to them is an ongoing area of research.

Due to these complexities, healthcare professionals use a comprehensive approach based on symptomatology to assess and address concussions (McGowan et al., 2021). Furthermore, ongoing research remains crucial for improving comprehension of concussions and establishing dependable biomarkers to advance prediction and prevention strategies.

### 2.3.2. Mechanisms of concussion

The common physical exposures associated with mTBI can be categorized into head impacts, head acceleration, or overpressure exposures (Figure 9) (Denny-Brown & Russell, 1941). The three mechanisms can be identified in military personnel, requiring research to improve the conditions.

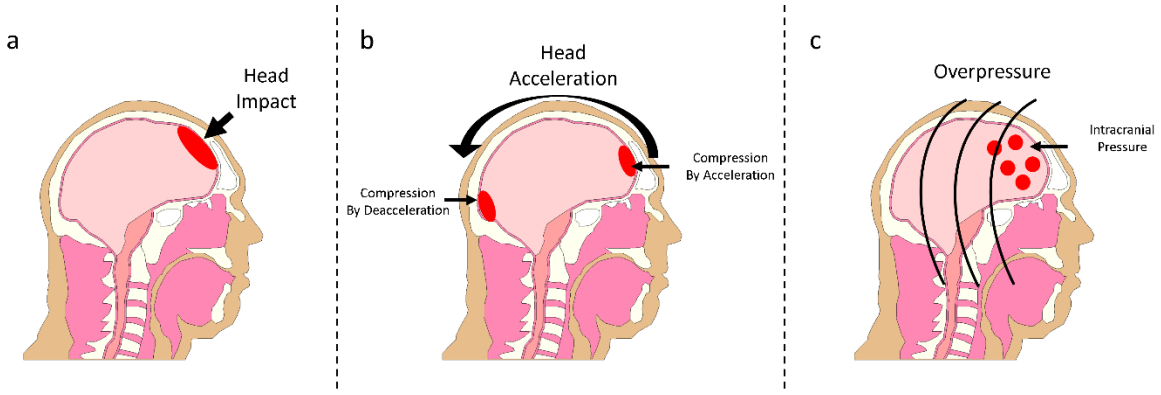


Figure 9: Concussion could be produced by head impact (a), head accelerations (b), and overpressure exposure (c)

Head impacts and accelerations initiate abrupt brain movements, causing strains develop due to the combination of inertia and forces (Stemper et al., 2015). Among military personnel, head impacts and accelerations represent common causes of concussions (Kong et al., 2022).

Conversely, individuals exposed to overpressure endure adverse effects on brain cells, potentially culminating in concussion (N. W. Nelson et al., 2015). This overpressure, characterized by the transmission of both positive and negative intracranial pressures, significantly impacts the proper function of brain tissues (Bustamante et al., 2018; Panzer et al., 2012; Zhang et al., 2004). Military personnel encounter diverse ranges of overpressure, facing exposure from explosives generating high-energy overpressure, to rifle discharges producing low-energy overpressure (M. R. Miller et al., 2022; T. J. Nelson et al., 2006; Woodall et al., 2023).

## 2.4. Finite element models to assess brain response

In the investigation of brain responses to traumatic events such as head impacts and overpressure, FE models emerge as a relevant tool. The utility of these FE models extends across multidisciplinary domains (F. Wang et al., 2022), providing a significant advantage for researchers, engineers, and medical practitioners.

The advantages of FE models include (Maas et al., 2012):

- Virtual Experiments: FE models allow researchers to conduct virtual experiments that would be ethically and practically challenging to perform in real life. They provide a controlled environment to investigate various impact and overpressure scenarios.
- Design Optimization: FEMs assist in optimizing the design of protective equipment, such as helmets and headgear, by evaluating their effectiveness in mitigating brain injuries. Designers can iterate and refine their products based on FEM predictions to enhance safety.
- Injury Thresholds: By simulating different loading conditions, FEMs help identify injury thresholds for various brain regions and types of injuries. These thresholds help establish safety standards and guidelines for preventing brain injuries in real-world situations.

Integrating the FE models within the context of brain response studies and their methodologies could strengthen the discussion of tools and approaches used in understanding traumatic events on the brain (Singh & Cronin, 2019).

However, FE models have limitations, such as simplifications in representing complex brain dynamics, uncertainties in material properties, and the need for experimental validation (Henninger et al., 2010). Real-world data is crucial to validate and refine FE models, ensuring their accuracy and enhancing our understanding of brain injuries for improved prevention and intervention strategies.

### 2.4.1. Geometry and meshing of FE models

FE models rely on the process of discretization, where a complex geometric domain is subdivided into interconnected elements, commonly triangles or quadrilaterals in 2D simulations and tetrahedra or hexahedra in 3D simulations (Bern & Plassmann, 2000). In the realm of biomechanical applications, this discretization process necessitates acquiring anatomical geometry and establishing a mesh that obtains a balance between mesh size and computational efficiency.

Acquiring head anatomy necessitates the utilization of medical imaging data, such as MRI or CT scans, to generate a digital 3D representation of internal and external structures. This process involves image segmentation, 3D reconstruction, mesh generation, and assignment of material properties (K. M. Tse et al., 2014).

Additionally, achieving an appropriate mesh size (Figure 10) is necessary for accurately capturing head behavior, as it directly influences both convergence and result accuracy (Singh et al., 2014). Smaller elements are advantageous in representing intricate geometries, yet they necessitate a higher element count, demanding greater computational resources (Ern & Guermond, 2021). Hence, achieving the ideal mesh refinement becomes crucial in developing an efficient FE model, wherein 'correct refinement' denotes striking a balance between precision in mesh representation and manageable computational demands (Zohdi, 2015).

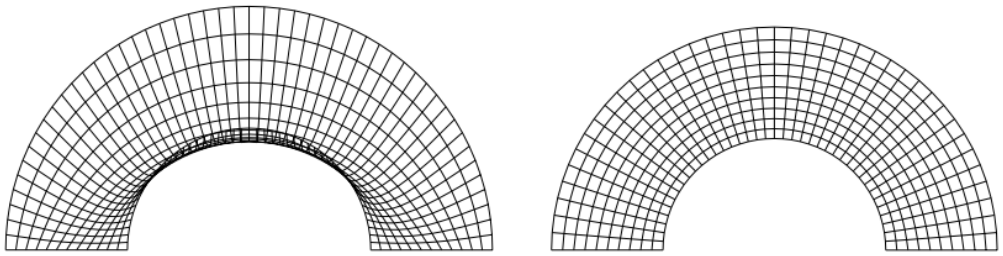

Figure 10: Example of meshing with inappropriate (a) and appropriate (b) quality of elements. Taken from (Bern & Plassmann, 2000)

### 2.4.2. Constitutive material models used in FE head models

In this study, constitutive models play a critical role in determining the mechanical reaction of the model to various loads, and this reaction is characterized by stress, strain, shear, and a combination of these factors (François et al., 2012). Previous head models include a combination of the following material models:

- Elastic materials: The head parts can be defined using elastic materials that adhere to Hook's law, exhibiting a linear relationship between stress and strain within their elastic limit (Chafi et al., 2012; Roberts et al., 2012). Elastic materials are defined by Young's modulus, and Poisson's ratio, describing reversible deformation behavior under mechanical loads. It is important to notice that elastic materials are suitable for simulating structures and components in engineering with small deformations.

- Hyperelastic materials: Hyperelastic materials are used in biomechanics for modeling the nonlinear and mechanical behavior of soft tissues, including muscles and blood vessels (Khaniki et al., 2023). Using a strain energy density function, this material model describes the non-linear relationship between stress and strain in biological tissues (Figure 11).

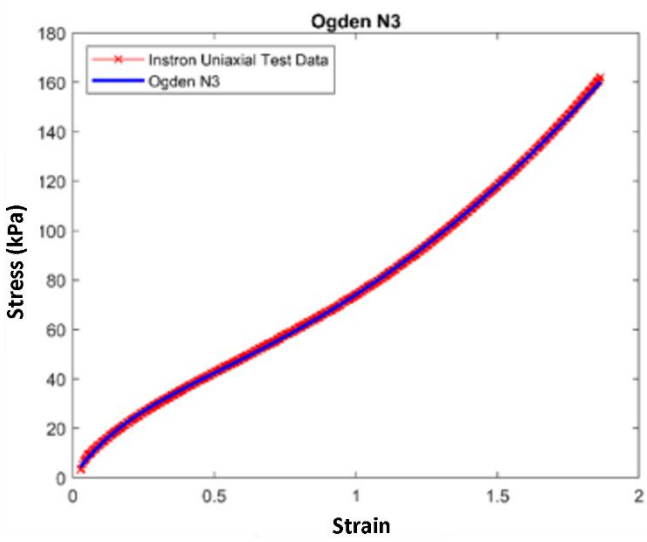


Figure 11: Example of stress vs strain of ligaments fitted by hyperelastic material model (Ogden). Taken from (Mollaee et al., 2023) under © Attribution-NonCommercial-NoDerivs 4.0 International

- Viscoelastic materials: The brain tissues are modeled as viscoelastic materials, which exhibit both viscous and elastic behaviors in response to applied forces (Labus & Puttlitz, 2016). When subjected to stress, these materials undergo both immediate elastic deformation and time-dependent viscous flow, with their responses varying based on the rate and duration of the applied load (Figure 12).

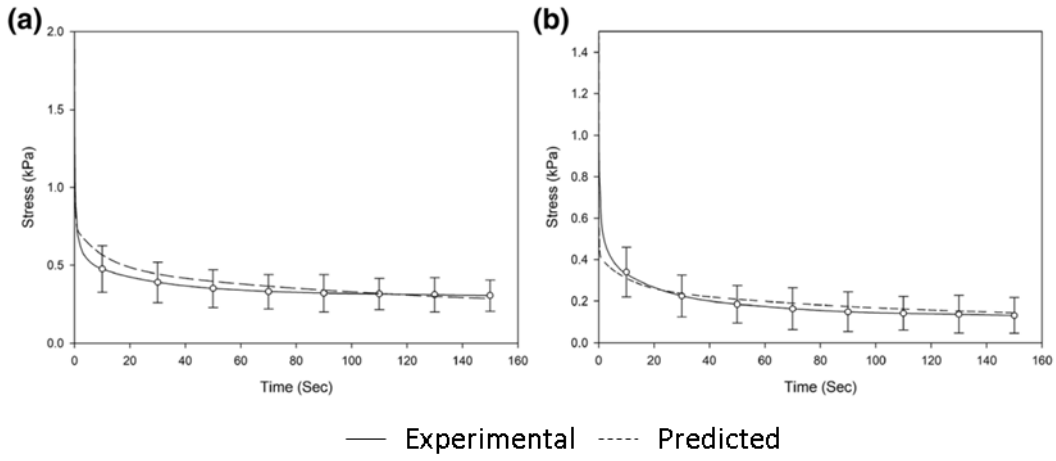


Figure 12: White (a) and grey (b) tissue represented with a viscoelastic model. Taken from (W. Li et al., 2021) under © Attribution-NonCommercial-NoDerivs 4.0 International

It is important to note that the Cerebrospinal Fluid (CSF) was a particular case of tissue in the FE model. This tissue layer between the brain and skull plays a role in distributing forces and dampening impacts (Panzer et al., 2012), which was represented using fluid material properties represented by a bulk modulus and viscosity.

### 2.4.3. Finite element head models to assess impact and acceleration loading

The application of FE models to simulate head injuries emerged in the 1970s, aiming to solve challenges beyond the capabilities of experimental methods (K. Tse et al., 2015). Although the initial 2D models exhibited unrealistic deformations, they provided significant insights into head behavior within defined parameters. Subsequent advancements progressively enhanced these models by refining geometries, materials, and contact properties, trying to achieve outcomes that closely correlate with empirical data.

The initial foray into head modeling via FE analysis introduced a planar skull model (Hardy & Marcal, 1973) with elastic material properties, aiming to predict deformations resulting from frontal and lateral impacts. Successive enhancements integrated the brain into the model (Shugar, 1975), represented by elastic fluid materials. Despite producing unrealistic outcomes, this step laid the groundwork for subsequent advancements in modeling approaches.

At first, three-dimensional models resembled spherical shells to simulate head behavior (Kenner & Goldsmith, 1972; Khalil & Hubbard, 1977). Conversely, they progressively evolved into more complex geometries to better mirror the head's morphology (Yang et al., 2009). The 1990s witnessed a significant leap forward with the advent of robust computational systems, empowering researchers to craft increasingly intricate three-dimensional models—an ongoing trajectory explored in recent studies (Bruneau & Cronin, 2020; Deck & Willinger, 2008; Willinger & Baumgartner, 2003).

Contemporary three-dimensional head models (Figure 13) lean on human anatomical data acquired from scans and MRIs (Madhukar & Ostoja-Starzewski, 2019). However, these cutting-edge models face notable challenges, particularly in defining contacts and representing materials, as they strive for enhanced precision in emulating realistic behaviors.

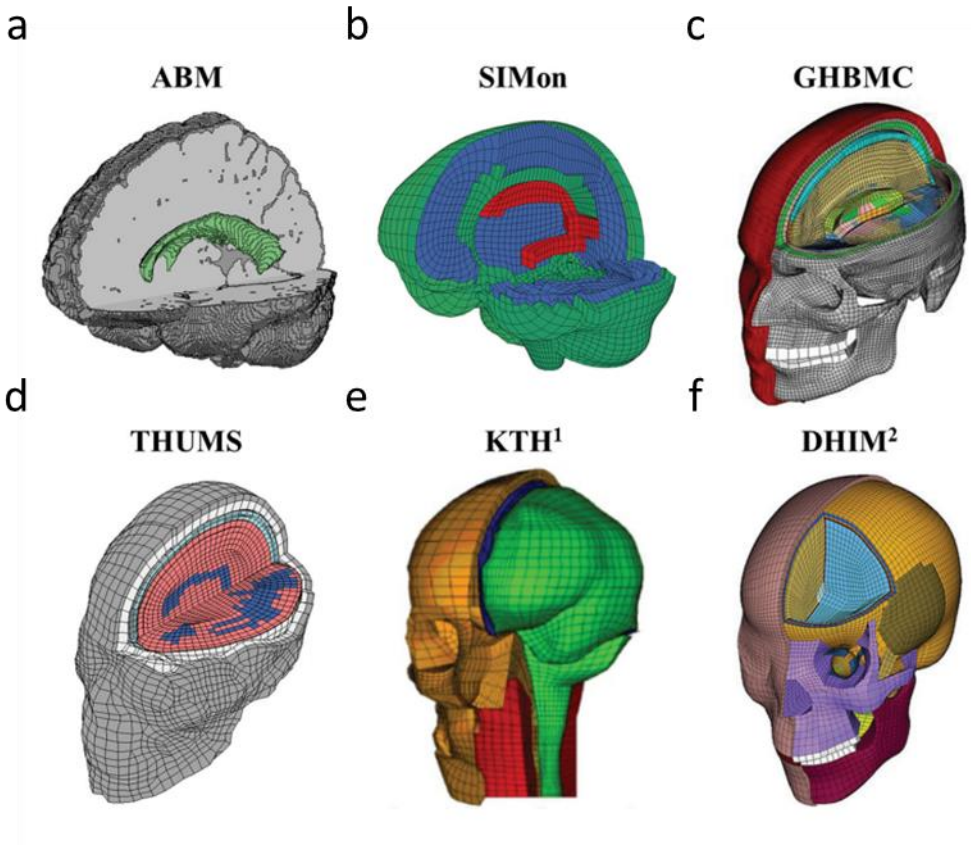


Figure 13: Modern three-dimensional head models, including ABM (a), SIMon (b), GHBMC (c), THUMS (d), KTH (e), and DHIM (a)

While three-dimensional models excel in replicating impact and head acceleration loads, it is important to note that their capabilities are limited in simulating overpressure loads. This limitation lays in the computational requirement, which reduce the maximum possible number of elements in the models. This reduction affects the accuracy in the overpressure estimation and the calculus of material behavior (Virzi Mariotti et al., 2019).

### 2.4.4. Finite element head models to assess overpressure

The overpressure head model involves a fluid-solid interaction, wherein the overpressure signifies a transferred of pressure load from the air (fluid) onto the head (solid). The primary method employed to address this complexity is the Arbitrary Lagrangian-Eulerian (ALE) method (Lotfy & Ezzeldin, 2023; Peng et al., 2023), specifically designed as a meshing technique to simulate contact between a highly deformable mesh (fluid) and a less deformable mesh (solid). Subsequent research has bifurcated into two paths: three-dimensional models and planar models, each offering distinct advantages and disadvantages.

The ALE method functions as a computational technique engineered to replicate the behavior of fluids and solids undergoing significant deformations or motions (Donea et al., 2004). It amalgamates the Lagrangian approach, which traces material motion (fluid), with the Eulerian approach utilizing a stationary grid (for fluid contour and fluid-solid contacts) (Figure 14). ALE necessitates continual mesh updates while concurrently solving equations, enabling accurate domain tracking within the grid. This versatile method finds application in both three-dimensional and planar models.

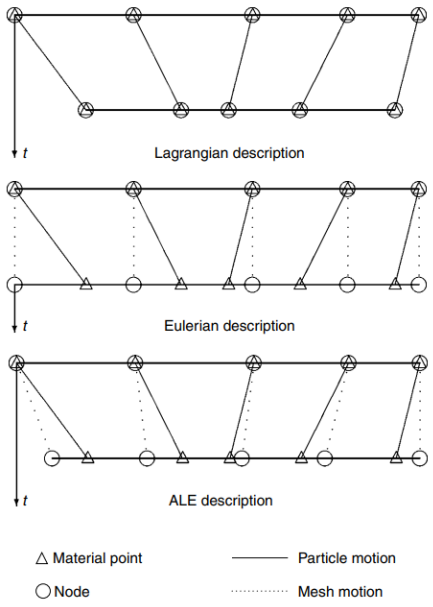


Figure 14: Variation in the mesh motion using (a) the Lagrangian description, (b) the Eulerian description, and (c) the ALE description. Taken from (Donea et al., 2004)

Initially, three-dimensional models employed simplified head geometries, often using shapes like spheres (Panzer et al., 2012, 2013). As time progressed, these models evolved toward more intricate geometries (Du et al., 2022; Huang et al., 2022; Sutar & Ganpule, 2022), successfully predicting head behavior. However, these advancements came with a significant computational demand, imposing restrictions on both the level of geometric detail (number of elements) and simulation duration.

In contrast, planar models strive to streamline the overpressure-head issue, efficiently utilizing computational resources (Panzer et al., 2012; Singh et al., 2014; Singh & Cronin, 2019, 2017). Typically, these models employ a dual approach by utilizing two planar models (sagittal and transverse) to replicate the overpressure effect, offering a viable alternative to three-dimensional models. This approach facilitates longer simulation durations with increased element count, thereby enhancing the capabilities of the model.

## 2.5. Metrics to assess brain injury

Estimating the brain response to specific boundary conditions stands as a crucial predictive measure for potential brain injuries. This assessment involves the utilization of diverse metrics and corresponding thresholds proposed by different authors to measure and predict brain injuries. Within this context, this study establishes a categorization of these injury metrics into two distinct groups: global metrics and tissue-level metrics.

### 2.5.1. Global metrics for brain injury based on head kinematics

Global brain injury metrics include Head Injury Criterion (HIC) and Brain Injury Criteria (BrIC), among others.

- The HIC (Schmitt et al., 2019a) (Equation 1) is a quantitative measure used to assess the potential for head injury resulting from an impact or collision. It is a widely used parameter in biomechanics and automotive safety to evaluate the likelihood of head trauma during

accidents. The HIC is designed to indicate the severity of a head impact based on the acceleration-time history of the center of gravity of the head.

The HIC is calculated using the following formula:

$$HIC = max\left\{\left[\frac{1}{(t_2 - t_1)}\int_{t_1}^{t_2} a(t)dt\right]^{2.5}(t_2 - t_1)\right\} \quad (1)$$

Here, $a(t)$ presents the head's acceleration as a function of time during the impact, $t_1$ and $t_2$ are the beginning and ending times of the time interval over which the integral is computed. The HIC is often reported as a single scalar value and is used as a criterion to compare different impact scenarios and evaluate the potential risk of head injury.

- The BrIC (Takhounts, Craig, Moorhouse, Mcfadden, et al., 2013) (Equation 2) is a brain injury assessment metric that focuses on rotational velocities as a critical factor in predicting the likelihood of brain injury. Unlike linear acceleration, angular momentum measures the rate of change of angular displacement around a rotational axis. In the case of head impacts, rotational velocities can lead to shearing and stretching of brain tissue, which are associated with different brain injuries. It considers the rate between angular velocities and the critical angular velocity to provide a threshold value beyond which the risk of brain injury increases significantly.

$$BrIC = \sqrt{\left(\frac{W_x}{W_{xC}}\right)^2 + \left(\frac{W_y}{W_{yC}}\right)^2 + \left(\frac{W_z}{W_{zC}}\right)^2} \quad (2)$$

Where: $W_x$, $W_y$, and $W_z$ are the rotational velocities in axes X, Y, and Z, respectively. $W_{xC}$, $W_{yC}$, and $W_{zC}$ are the critical rotational velocities in axes X, Y, and Z, respectively.

By correlating the results of finite element simulations with injury metrics, researchers can gain valuable insights into the potential risks of overpressure and recoil-induced head injuries. This

information can be used to improve safety measures to minimize the risk of head injuries in different scenarios.

### 2.5.2. Tissue level metrics for brain injury

Brain tissue level metrics for injury involve quantitative measures analyzing how elements respond to boundary conditions. These metrics offer valuable insights into tissue deformation, intracranial pressure, and potential damage, thereby facilitating a deeper comprehension of injury mechanisms.

The maximum principal strain (MPS) (Mcallister et al., 2012) serves as an engineering metric to quantify the deformation experienced by elements, such as brain meshing when subjected to external forces. By evaluating MPS across different brain regions, researchers can infer potential damage to neural structures, thereby informing the development of strategies for injury prevention and mitigation (Wu et al., 2021). Notably, in the context of this study, the external forces pertain to the kinematic and overpressure load generated by the LPR discharge.

An additional option to evaluate the tissue deformation in the FE model is the Cumulative Strain Damage Measure (CSDM). The CSDM (Knowles & Dennison, 2017) (Equation 3) is a metric used to assess the risk of diffuse axonal injury in the brain due to traumatic events, such as impacts or accelerations. Diffuse axonal injury involves the stretching (strain) and tearing of nerve fibers (neurons) throughout the brain, which can lead to serious neurological consequences. CSDM is calculated by integrating the magnitude of strains experienced by brain tissue over a specified period.

$$CSDM = \int_0^T \sqrt{\frac{\varepsilon^2}{T}}\, dt \qquad (3)$$

Where ε represents the principal strain magnitude, and T is the time interval the strain occurs.

On the other hand, Intracranial Pressure (ICP) has been suggested in prior studies as a tissue-level metric for evaluating mTBI (Du et al., 2022; Ward et al., 1980). This metric offers dual values: positive ICP associated with tissue compression (Zhang et al., 2004) and negative ICP associated with cavitation within the brain fluid (Bustamante et al., 2018; Panzer et al., 2012; Zhang et al., 2004).

Both MPS and ICP can be evaluated through two approaches: tracking their response over time using the $95^{th}$ percentile of element histories and analyzing their cumulative volume fraction response. The $95^{th}$ percentile method helps observe the variation of MPS and ICP over time while minimizing the influence of individual elements with artificially high values (Cecchi et al., 2023). On the contrary, the cumulative volume fraction analysis showcases the distribution of MPS and ICP within the brain geometry, pinpointing specific brain areas responsive to external loads (such as overpressure and kinematics) (Seeburrun et al., 2023).

### 2.5.3. Brain injury thresholds

Brain injury thresholds represent specific values of injury metrics associated with mBTI determined by previous researchers under specific conditions. These thresholds may be derived from either global or tissue-level metrics, depending on the precise load conditions being evaluated.

It is crucial to highlight that global metrics are derived through empirical formulations specific to certain types of kinematic loads (Gabler et al., 2019). As a result, these metrics are constrained to the particular load conditions under which they were formulated.

Yet, the significance of these injury thresholds based on global metrics lies in their ability to standardize brain injury risk assessment under specific conditions, such as car collisions (Carroll et al., 2010). Additionally, within the automotive sector, the development of the Abbreviated Injury Scale (AIS) has enabled the definition of distinct injury levels resulting from automobile accidents (Schmitt et al., 2019b) (Table 1).

Table 1: Abbreviated Injury Scale (AIS)

| AIS code | Injury |
|---|---|
| **1** | Minor |
| **2** | Moderate |
| **3** | Serious |
| **4** | Severe |
| **5** | Critical |

The following table (Table 2) summarizes the brain injury thresholds with corresponding metrics and load conditions.

Table 2: Brain injury thresholds with corresponding metrics and load conditions

| Injury Metric | Injury Risk | Injury Threshold | Load Condition | Author |
|---|---|---|---|---|
| **CSDM** | 25% probability AIS 4+<br>50% probability AIS 4+<br>80% probability AIS 4+ | 0.39<br>0.54<br>0.73 | Side and frontal impact | (Takhounts, Craig, Moorhouse, Mcfadden, et al., 2013) |
| **BrIC** | 25% probability AIS 4+<br>50% probability AIS 4+<br>80% probability AIS 4+ | 0.72<br>1.00<br>1.35 | Frontal impact | (Takhounts, Craig, Moorhouse, Mcfadden, et al., 2013) |
| **HIC-15** | 25% probability AIS 4+<br>50% probability AIS 4+<br>80% probability AIS 4+ | 800<br>1000<br>1300 | Side and frontal impact | (Virzi Mariotti et al., 2019) |

Regarding tissue-level metrics, researchers have dedicated efforts toward establishing thresholds for these metrics since the inception of the initial head models (K. Tse et al., 2015). The MPS commonly serves as a validation tool for material behavior within head models (Galbraith et al., 1993), while the ICP validates the overall behavior of the brain within these models (Ward et al., 1980).

The following table presents a summary of the injury thresholds for tissue-level metrics (K. Tse et al., 2015).

Table 3: Injury thresholds for tissue-level metrics

| Injury Metric | Injury Risk | Injury Threshold | Load Condition | Author |
|---|---|---|---|---|
| **MPS** | Structural Failure<br>Functional Deficit<br>Reversible Injury | 0.25<br>0.20<br>0.10 | A uniaxial load was applied to axons | (Galbraith et al., 1993) |
| | 25% probability of mBTI<br>50% probability of mBTI<br>80% probability of mBTI | 0.13<br>0.18<br>0.28 | Vacuum pressure was applied to brain tissues | (Shreiber et al., 1997) |
| | 25% probability of mBTI<br>50% probability of mBTI<br>80% probability of mBTI | 0.14<br>0.19<br>0.24 | Head-to-head impact | (Zhang et al., 2004) |
| **Positive ICP** | Injury<br>Minor Injury | >235 kPa<br>173 – 235 kPa | Frontal Impact | (Ward et al., 1980) |
| | Injury<br>Minor Injury | 66 – 114 kPa<br>44 – 66 kPa | Head-to-head impact | (Zhang et al., 2004) |
| **Negative ICP** | Injury<br>Minor Injury | -101 - -51 kPa<br>-59 - -23 kPa | Head-to-head impact | (Zhang et al., 2004) |

A recent study (Lyu et al., 2022) has proposed correlations between the MPS (Equation 4) and ICP (Equation 5) regarding concussion risk, derived through statistical analysis (Weibull curve). While these relationships were established for a defined scenario involving frontal impact and blast, the concussion risks they define could serve as a valuable reference point to comprehend the impact of combined head accelerations and overpressure loads.

$$P.Concussion = \frac{1}{1 + e^{-9.184 * MPS_{peak} + 4.195}} \quad (4)$$

$$P.Concussion = \frac{1}{1 + e^{-0.02394 * ICP_{peak} + 3.8606}} \quad (5)$$

# 3. Experimental Methods to Measure Head Loading Conditions

This section presents in the experiments and processing methodology used to measure the overpressure and kinematic effects produced around the head of the operators by an LPR caliber 0.5. These overpressure and kinematics effects were studied using two experiments developed by Defense Research and Development Canada (DRDC) Valcartier Research Centre. The data obtained from these experiments were processed in this study to examine the variations in kinematics and overpressure effects on the operators depending on the LPR configuration and the operators.

The kinematics and overpressure data were classified depending on the type of data collected (kinematic or overpressure), the operator, and the LPR configuration (Table 1), obtaining two kinematic datasets and two overpressure datasets. Specifically, these kinematics datasets were divided into a first set of cases with one operator discharging different configurations of LPRs and a second set of cases with different operators discharging one LPR configuration. On the other hand, the overpressure datasets were divided between four discharges of the LPR with non-suppressor configuration and four discharges of the LPR with suppressor configuration.

Table 4: Matrix of experimental data obtained from LPR discharge under different testing conditions.

| ID | Measurement | Operator ID | Operators | Configuration | Discharge ID | High-Speed Video |
|---|---|---|---|---|---|---|
| **KNO1D1** | Kinematics | O1 | Human | Non-suppressor | D1 | No |
| **KNO1D2** | Kinematics | O1 | Human | Non-suppressor | D2 | No |
| **KSO1D1** | Kinematics | O1 | Human | Suppressor | D1 | No |
| **KSO1D2** | Kinematics | O1 | Human | Suppressor | D2 | No |
| **KSO2D1** | Kinematics | O2 | Human | Suppressor | D1 | Yes |
| **KSO3D1** | Kinematics | O3 | Human | Suppressor | D1 | Yes |
| **KSO4D1** | Kinematics | O4 | Human | Suppressor | D1 | Yes |
| **KSO5D1** | Kinematics | O5 | Human | Suppressor | D1 | Yes |
| **ONH1D1** | Overpressure | H1 | Hybrid III | Non-suppressor | D1 | Yes |
| **ONH1D2** | Overpressure | H1 | Hybrid III | Non-suppressor | D2 | No |
| **ONH1D3** | Overpressure | H1 | Hybrid III | Non-suppressor | D3 | No |
| **ONH1D4** | Overpressure | H1 | Hybrid III | Non-suppressor | D4 | No |
| **OSH1D1** | Overpressure | H1 | Hybrid III | Suppressor | D1 | Yes |
| **OSH1D2** | Overpressure | H1 | Hybrid III | Suppressor | D2 | No |
| **OSH1D3** | Overpressure | H1 | Hybrid III | Suppressor | D3 | No |
| **OSH1D4** | Overpressure | H1 | Hybrid III | Suppressor | D4 | No |

## 3.1. Measurement of kinematic reaction to LPR recoil

The LPR discharge produced recoil forces on the operator as a reaction to the projectile propulsion, producing a kinematic effect (linear acceleration and rotational velocities) on the head along three coordinate axes. This kinematic effect was measured using instrumented mouthguards (Prevent IMM, Prevent Biometrics, Minneapolis, USA) during discharging sessions, which were defined to study the operator dependency and the effect of the LPR configuration (suppressor and non-suppressor). However, these instrumented mouthguards used a coordinate system defined by the mouthguard (mouthguard coordinate system), and the kinematic data needed to be defined in the center of gravity of the head. To approach the kinematic effect on the head, the measured linear acceleration and rotational velocities were transformed into the head coordinate system.

First, the linear acceleration and rotational velocity along the time of five operators were measured by DRDC using an instrumented mouthguard during LPR discharges. The kinematic data corresponded to two datasets and aimed to study the kinematic effect variation depending on the LPR configuration or the operator. The first dataset consisted of four operators discharging an LPR with a suppressor configuration, carrying out one discharge per operator to study the subject dependency. The second set showed the variation between LPR configurations, collecting data from the fifth operator performing two discharges per each LPR configuration (suppressor and non-suppressor).

The second step was data processing, in which the collected kinematics data was transformed to reduce the signal noise and represent the center of gravity movement of the head of the operators (Seeburrun et al., 2023). Initially, the data were processed by applying 4th-order low-pass filters with 500 Hz and 50 Hz corner frequencies. Then, the curves were converted from the mouthguard coordinate system to the head center of gravity (Figure 15), applying vector transformation (Equation 6).

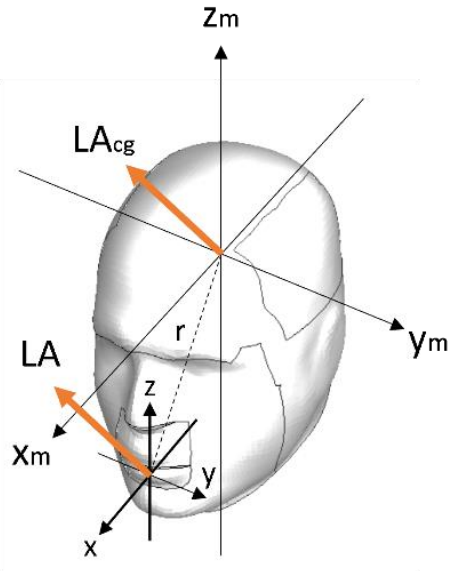


Figure 15: Diagram for the head coordinates system and radius were used to convert the acceleration vector received from the mouthguard coordinate system into the center of gravity.

$$LA_{cg} = LA + RA * r + RV * (RV * r) \quad (6)$$

The vector transformation used the rotational velocity (RV) and the rotational acceleration (RA) to transform the linear acceleration from the mouthguard coordinate system (LA) to an equivalent linear acceleration in the head coordinate system ($LA_{cg}$). The rotational acceleration was calculated by differentiating the rotational velocity, and the head radius (r) was estimated using the $50^{th}$ percentile male head value.

## 3.2. Measurement of the overpressure produced by LPR discharge.

Four overpressure sensors (XCL-100, Kulite Semiconductor Products, New Jersey, USA) were located on the forehead, the right side, the left side, and the rear side of a Brain Injury Protection Evaluation Device (BIPED) incorporated into a Hybrid III ATD ((ATD Hybrid III 50th Male, Humanetics, Michigan, USA) (Figure 16) (Ouellet & Philippens, 2018). This Hybrid III recreated the prone position of the operator with the LPR positioned over the right shoulder, remotely discharging the LPR four times with the non-suppressor configuration and another four times with the suppressor configuration.

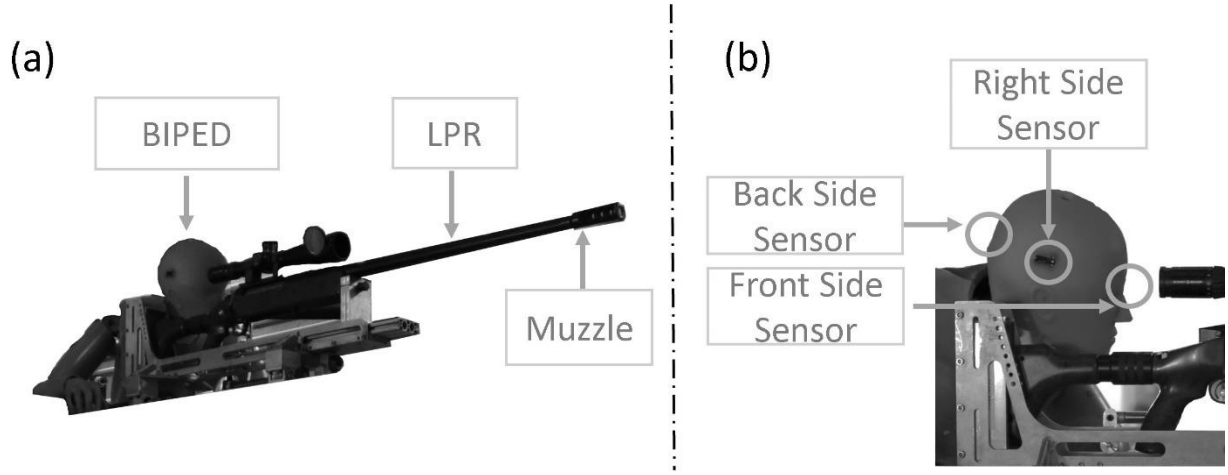


Figure 16: BIPED incorporated in a Hybrid III was used to measure the overpressure propagation from the muzzle of an LPR. Isometric view of the mannequin and trigger device on the platform (a), and a close view of the mannequin's head showing the location of the sensors (b).

## 3.3. Sequence of kinematic and overpressure reactions

The LPR discharge produced an overpressure effect on the operator, followed by the kinematics with a variable delay time between both effects (Figure 17). Furthermore, this delay time variation was one of the objectives of this study because the interaction between overpressure and kinematic effects over the head has yet to be assessed. Due to the overpressure and kinematics datasets being aligned in time with the corresponding trigger of the sensors, the offset of these datasets did not coincide. Thus, the moment of projectile propulsion from the muzzle was used as a reference to measure the respective times before the overpressure and kinematic sensors were triggered, synchronizing both datasets in a single offset.

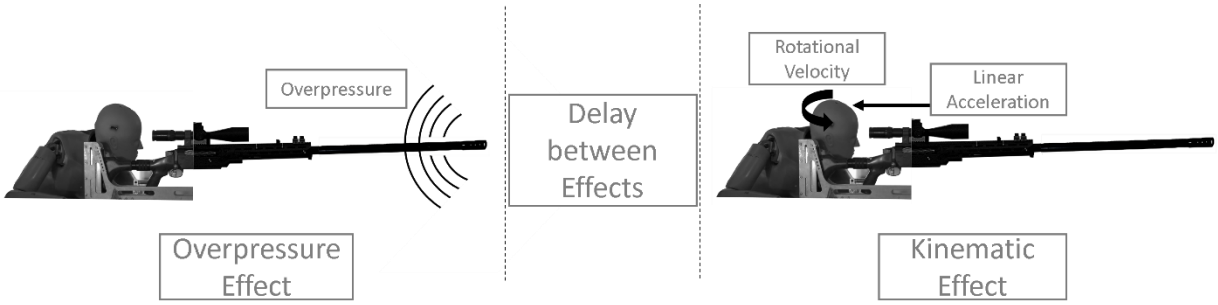


Figure 17: The sequence of events consisted of the overpressure effect followed by the kinematic effect with a delay between them.

Initially, the time for the kinematic sensor triggered after the projectile propulsion was estimated using free-source video tracking software (Tracker, Open-Source Physics Project)(Brown & Cox, 2009), and 3000 frames-per-second high-speed videos (FASTCAM SA-Z, Photron, San Diego, USA) of four operators discharging an LPR with the suppressor configuration (Figure 18). The kinematic sensor triggering coincided with the time for the first head movement of the operators, which was estimated by plotting the displacement tape mark on the right side of the head. In addition to this time for the first head movement, the moment the bullet was propelled from the muzzle was measured in the high-speed video. The difference between both times defined these omitted times before the kinematic sensor was triggered, which was added to the kinematic curves to adjust them into the LPR time frame.


Figure 18: The operator in a prone position discharged an LPR with a suppressor configuration, and the head movement was tracked using tape marks and free-source video tracking software.

Then, the time since the projectile propulsion to the pressure sensor triggering was calculated and added to the time axis in the pressure sensor measurements, assuming a constant velocity for the overpressure wave propagation (Equation 7). The time since the projectile propulsion to the pressure sensor triggering ($\Delta t$) was equal to the distance between the muzzle and the frontal sensor ($\Delta d$) divided by the overpressure wave speed ($v$). To obtain the variable, the discharge of an LPR with the suppressor and non-suppressor configuration was recorded using a 25000 frames per second high-speed video (FASTCAM SA-Z, Photron, San Diego) with the Schlieren image method (Figure 19), which showed the overpressure wave movement caused by the overpressure through the contrast of fluid density differences. Then, the displacements of the overpressure waves were measured in centimeters per frame using Tracker and multiplied by the 25000 frames per second to obtain the overpressure wave speeds.

$$t = \frac{d}{v} \tag{7}$$

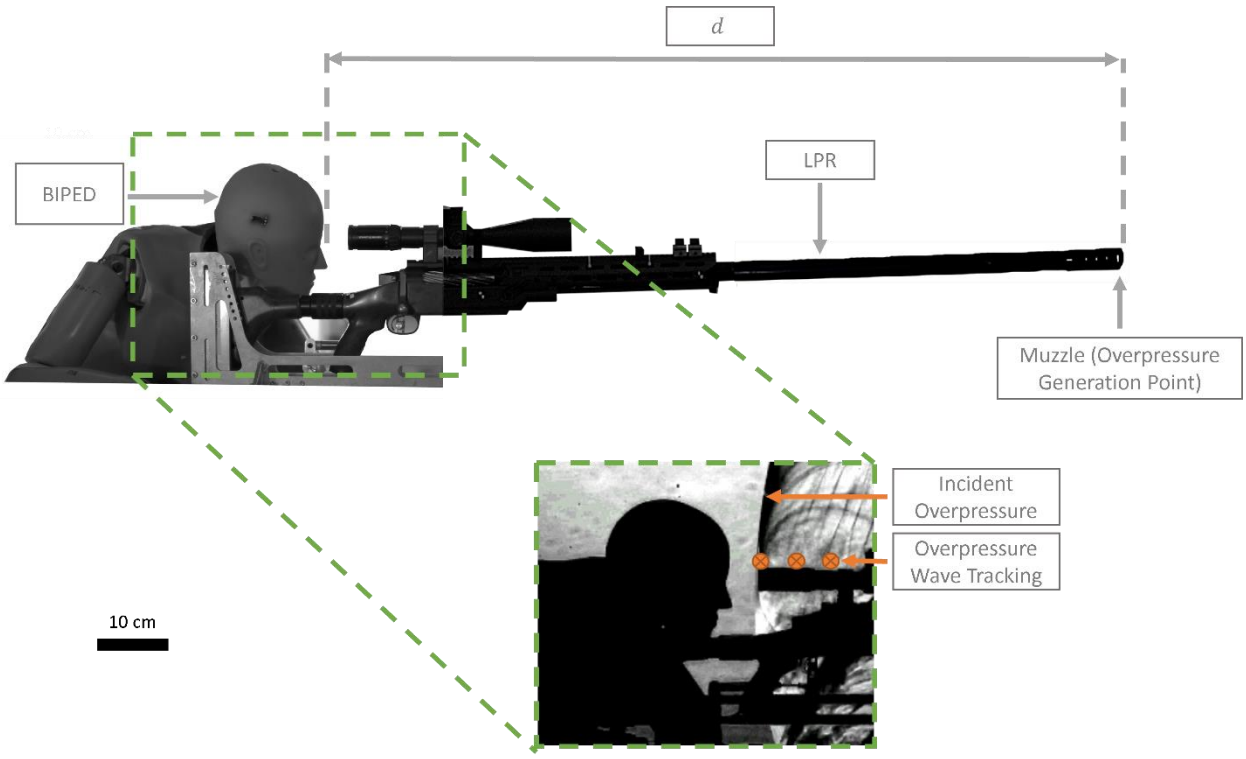


Figure 19: Schlieren video image (inset) to measure overpressure wave speed. The position of the overpressure wave was tracked and used to determine the time duration from when the rifle was fired to when the primary overpressure wave reached the head.

Finally, the adjusted kinematic and overpressure datasets were synchronized using the projectile propulsion time as an offset in the time axis. The synchronized curves were used to estimate the delay time between overpressure and kinematics effects by calculating the difference between the triggered times of both effects. Still, the delay time for cases with the non-suppressor configuration was omitted because the non-suppressor configuration session was not recorded.

# 4. Experimental Results

This section presents how the LPR discharge produced a sequence of effects that started with the overpressure effect reaching the head, followed by a delay time and a kinematic effect. While the kinematics measured in the experiments and the delay between effects depended on the operator, the overpressure measured around the head of the operator depended on the LPR configuration. These dependencies on the operator and LPR configuration were analyzed following the order of the experiments, starting with the kinematics effect, then the overpressure effect, and finally, the delay between kinematic and overpressure effects.

## 4.1. Measurement of kinematics produced by an LPR.

The kinematics depended on the LPR configuration and the operator, showing variations in the peaks and amplitude of linear accelerations and rotational velocities in two experiments. The first experiment consisted of two sessions with one operator, who discharged an LPR with the suppressor and non-suppressor configuration in each session. On the other hand, the second experiment consisted of four volunteers discharging an LPR with the suppressor configuration, showing variations in linear accelerations and rotational velocities between operators.

In the first experiment, the first session showed that the head kinematics caused by LPR with non-suppressor and suppressor configuration presented similar behavior with differences in the magnitudes (Figure 20). In both configurations, the linear acceleration gave the highest magnitudes rounding the first 75 ms with a tendency to be stable after 100 ms, and the rotational velocity fluctuated along the 250 ms with peaks before the first 100 ms. However, the magnitudes of linear accelerations and rotational velocities were higher in the suppressor configuration than in the non-suppressor configuration. The suppressor configuration obtained linear acceleration peaks 47.7%, 95.8%, and 27.3% higher than the non-suppressor configuration in axes X, Y, and Z, respectively. Furthermore, the rotational velocities caused by the suppressor configuration were 145% higher than their counterpart with the non-suppressor configuration.

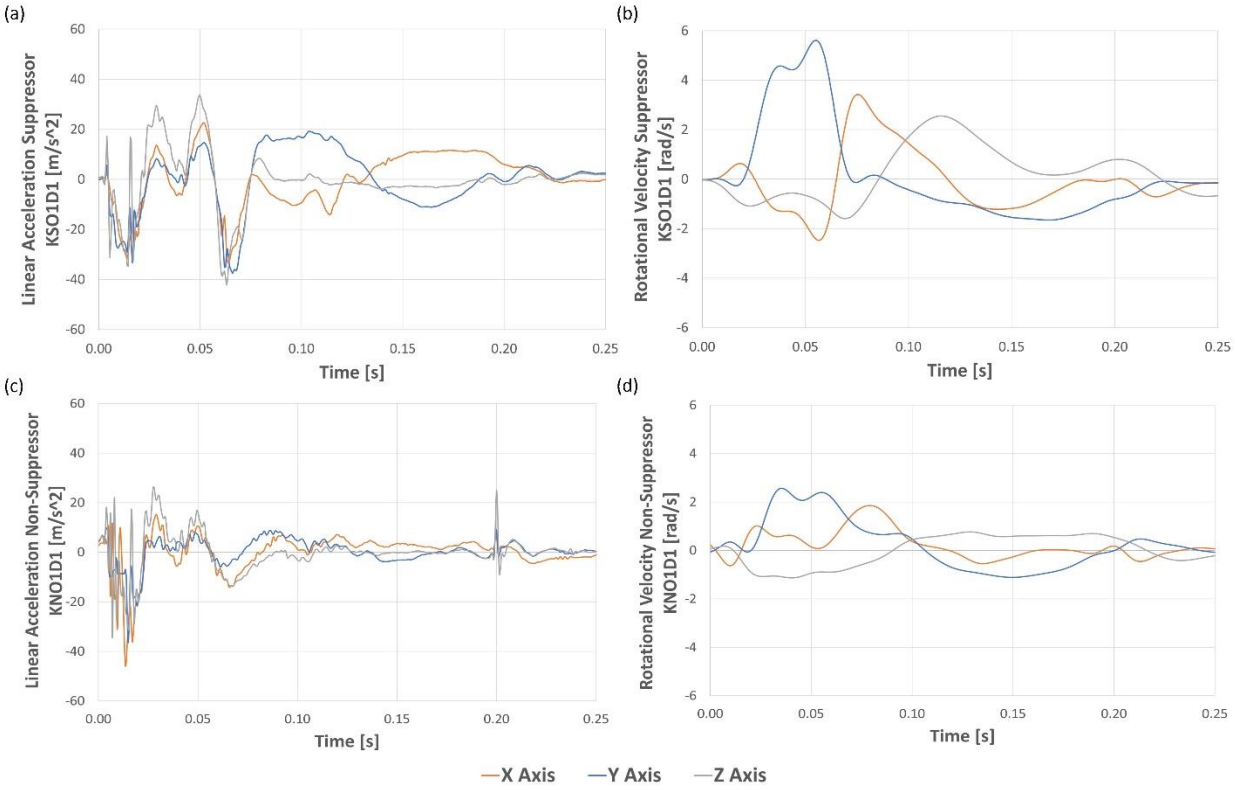


Figure 20: Kinematic measurements from non-suppressor configuration in cases KNO1D1 and suppressor configuration in case KSO1D1. Linear accelerations from non-suppressor configuration (a), rotational velocities from non-suppressor configuration (b), linear accelerations from suppressor configuration (c), and rotational velocities from suppressor configuration (d) were recorded by mouthguards and converted to the center of gravity of the head on axes X, Y, and Z.

In addition to the first experiment, the second session showed that the response of the rotational velocities to the LPR configuration concorded with the first sessions (Figure 21), showing increments in kinematics due to the suppressor. The curves presented crest and peaks with the frequency observed in the first session, and the suppressor increased the peaks of rotational velocities at 122%, 65%, and 129% in the axes x, y, and z, respectively. However, the linear accelerations caused by the discharge of the LPR with suppressor decreased by 58%, 17%, and 53% in the axes x, y, and z, respectively. This variation in the linear acceleration proposed an operator dependency, which was tested in the following kinematic experiment.

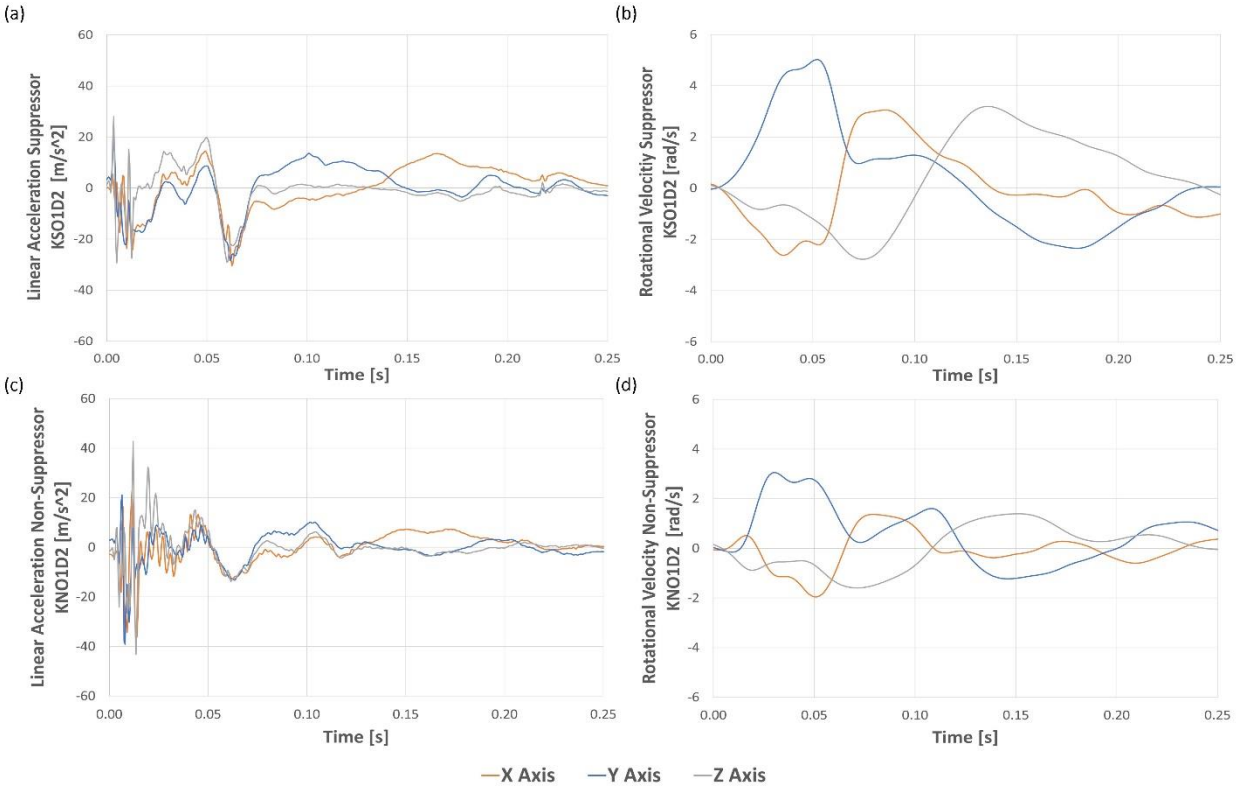


Figure 21: Kinematic measurements from non-suppressor configuration in cases KNO1D2 and suppressor configuration in case KSO1D2. Linear accelerations from non-suppressor configuration (a), rotational velocities from non-suppressor configuration (b), linear accelerations from suppressor configuration (c), and rotational velocities from suppressor configuration (d) were recorded by mouthguards and converted to the center of gravity of the head on axes X, Y, and Z.

The second experiment consisted of four operators discharging and LPR with suppressor configuration, showing variation in the linear accelerations and rotational velocities depending on the operator (Figure 22). The case KSO2D1 showed the highest variation in comparison to the other three cases, with more pronounced peaks at around 100 ms. The cases KSO2D2 and KSO2D3 presented similitudes in kinematics before 100 ms, but the rotational velocities differed after 100 ms. Finally, the case KSO2D4 showed lower fluctuations in the linear accelerations, and the rotational velocity stabilized in less time than the other cases (<100 ms).

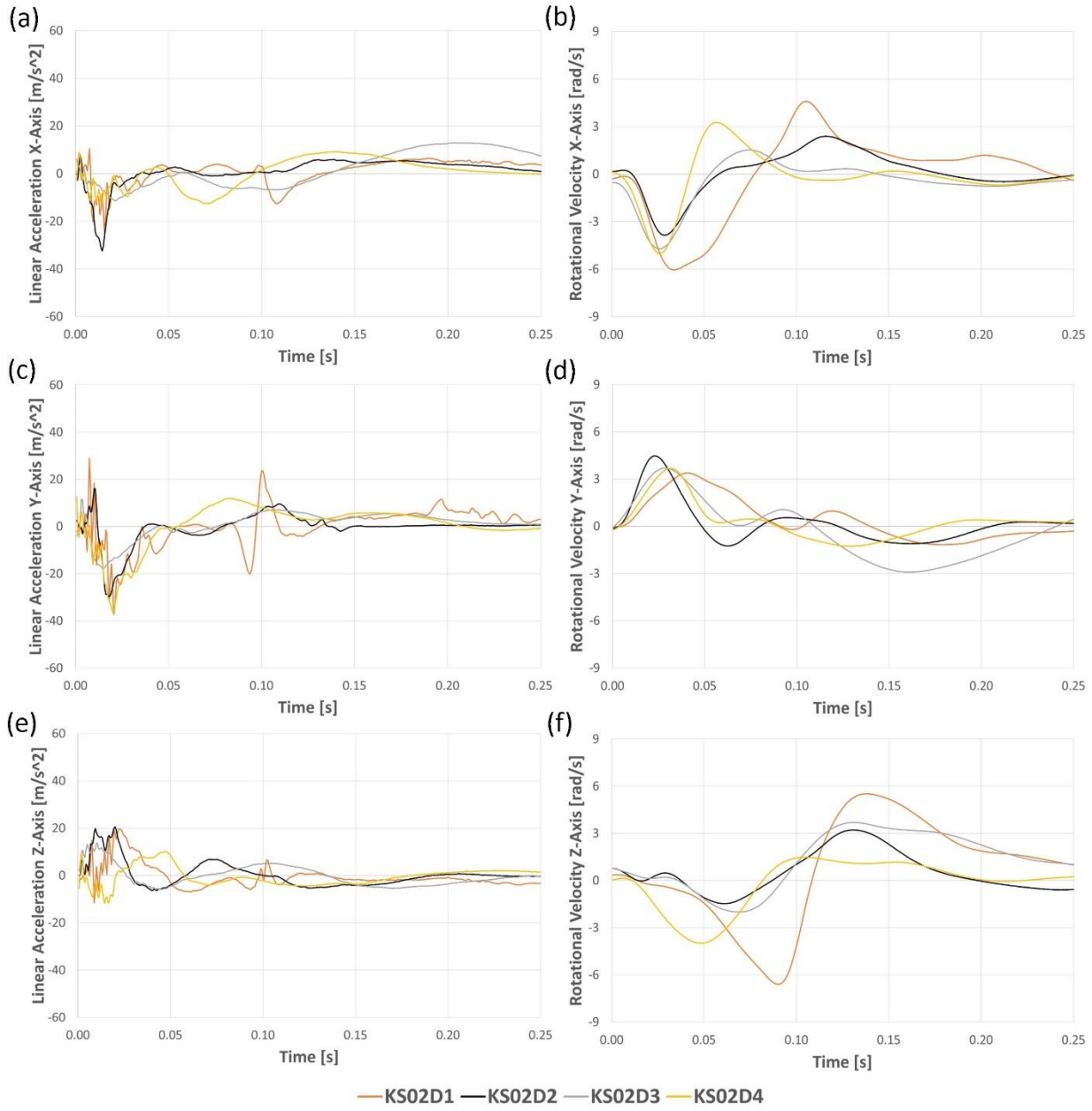


Figure 22: Kinematics obtained from LPR discharge with suppressor configuration in cases KSO2D1, KSO3D1, KSO4D1, and KSO5D1. The instrumented mouthguards recorded the linear acceleration in the x-axis (a), rotational velocity in the x-axis (b), linear acceleration in the y-axis (c), rotational velocity in the y-axis (d), linear acceleration in the z-axis (e), and rotational velocity in the z-axis (f).

## 4.2. Measurement of the overpressure produced by LPR discharge.

The overpressure experiment consisted of four LPR discharges with a non-suppressor configuration and another four LPR discharges with a suppressor configuration, assessing the effectiveness of the suppressor to attenuate the overpressure around the head. In addition to the LPR configuration dependency, the results from the non-suppressor configuration showed a consistent overpressure around the head, implying no dependency on the operator.

The overpressure on the four sensors around the BIPED was consistent through the four discharges of LPR with non-suppressor configuration (Figure 23), presenting a cross-correlation score of 0.963 (CORA, Partnership for Dummy Technology and Biomechanics, R.4.0.5, Germany) (Appendix A) with a positive phase followed by the negative phase predictable in overpressures caused by detonations (Kamimori et al., 2017; Singh & Cronin, 2019). Furthermore, the overpressure measurements presented the tendency to stabilize before the 4 ms of propagation with pressure peaks of 27.6 kPa, which below the safety range of exposure (Woodall et al., 2023). In addition, the overpressure field showed how the front side sensor registered the first overpressure on the BIPED, followed by the right and left side in parallel, and finishing with the back-side sensor. The highest peak was also recorded by the sensor on the front side of the BIPED due to receiving the first incident of overpressure, followed by the right and left side sensors measured peaks of overpressure at the same time (12 ms) with variations in overpressure peaks (5 kPa). While the results on the right and left sides implied that the BIPED received lateral overpressure in parallel, the overpressure peaks were higher on the side where the LPR was located. In contrast to the other sensors, the sensor on the back side of the BIPED received a lower magnitude of overpressure due to the propagation being attenuated by the BIPED geometry.

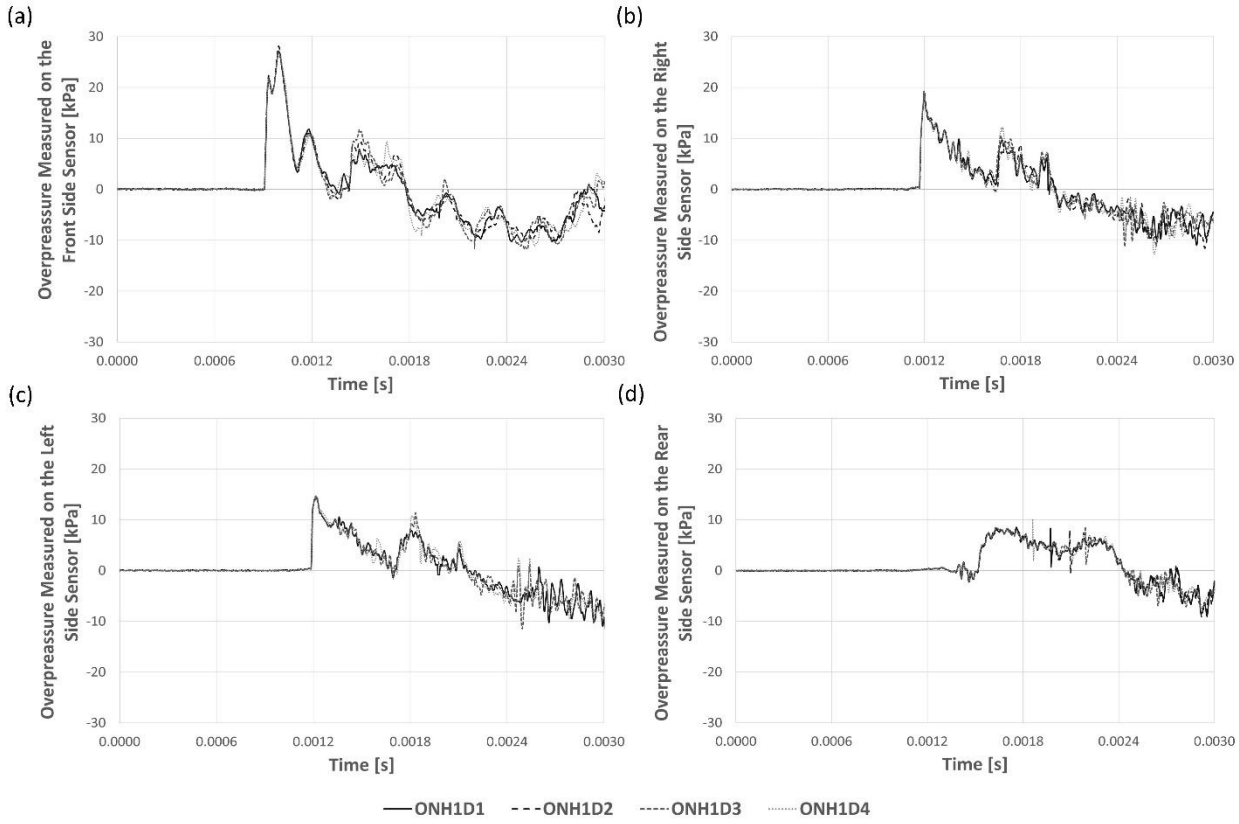


Figure 23: Overpressure measured from LPR discharges with non-suppressor configuration in the cases ONH1D1, ONH1D2, ONH1D3, and ONH1D4. The pressure sensors measured the overpressure on the front side (a), right side (b), left side (c), and rear side (d).

In contrast, the LPR with suppressor configuration showed pressures lower than 0.5 kPa in the four sensors around the BIPED (Figure 24), proving the attenuation effect of the suppressor. The results of the kinematics and overpressure experiments implied that the suppressor configuration attenuated the overpressure by increasing the rotational velocities, and the kinematics, in general, depended on the operator.

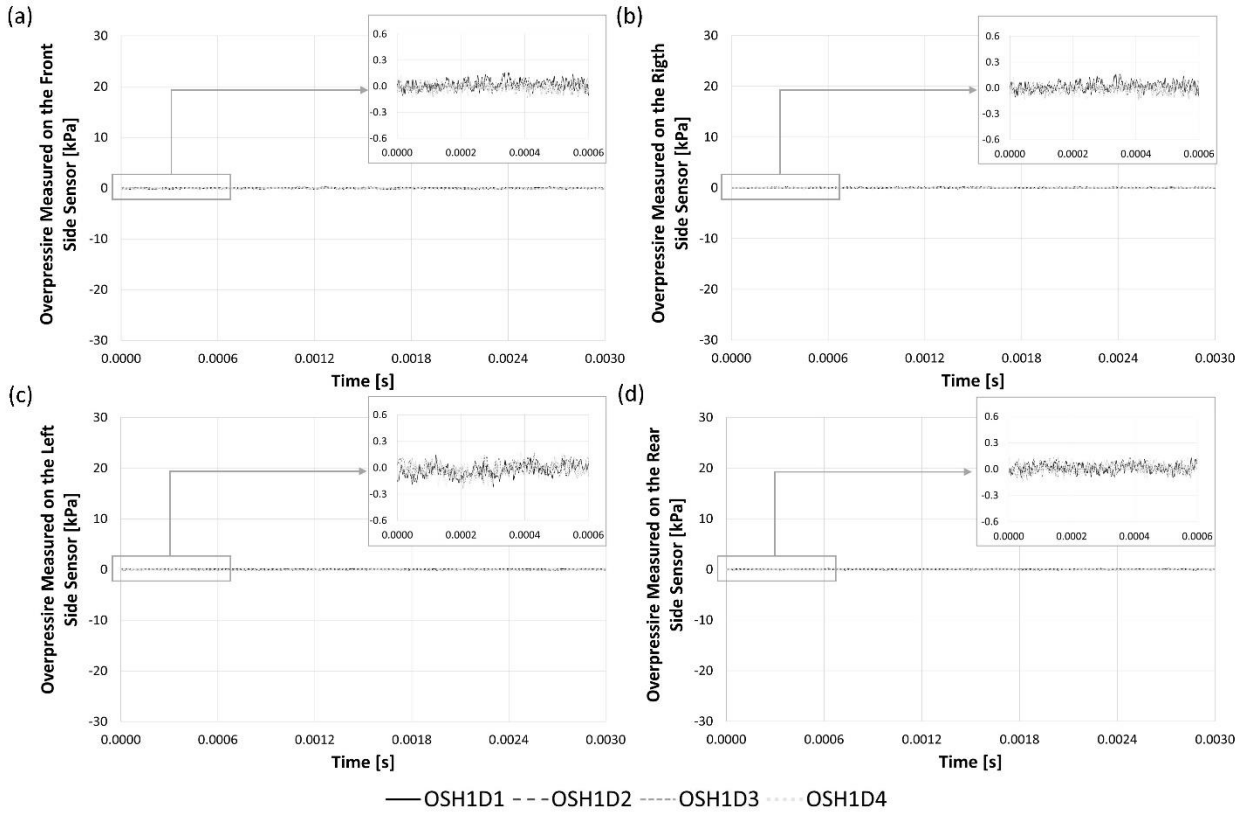


Figure 24: Overpressure measured from LPR discharges with non-suppressor configuration in the cases OSH1D1, ONS1D2, ONS1D3, and ONS1D4. The pressure sensors measured the overpressure on the front side (a), right side (b), left side (c), and rear side (d).

## 4.3. Sequence of kinematic and overpressure reactions

The overpressure and head movement curves were synchronized in time (Figure 25), showing the sequence of overpressure at 3.6 ms, followed by kinematics after a delay time between 7.4 and 24.4 ms, depending on the operator. The overpressure start time was calculated using the average overpressure wave speed with the suppressor and non-suppressor configuration of 352 m/s, and the average 1.275 m distance from the LPR muzzle (suppressor and non-suppressor) and the head of the operator. As a result, the overpressures reached the frontal sensor of the BIPED 3.6 ms after the projectile propulsion and tended to stabilize at 5 ms after the first incident of overpressure. On the other hand, the recoil head start time was measured in 11 ms, 12 ms, 28 ms, and 20 ms after the projectile propulsion for the cases KSO2D1, KSO3D1, KSO4D1, and KSO5D1, respectively.

The difference between the overpressure starting time and the head kinematics start time represented the range of delay times between overpressure and recoil head kinematics (Table 5).

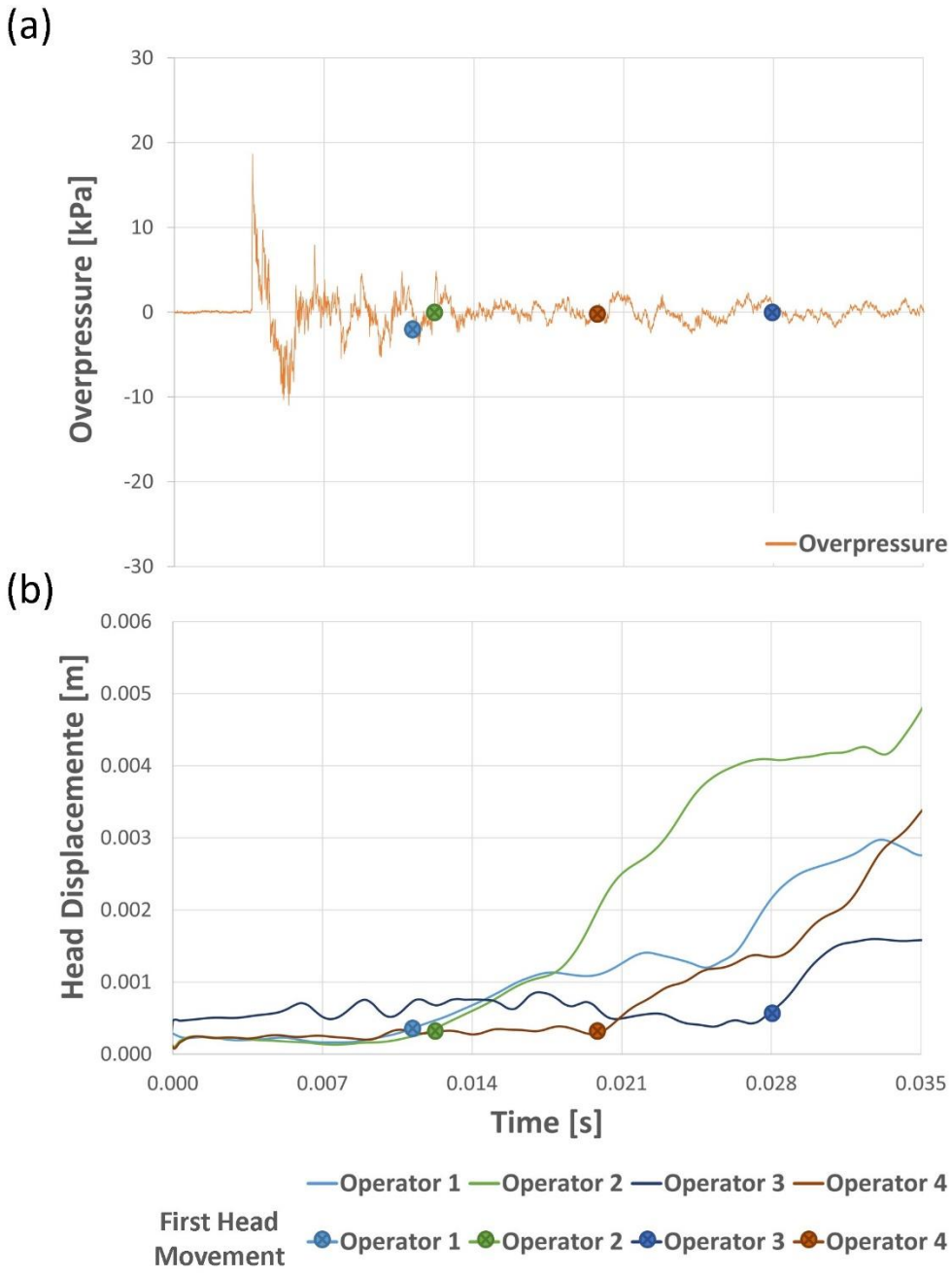


Figure 25: Synchronization of overpressure propagation and recoil head kinematics using LPR discharge time. The graph shows the time for the overpressure wave to reach each operator (a) and the head movement timing of four operators (b).

Table 5 Delay time between primary blast impact and the first head movement estimated using the overpressure start time and the kinematics start time.

| ID | Overpressure starting time [ms] | Head kinematics start time [ms] | The delay between primary overpressure impact and kinematics starts [ms] |
|---|---|---|---|
| **KSO2D1** | 3.6 | 11 | 7.4 |
| **KSO2D2** | 3.6 | 12 | 8.4 |
| **KSO2D3** | 3.6 | 28 | 24.4 |
| **KSO2D4** | 3.6 | 20 | 16.4 |

# 5. Numerical Models to Assess Head Response

This section defined the methods to study the brain response to the LPR discharge using two FE models to represent the sagittal and transverse planes of the head, applying the boundary conditions for kinematics and overpressure loads. To apply these overpressure loads, the sagittal and transverse models were defined as planar models (LS-DYNA R13.1, ANSYS Inc, Pennsylvania). rather than fully three-dimensional due to the transmission of overpressure loads requiring a high number of elements and continuum-connected surfaces (Singh & Cronin, 2019).

The boundary conditions of the models recreated the overpressure and kinematics recorded in the experimental cases, assessing the brain response dependency on the LPR configuration and operator. Initially, the collected overpressure and head recoil kinematic data were transformed into input data for the software of finite elements. Then, the simulated overpressure and head kinematics were compared against the experimental overpressure and head kinematics through cross-correlation, obtaining good agreement between the simulation and experiments. Finally, the brain response to different input data of overpressure and kinematics was assessed using tissue-level metrics response over time, cumulative volume fraction response to tissue-level metrics, and the injury brain risk.

## 5.1. Head model to assess brain response to kinematics

### 5.1.1. Head geometry and head mesh

The sagittal and transverse models were developed in previous studies (Singh et al., 2014; Singh & Cronin, 2019, 2017), which used the Visible Human Project (VHP) to obtain the head geometries (Figure 26). Notice that these geometries were meshed with 1 mm solid hexahedral elements to ensure tissue continuity and response convergence (Singh et al., 2014).

These head geometries consisted of 8 tissues for the sagittal model and 7 tissues for the transverse model, defining the parts as deformable to enable the overpressure propagation through the tissues. In addition to the parts definition, the nodes between tissue layers were merged to allow acoustic stress wave transmission.

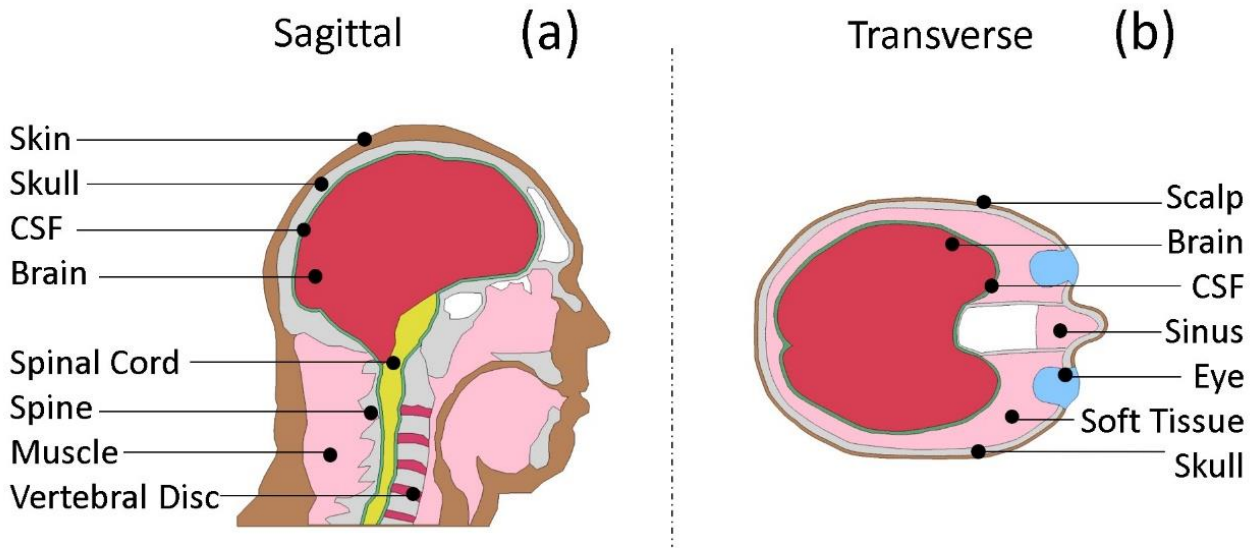


Figure 26: The sagittal (a) and transverse (b) models were used to simulate the brain response to kinematic and overpressure loads.

The VHP specified this male specimen anthropometry as a 38-year-old man with 2.8 m tall and 90.2 kg weight, scanned post-mortem (Spitzer et al., 1996). Notice that these anatomical image layers counted with a resolution of 0.33 mm, which provided enough resolution to distinguish the tissue layers.

Many modeling approaches have traditionally favored tetrahedral elements due to their computational efficiency; however, they are susceptible to generating inflated pressure values due to issues like hydrostatic locking. Conversely, solid hexahedral elements have been found to exhibit more reliable convergence in scenarios involving overpressure exposures (Singh, 2015).

### 5.1.2. Constitutive Model Materials

The sagittal and transverse models were defined using different material models and properties depending on the tissue (Table 6), including the skull/vertebrae, vertebral disc, skin, muscle/soft tissue, CSF, and the brain (Singh, 2015; Singh et al., 2014; Singh & Cronin, 2019).

Table 6: Material properties used in the sagittal and transverse models extracted from (Singh, 2015).

| Tissue | Model Material | Density ($Kg/m^3$) | Poisson's Ratio | Young's Mod. (Pa) | Bulk Mod. (Pa) |
|---|---|---|---|---|---|
| **Skull/Vertebrae** | Elastic | 1561 | 0.379 | 7.92e9 | - |
| **Vertebral Disc** | Elastic | 1040 | 0.400 | 3.40e6 | - |
| **Skin** | Elastic | 1200 | 0.420 | 1.70e9 | - |
| **Muscle/Soft Tissue** | Hyperelastic | 1050 | - | - | 2.2e9 |
| **CSF** | Elastic Fluid | 1040 | - | - | 2.2e9 |

The skull/vertebrae, vertebral disc, and skin were modeled as an elastic material (*MAT_ELASTIC in LS-DYNA), anticipating that these tissues do not present large deformations under the established boundary conditions. These elastic materials were characterized by Poisson's ratio and Young's modulus.

The muscle and soft tissue were modeled with the hyperelastic material model for strain rate-dependent simplified rubber (*MAT_SIMPLIFIED_RUBBER/FOAM in LS-DYNA) (Lockhart, 2010; Van Sligtenhorst et al., 2006). The characterization of these hyperelastic materials was based on the bulk modulus, which defined how these materials react to external pressure by resisting changes in their volume.

The CSF was modeled as an elastic fluid (*MAT_NULL in LS-DYNA) that did not present shear resistance due to the fluid shear resistance being negligible in this study case. In specific, the hourglass module (*HOURGLASS in LS-DYNA) was increased to 0.15 implementing this modification through the Flanagan-Belytschko viscous formulation (LS-DYNA ®, 2021, pp. 24-1). This adjustment in the Hourglass module introduced artificial energy to prevent non-physical deformations in the bottom of the sagittal head geometry, considering the absence of an inferior border (Figure 32a).

Finally, the brain was defined as one part using the linear viscoelastic constitutive model (*MAT_VISCOELASTIC in LS-DYNA), assuming an isotropic material in a homogeneous continuum. This assumption has demonstrated favorable outcomes in prior investigations (Singh et al., 2014; Wittek & Omori, 2003) where brain material properties were considered uniform across the entire brain (Singh & Cronin, 2019). Notice that this linear viscoelastic material was

defined using shear relaxation response (Equation 8), where $G_\infty$ was the long-time shear modulus, $G_0$ was the short-time shear modulus, and $\beta$ was the decay constant.

$$G(t) = G_\infty + (G_0 - G_\infty)e^{-\beta t} \quad (8)$$

The constants necessary to define the brain material were 2.2 GPa, 1050 Kg/m$^{3,}$ 15900 Pa, 3600 Pa, and 504.5 s$^{-1}$ for Bulk Modulus, Density, $G_\infty$, $G_0$, and $\beta$, respectively (Zhu et al., 2013).

### 5.1.3. ALE method and meshing

The overpressure propagation was modeled using the ALE method, which required the head mesh to be surrounded by a mesh to represent the air. Note that to simulate the overpressure produced by the LPR, this air mesh was defined as a viscous fluid model with the properties of the air. Then, the sagittal and transverse meshes were coupled to the air mesh in different models, creating independent simulations with the interaction between air and the respective head mesh.

The geometry of the air mesh served the primary objective of maintaining ample clearance around the head mesh, thereby mitigating undesired reflective overpressure effects on the models (Figure 27a). The air mesh itself took the form of a 2.20x2.05 m square, with a front line of air elements (leading edge of air mesh) positioned in front of the head mesh, serving as the initial boundary for the propagation of air overpressure.

The element size was refined around the head to couple the meshes through the ALE method without affecting the computational efficiency. This refinement consisted of reducing the size of the elements from 40 mm in the corners of the square to 1 mm in the perpendicular lines crossing the head mesh (Figure 27b) (LS-DYNA ®, 2021; Singh & Cronin, 2019). Notice that we applied a 10% size differential relative to the adjacent elements.

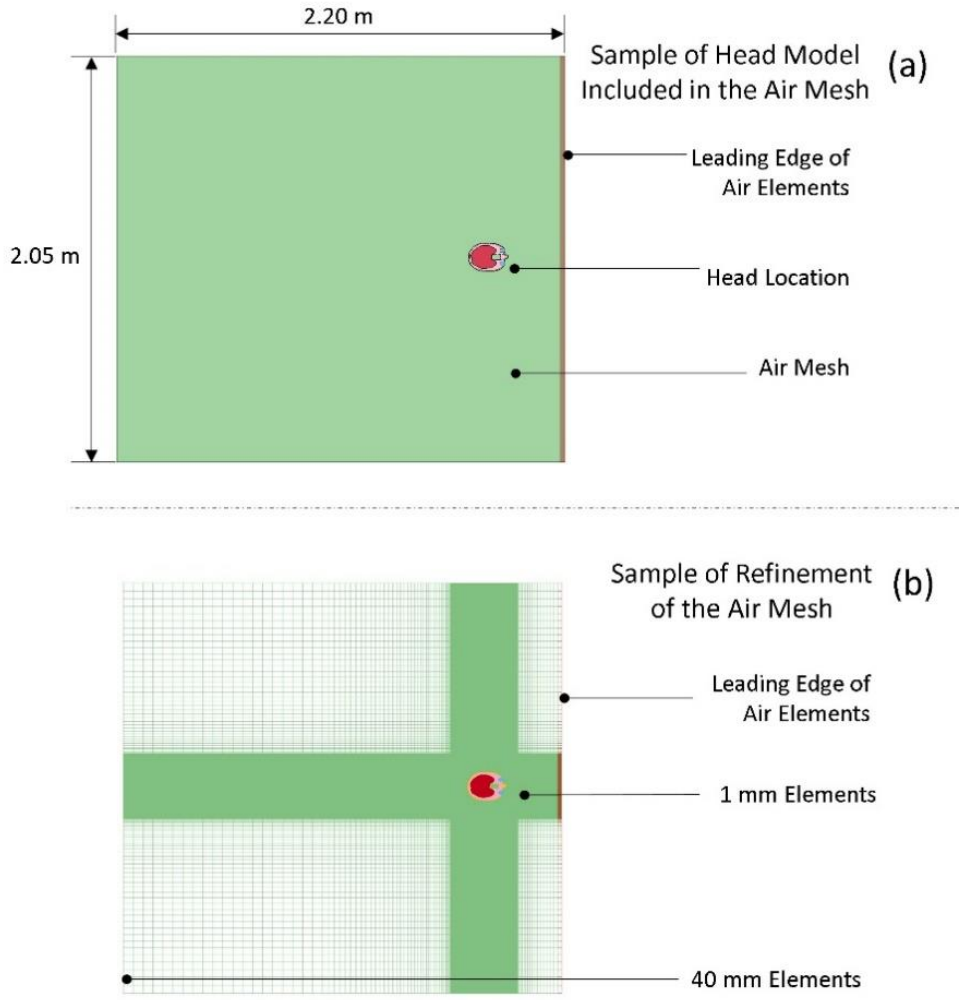


Figure 27: Example of the head model (transverse) included in the air mesh (a) and the refinement of the air mesh (b) used to simulate the brain response to overpressure propagation.

The air mesh material was defined as a viscous fluid model through the ideal gas equation (Equations 9, 10), assuming the initial air state as standard air conditions at atmosphere pressure (Table 7). Initially, the air material properties were established by incorporating density ($\rho$) and dynamic viscosity ($\mu$). Subsequently, the ideal gas equation was employed to define pressure ($P_i$) as a function of gas density ($\rho_i$), heat capacity ($C_{v0}$ and $Cp_0$), and temperature ($T_i$). Finally, any variation in the gas density was determined based on the relative volume ($\upsilon_i$). It is worth noting that heat capacity ($C_{v0}$ and $Cp_0$) was assumed to remain constant ($C_L/C_Q$) throughout the analysis.

$$P_i = \rho_i(Cp_i - Cv_i)T_i \quad (9)$$

$$\frac{v_i}{v_0} = \frac{\rho_0}{\rho_i} \quad (10)$$

Table 7: Material properties and ideal gas law parameters

| $\rho_0$ [Kg/m3] | $\mu$ [Pa*s] | $C_{v0}$ [J/K] | $C_{p0}$ [J/K] | $C_L/C_Q$ [J/K] | $T_0$ [K] | $v_0$ |
|---|---|---|---|---|---|---|
| 1.205 | 1.821e-5 | 717.860 | 1005.000 | 0.000 | 293.150 | 1.000 |

## 5.2. Boundary conditions to assess brain response to the head kinematics effect.

The linear acceleration and rotational velocities for one case of LPR discharge with non-suppressor configuration (Figure 28) were used to represent a baseline case. Note that this case was previously transformed into the head coordinate system in Section 3.1.

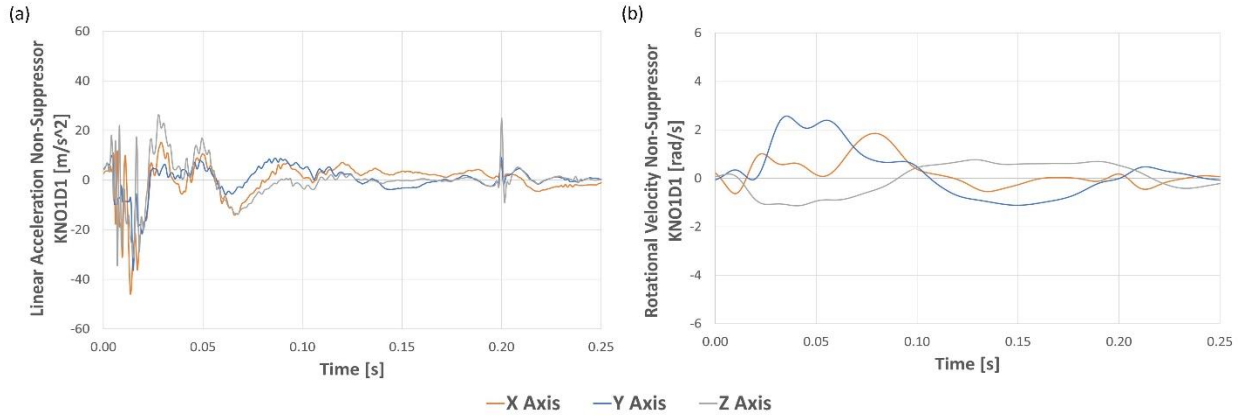


Figure 28: The linear acceleration (a) and rotational velocity (b) in the head coordinate system representing the head kinematics caused by an LPR discharge with the non-suppressor configuration (KNO1D1).

To define the boundary conditions for the sagittal and transverse models, the linear accelerations and rotational velocities had to be processed to obtain nodal forces. This transformation consisted of four consecutive steps applied through a custom-written script (MATLAB R2022a) (Appendix

E). First, the rotational angles between the head coordinate system and the model coordinate system were calculated (Figure 29a). Second, these rotational angles were used to transform the linear accelerations and rotational velocities into the model coordinate system (Figure 29b). Third, the linear accelerations and rotational velocities were distributed between the sagittal and transverse models (Figure 29c). Finally, the linear accelerations and rotational velocities were transformed into nodal forces (Figure 29d).

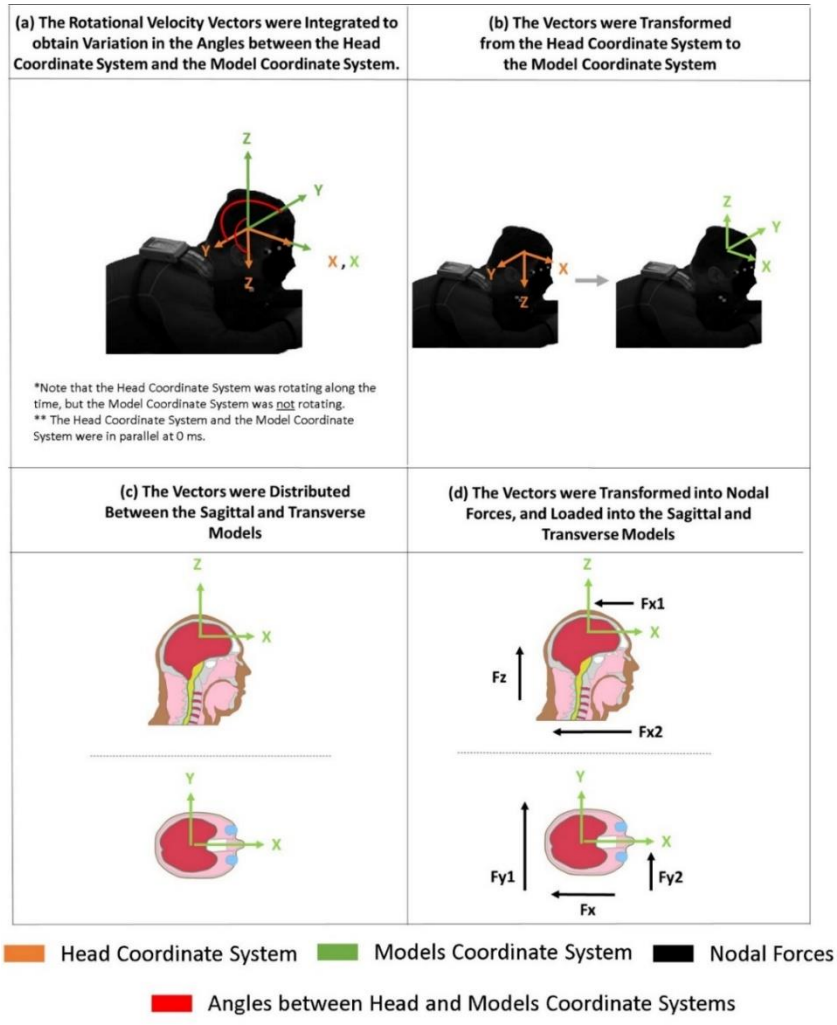


Figure 29: Process to obtain the kinematic boundary conditions. First, the head coordinate system was aligned with the model coordinate system (a), Second, the vectors were transformed to the model coordinate system (d). Third, the vectors were distributed between the sagittal and transverse models (e). Finally, the vectors transformed into nodal forces(d)

### 5.2.1. Step 1: Angles between Head Coordinate System and Model Coordinate System

The axes from the head coordinate system rotated along the time, but the model coordinate system did not rotate. For this reason, θ, β, and α were defined as the rotational angles between the head and model coordinate system, being θ, β, and α rotations around the axes X, Y, and Z, respectively.

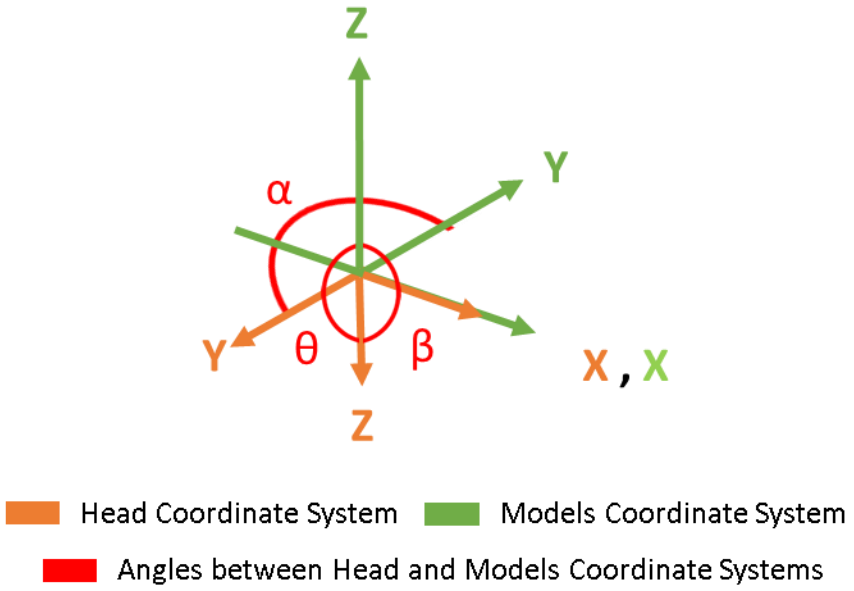


Figure 30: Rotational angles θ, β, and α rotations around the axes X, Y, and Z, respectively.

$\Theta$, $\beta$, and $\alpha$ were calculated by integrating the rotational velocities vectors ($w_{local}$), which were measured in the head coordinate system. Note that this integration was applied using the midpoint method from 0 to 250 ms, defining an increment of 0.001 ms ($\Delta t$) (Equation 11). In addition, the initial values between the head and the model coordinate system were defined at 180 degrees around the x-axis ($\theta_0$), 0 degrees around the y-axis ($\beta_0$), and 0 degrees around the z-axis ($\alpha_0$) (orientation based on right-hand rule and counterclockwise positive conventions).

$$(\theta \quad \beta \quad \alpha) = (\theta_0 \quad \beta_0 \quad \alpha_0) + \sum_{i=1}^{n} \left( w_{local} * \frac{\Delta t}{2} \right) \tag{11}$$

### 5.2.2. Step 2: Transformation of Kinematics from Head Coordinate System to Model Coordinate System

To transform the linear acceleration ($a_{local}$) and rotational velocities vectors ($w_{local}$) into the model coordinate system ($a_{global}$ and $w_{global}$), $a_{local}$ and $w_{local}$ were multiplied by the rotational matrix ® (Equations 12, 13). Notice that $R$ was defined by the multiplication of rotational components (Equation 14), which consisted of the rotation in axis X ($R_x$) (Equation 15), the rotation in axis Y ($R_Y$) (Equation 16), and the rotation in axis Z ($R_Z$) (Equation 17).

$$a_{global} = R * {a_{local}}^T \tag{12}$$

$$w_{global} = R * {w_{local}}^T \tag{13}$$

$$\mathrm{R} = R_z * R_y * R_x \tag{14}$$

$$R_x = \begin{bmatrix} 1 & 0 & 0 \\ 0 & \cos\theta & -\sin\theta \\ 0 & \sin\theta & \cos\theta \end{bmatrix} \tag{15}$$

$$R_y = \begin{bmatrix} \cos\beta & 0 & \sin\beta \\ 0 & 1 & 0 \\ -\sin\beta & 0 & \cos\beta \end{bmatrix} \tag{16}$$

$$R_z = \begin{bmatrix} \cos\alpha & -\sin\alpha & 0 \\ \sin\alpha & \cos\alpha & 0 \\ 0 & 0 & 1 \end{bmatrix} \tag{17}$$

### 5.2.3. Step 3: Distribution of Kinematics between Sagittal and Transverse Model

Once the linear acceleration and the rotational velocity were transformed into the model coordinate system, their components were distributed between the sagittal and transverse models (Figure 31). The sagittal model received the linear acceleration in the x-axis, the linear acceleration in the z-axis, and the rotational velocity in the y-axis. On the other hand, the transverse model received the linear acceleration in the x-axis, the linear acceleration in the y-axis, and the rotational velocity in the z-axis. Noticed that neither the sagittal model nor the transverse model was defined to simulate the rotational velocity in the x-axis, accepting this rotational velocity as a limitation of the models.

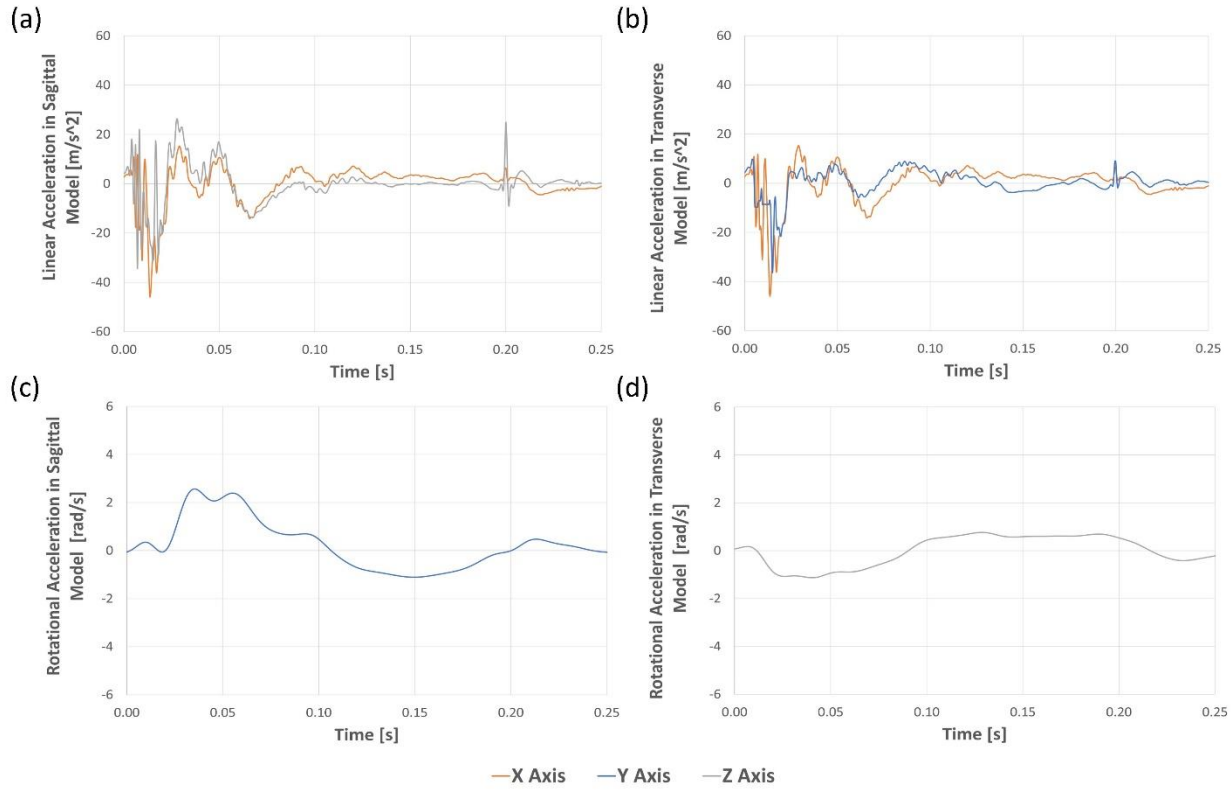


Figure 31: Distribution of linear acceleration into the sagittal model (a), linear acceleration into the transverse model (b), rotational velocity into the sagittal models (c), and rotational velocity into the transverse models (d).

### 5.2.4. Step 4: Transformation of Kinematics into Nodal Forces

The kinematics were applied to the skull parts in the sagittal and transverse models, but these skull parts were defined as non-rigid (Section 5.1.1.). The non-rigid definition implied that the skull parts did not admit rotational velocities as boundary conditions but did admit nodal forces as boundary conditions. Therefore, the boundary conditions were defined through nodal forces, which produced the required linear accelerations and rotational velocities. These nodal forces were calculated for sagittal and transverse models using the second law of Newton for linear accelerations and moment of inertia (Figure 32), obtaining the moment of inertia (angular acceleration) by applying numerical derivation to the rotational velocity.

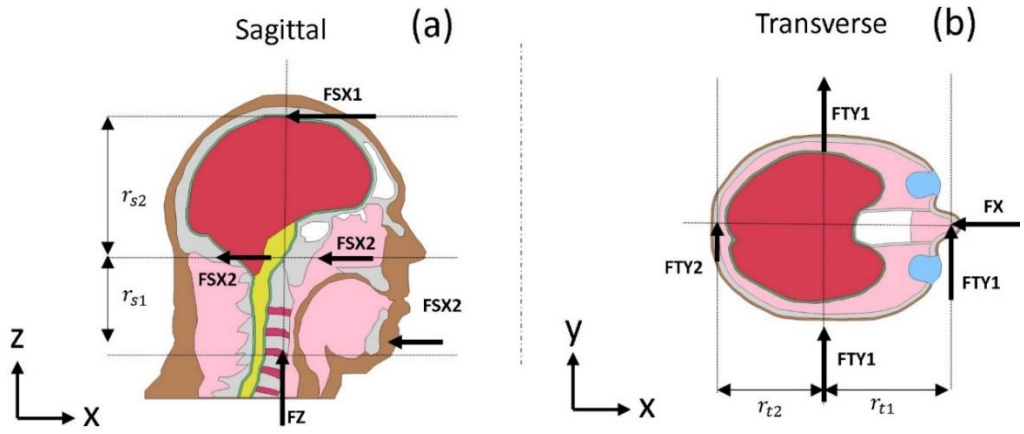


Figure 32: Free body diagram calculates the nodal forces related to the kinematic curves in sagittal (a) and transverse (b) models.

In the sagittal model (Figure 32a), one force was applied along the z-axis ($FZ$) to mimic the acceleration in the z-axis ($a_z$) (Equation 18). Furthermore, a torque was generated through the combination of one force $FSX1$ and three forces $FSX2$, which collectively reproduced both the acceleration in the x-axis ($a_x$) (Equation 19) and the rotational acceleration in the y-axis ($\alpha_y$) (Equation 20).

$$FZ = m_s * a_z \tag{18}$$

$$3 * FSX2 + FSX1 = m_s * a_x \tag{19}$$

$$FSX1 * r_{s1} - FSX2 * r_{s2} = I_s * \alpha_y \tag{20}$$

In the transverse model (Figure 32b), one force was applied along the x-axis ($FX$) to mimic the acceleration in the x-axis ($a_x$) (Equation 21). Furthermore, a torque was generated through the combination of one force $FTY1$ and three forces $FTY2$, which collectively reproduced both the acceleration in the y-axis ($a_y$) (Equation 22) and the rotational acceleration in the z-axis ($\alpha_z$) (Equation 23).

$$FX = m_T * a_x \tag{21}$$

$$3 * FYT1 + FYT2 = m_T * a_y \tag{22}$$

$$FYT1 * r_{T1} - FYT2 * r_{T2} = I_T * \alpha_z \tag{23}$$

It is noteworthy that the constants representing mass ($m_s$ and $m_T$), moment of inertia ($I_s$ and $I_T$), and the distance between the center of gravity and the nodal force ($r_{s1}, r_{s2}, r_{T1}$, and $r_{T2}$ ) were determined based on measurements taken from the sagittal and transverse models (Table 8).

The entire process of nodal forces calculation was applied through a custom-written script (MATLAB R2022a) (Appendix F), and the simulated kinematics were validated against the experimental kinematics (CORA) (Appendix A).

Table 8. Constants of mass, moment of inertia, and distance between the center of gravity and the nodal force used to calculate the nodal forces in sagittal and transverse models.

| Model | Variable | Notation | Value |
|---|---|---|---|
| **Sagittal** | Mass [kg] | $m_s$ | 0.058900 |
| **Sagittal** | Moment of Inertia [kg·m$^2$] | $I_s$ | 0.000497 |
| **Sagittal** | Distance FSX1 [m] | $r_{s1}$ | 0.098450 |
| **Sagittal** | Distance FSX2 [m] | $r_{s2}$ | 0.086450 |
| **Transverse** | Mass [kg] | $m_T$ | 0.023600 |
| **Transverse** | Moment of Inertia [kg·m$^2$] | $I_T$ | 0.000097 |
| **Transverse** | Distance FTY1 [m] | $r_{T1}$ | 0.131500 |
| **Transverse** | Distance FTY2 [m] | $r_{T2}$ | 0.058500 |

Finally, the brain response was measured using the injury metrics discussed in Section 5.1.4.

## 5.3. Boundary conditions to assess brain response to the overpressure effect

In both the sagittal and transverse models, the measured overpressure was applied using the ALE air elements. This process necessitated replicating the overpressure data at the leading edge of the air mesh by considering gas properties as boundary conditions.

It is important to note that the measured overpressure data exhibited low variability (Section 4.3). Consequently, the sagittal and transverse models were loaded with the overpressure data from a specific case where a non-suppressor configuration was employed (ONH1D1) (Figure 33). More precisely, the overpressure data from the right side was used to calculate the appropriate boundary conditions, aiming to achieve sensor measurements devoid of reflective overpressure.

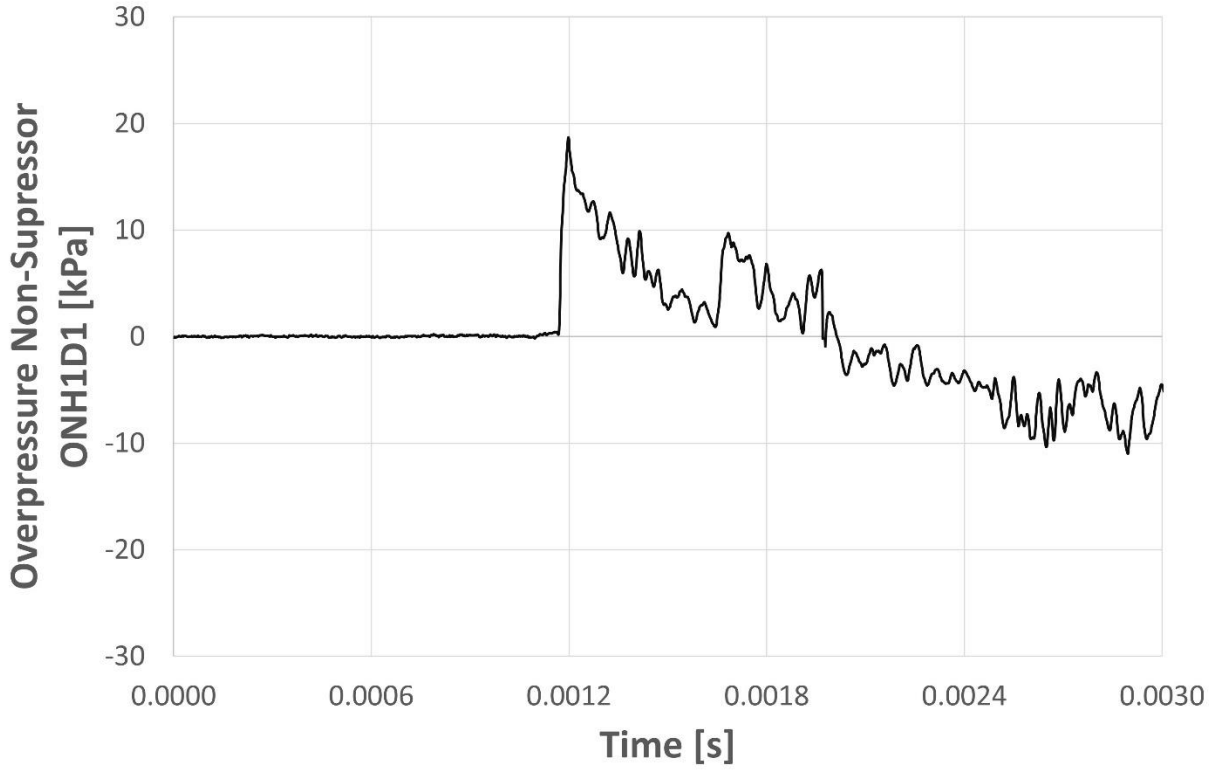


Figure 33: Overpressure recorded from a non-suppressor configuration case (ONH1D1), which was used to define the boundary conditions for the FE models.

The accuracy of the simulated overpressure was validated by comparing it with the measured overpressure from all four sides of the BIPED using cross-correlation (CORA) (Appendix A). Differences in both length and amplitude were observed between the simulated and measured overpressure data. To address these disparities, an iterative approach was employed.

This iterative process (Figure 34) involved adjusting the length and amplitude of the measured overpressure, recalculating the boundary conditions, simulating the overpressure, and comparing the results with the measured overpressure data. This cycle was repeated until an acceptable level of agreement (cross-correlation score exceeding 0.8) between the simulated and measured overpressure was achieved. Once acceptable overpressure results were achieved, as indicated by a, the brain response was measured using the injury metrics (Section 5.1.4.)

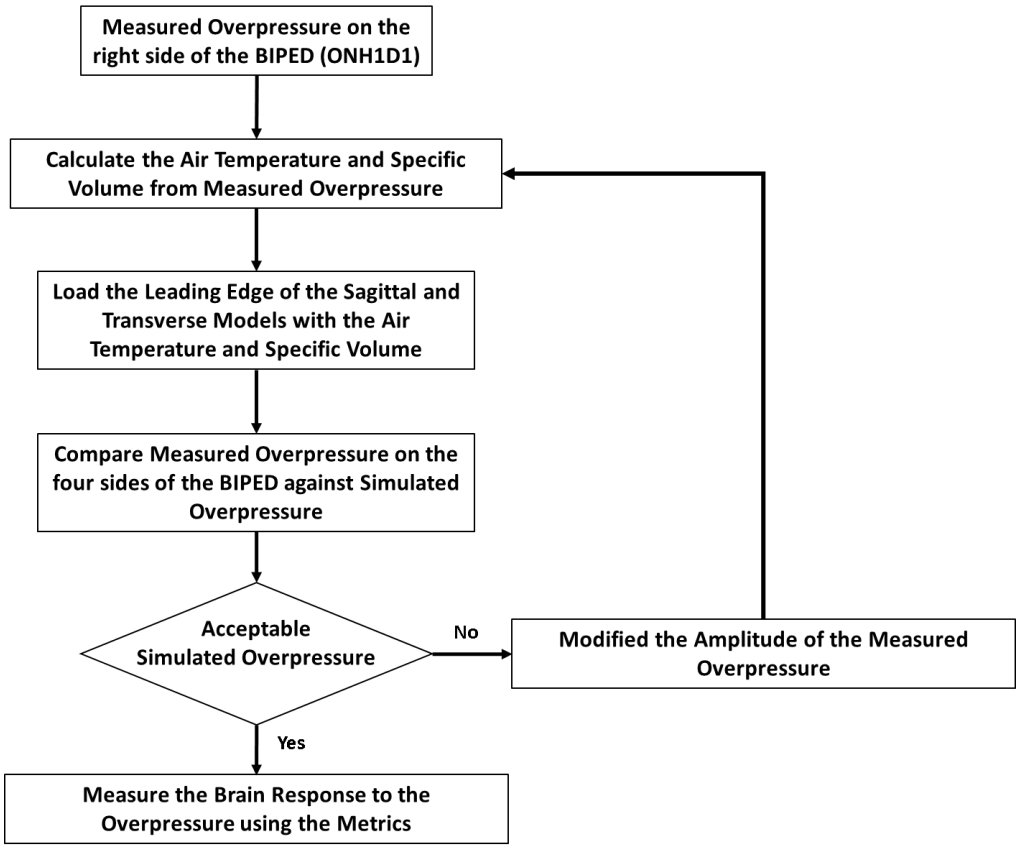


Figure 34: Iteration process applied to calculate the boundary condition (overpressure) caused by the LPR discharge.

Note that the gas properties in our study were characterized using the air temperature and specific volume. These parameters were derived by applying the Rankine-Hugoniot relation (Equations 24, 25) based on previous work (Pal & Mitra, 2021) to the measured overpressure.

$$\vartheta = \left( \frac{7 + \frac{P - P_{atm}}{P_{atm}}}{7 + 6 * \frac{P - P_{atm}}{P_{atm}}} \right) \tag{24}$$

$$T = T_{atm} * \vartheta * \left(1 + \frac{P - P_{atm}}{P_{atm}}\right) \tag{25}$$

The air atmosphere conditions were defined as 101.325 kPa ($P_{atm}$) and 293 K ($T_{atm}$).

## 5.4. Boundary conditions to assess brain response to the combined head kinematics and overpressure effect

The sagittal and transverse models were loaded with a sequence of the overpressure and the kinematic boundary conditions (Figure 35), applying an offset over the kinematic curves equal to the 8.4 ms to represent delay between both effects (Section 4.3.). Note that the off set started 1 ms after the calculated delay time because the overpressure in the simulation took 1 ms to reach the head. In addition, the air mesh and coupling were deleted (*DELETE_PART, DELETE_FSI and RESTART option in LS-DYNA) to reduce the number of elements (computational time), applying these delete after 6 ms when the overpressure tended to stabilize.

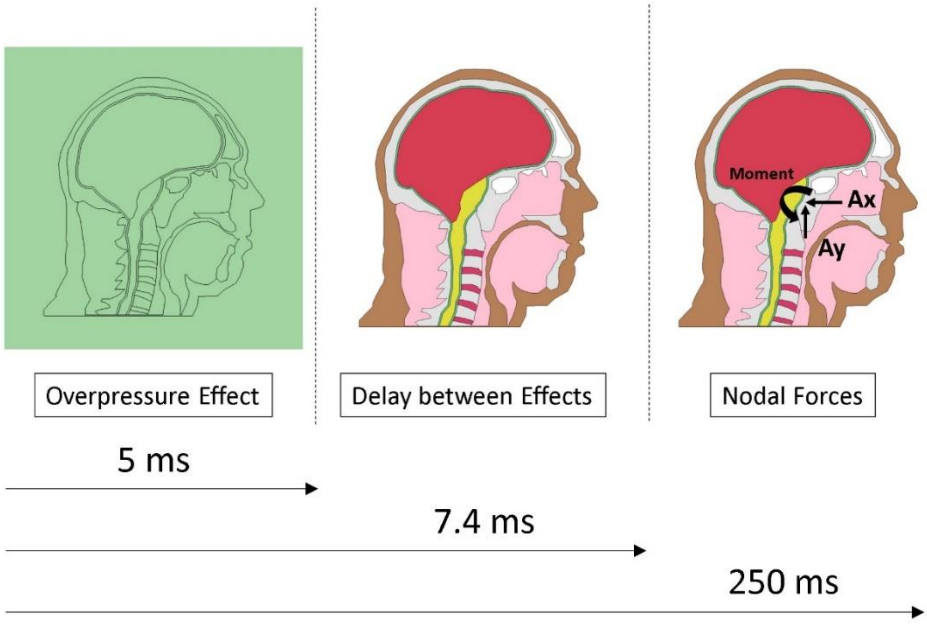


Figure 35: Example of the sequence of boundary conditions applied on the sagittal head model to simulate the combined effect between overpressure and kinematics.

The brain response was measured using the metrics (Section 5.1.4.) and compared against the model with kinematics and overpressure boundary conditions.

## 5.5. Boundary conditions to assess brain response to the variation in delay time between head kinematics and overpressure effect

There were variations in delays between the overpressure and the kinematic effects (Section 3.1.3.), obtaining a range of possible delays between 7.4 and 24.4 ms. To verify the delay effect over the brain response, five possible delay times (Table 9) were selected from the calculated range of values (equally spaced) and applied to the sagittal and transverse models as kinematics offset. Then, the brain response was measured using the injury metrics (Section 3.1.4.). Note that this delay time comparison was delimited by using the overpressure and kinematic input from one test of the LPR with a non-suppressor configuration (KNO1D1 and ONH1D1) to reduce the variables within simulations.

Table 9: Delay times between overpressure and kinematics used in the delay sensitivity comparison.

| **Delay Time [ms]** | 7.40 | 11.65 | 14.90 | 19.15 | 23.40 |
|---|---|---|---|---|---|
| **Kinematic Offset [ms]** | 6.40 | 10.65 | 14.90 | 19.15 | 23.40 |

To clarify the kinematics offset, the overpressure reached the head geometry in the simulation after 1 ms, causing that the kinematic offset had to be shift in 1 ms.

## 5.6. Boundary conditions to assess brain response to the suppressor and non-suppressor configuration

The suppressor and non-suppressor configurations altered the head kinematics and overpressure, and these alterations were assessed through calculating corresponded curve for the boundary conditions (head kinematics and overpressure). These boundary conditions were obtained from two overpressure test (Figure 36) and four kinematic tests (Figure 37, Figure 38), which combined the head kinematics with overpressure (

Table 10) to represent the suppressor and non-suppressor configurations. Note that the simulation variables were delimited using a constant delay time between head kinematics and overpressure (7.40 ms).

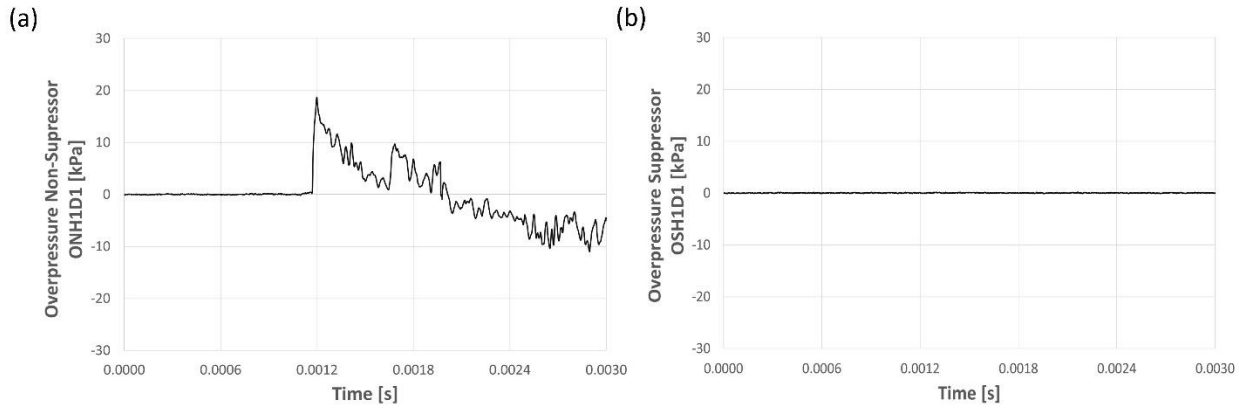


Figure 36: Experimental data used to simulate the overpressure effect under non-suppressor (a) and suppressor (b) configuration.

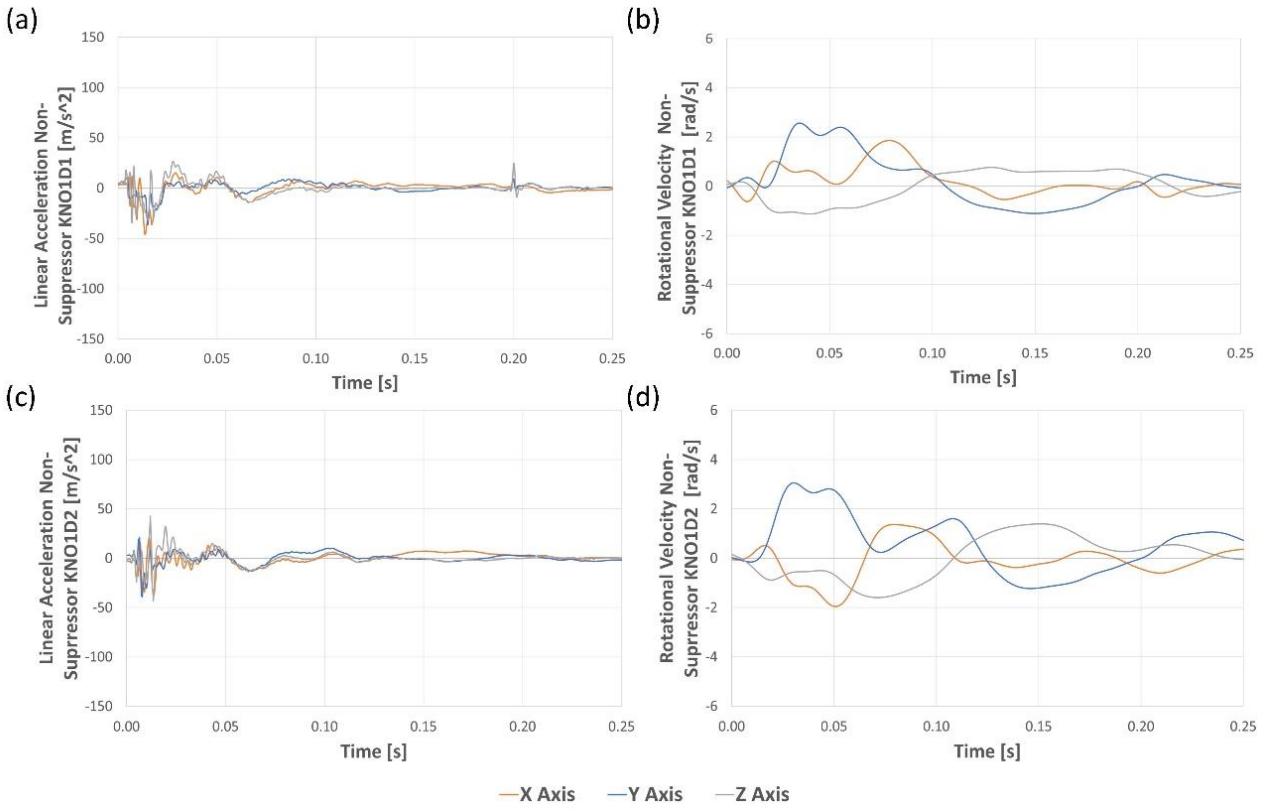


Figure 37: Experimental data used to simulate the head kinematics caused by non-suppressor configuration. The boundary conditions were calculated from linear acceleration KNO1D1 (a), rotational velocity KNO1D1 (b), linear acceleration KNO1D2 (d), and rotational velocity KNO1D2 (d)

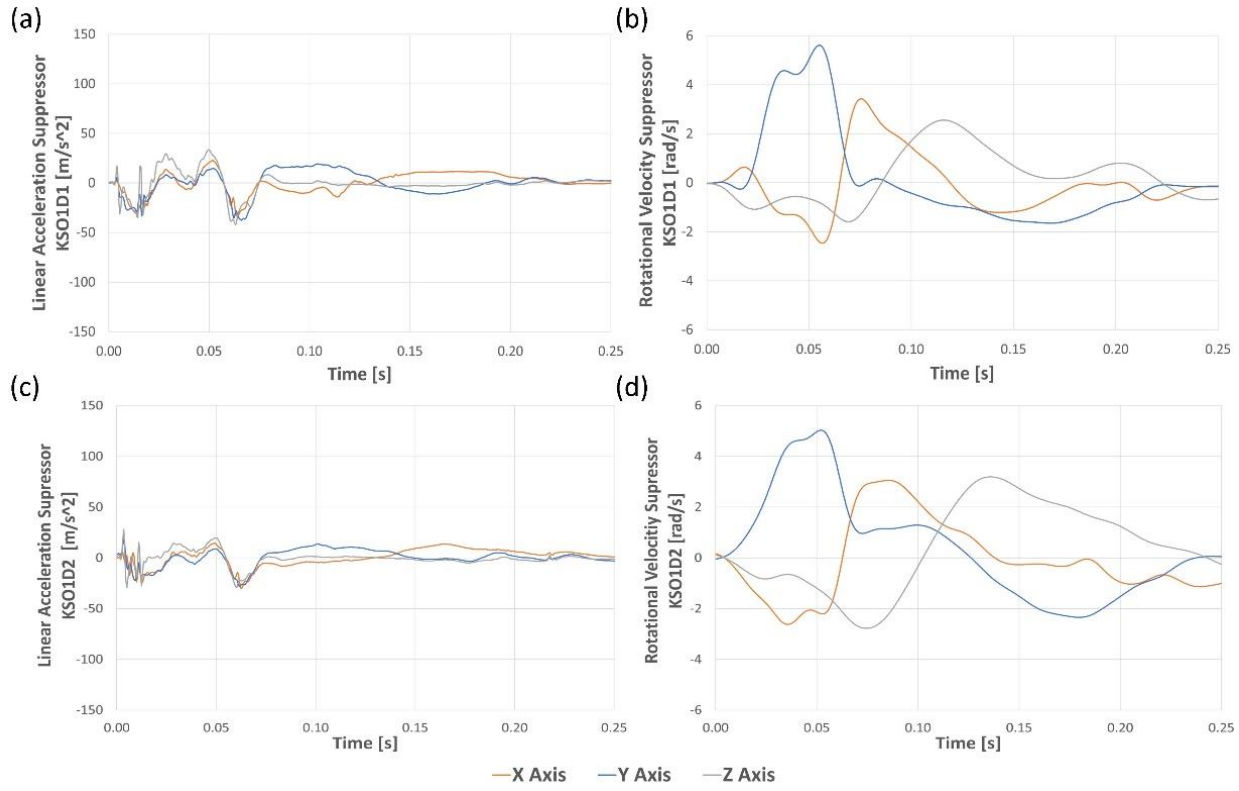


Figure 38: Experimental data used to simulate the head kinematics caused by suppressor configuration. The boundary conditions were calculated from linear acceleration KSO1D1 (a), rotational velocity KSO1D1 (b), linear acceleration KSO1D2 (d), and rotational velocity KSO1D2 (d)

Table 10: Combination of boundary conditions to represent cases with suppressor and non-suppressor configurations.

| Overpressure Test ID | Head Kinematics Test ID | LPR Configuration |
|---|---|---|
| OSH1D1 | KNO1D1 | Non-Suppressor |
| OSH1D1 | KNO1D2 | Non-Suppressor |
| ONH1D1 | KSO1D1 | Suppressor |
| ONH1D1 | KSO1S2 | Suppressor |

Finally, the brain response was compared to asset the relation between brain response mitigation and the LPR configuration.

## 5.7. Metrics used to assess brain response

Three kinds of metrics were used to assess the brain response to the boundary conditions caused by the LPR response. The first one was the tissue-level metrics over time, which were plotted to identify how the metric behavior changed due to the boundary conditions. The second one was the cumulative volume fraction response to tissue-level metrics, which was plotted to identify the extent of the brain response to the boundary conditions. The third one was brain injury probability metrics, using the head injury criterion (HIC15) and a new metric proposed in previous studies (Lyu et al., 2022).

The tissue-level metrics over time were analyzed with the 95$^{th}$ percentile of maximum principal strain ($MPS_{95}$), the 5$^{th}$ percentile of intracranial pressure ($ICP_5$), and the 95$^{th}$ percentile of intracranial pressure ($ICP_{95}$) over a duration of 250 milliseconds. Notice that the selection of percentiles for these metrics was deliberate and aimed to mitigate the influence of artificial peaks in these metrics, and these data was extracted using custom-written script (Python 3.9) (Aleksander Lukasz Rycman, 2022). In this context, the 95$^{th}$ percentile represents the maximum value, while the 5$^{th}$ percentile represents the minimum value within our dataset.

The cumulative volume fraction response to tissue-level metrics represented the fraction of brain volume reaction to the maximum principal strain (MPS), positive intracranial pressure (positive ICP), and negative intracranial pressure (negative ICP). This method was applied through the following steps (Seeburrun et al., 2023) using a custom-written script (MATLAB R2022a, MathWorks, California, USA) (Appendix A and Appendix B).

1. The initial volume for each element along the simulation was extracted, including the corresponding maximum value of the metric (*VM*). Notice that the negative ICP was calculated with the minimum value instead of the maximum.
2. The initial volume of each element ($VOL_i$) was divided by the total brain volume ($VOL_{brain}$), obtaining the element volume fraction ($VF_i$) (Equation 26).

$$VF_i = \left(\frac{VOL_i}{VOL_{brain}}\right) * 100 \quad 1. \quad (26)$$

3. The *VM* of the elements was sorted in ascending order, including the corresponding element volume fraction.

4. There was defined a cumulative volume fraction ($CVF_i$), which started in $CVF_{i=0}$ equal to 1. Then, the volume fraction of each element ($VOL_i$) was subtracted from the cumulative volume fraction, since $i = 0$ until the last elements ($N$) (Equation 27). Notice that the ascendent order in the VM was conserved.

$$CVF_{i+1} = \sum_{i=0}^{N} (CVF_i - VF_{i+1}) \tag{27}$$

The HIC15 (Equation 28) estimated brain injury risk to linear accelerations $a(t)$ in a period $(t_2 - t_1)$ 15 ms (Schmitt et al., 2019a), using a commercial post-processing (LS-PrePost v4.8). While the standardized metrics of HIC15 applied to car collisions, the metric was used to have a reference to compare the injury probability by LPR discharges with the injury probability by other sources.

$$HIC15 = \max_{t_1,t_2} \left\{ (t_2 - t_1) * \left[ \frac{1}{t_2 - t_1} \int_{t_1}^{t_2} a(t)dt \right]^{2.5} \right\} \tag{28}$$

Finally, Zhang et al. proposed a new method (Equations 29, 30) to estimate the concussion risk ($P.Concussion$) based on MPS ($MPS_{peak}$) and positive ICP ($ICP_{peak}$). This method was obtained through the Weibull curves in simulation cases of concussion (Lyu et al., 2022), using the average maximum metric in the top ten element.

$$P.Concussion = \frac{1}{1 + e^{-9.184 * MPS_{peak} + 4.195}} \tag{29}$$

$$P.Concussion = \frac{1}{1 + e^{-0.02394 * ICP_{peak} + 3.8606}} \tag{30}$$

Note that this equation was applied to the historical results of the elements through a custom-written script (MATLAB R2022a) (Appendix D).

# 6. Head Models Response to Kienamtics and Overpressure Loads

This section presents the estimated brain response to the kinematics and overpressure loads caused by an LPR discharge. This brain response was obtained through the FE head models and evaluated using the metrics presented in Section 5.7.

## 6.1. Brain response to head kinematics

The experimental head kinematics (Section 4.1) were transformed into load forces (Section 5.2) to be simulated in the sagittal and transverse models. The simulated kinematics were compared against the experimental kinematics, obtaining cross-correlation scores of 0.808 and 0.875 for the sagittal and transverse models, respectively. These cross-correlation scores showed that both models presented close alignment between simulated and experimental linear accelerations, although slight discrepancies were observed in the rotational velocities.

It is important to notice that these simulated rotational velocities were obtained with the torque caused by nodal forces and were not loaded as direct boundary conditions, causing the difference between the experiment and the models. Despite this difference, the cross-correlation scores showed good agreement, validating that the head models effectively captured the head kinematics generated by the recoil effect induced by LPR (Figure 39).

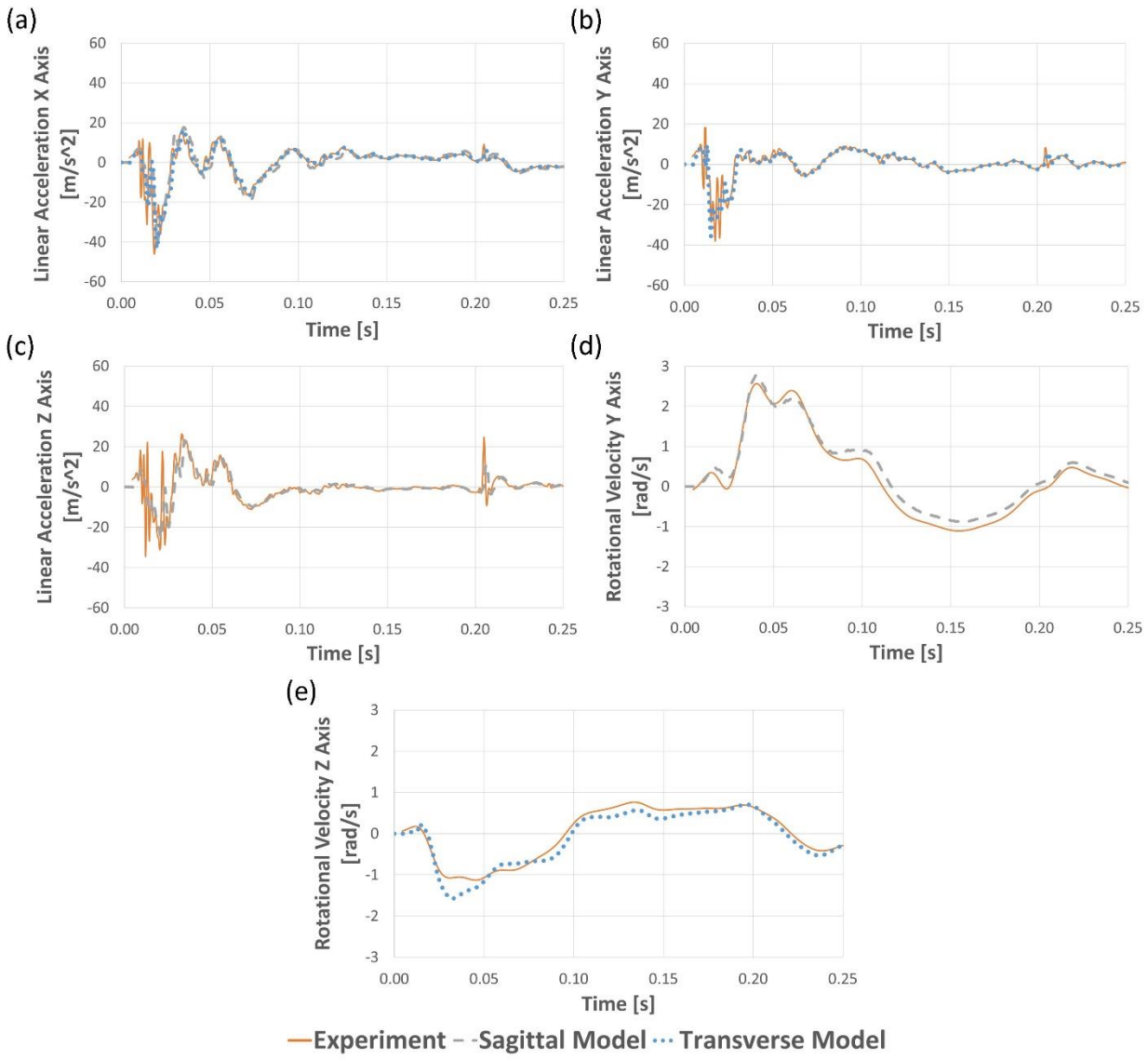


Figure 39: Comparison between the experimental kinematics and simulated kinematics, comparing the linear acceleration in the x-axis (a), linear acceleration in the y-axis (b), linear acceleration in the z-axis (c), rotational velocity in the y-axis (d), and rotational velocity in the z-axis (c).

The kinematic boundary conditions produced MPS and ICP in the brain (Figure 40), with the MPS having the more noticeable effect. Specifically, the MPS was focalized in the midbrain area (Figure 41a), producing peaks of 0.0277 m/m and 0.0406 m/m in the sagittal and transverse models, respectively. On the other hand, the ICP was concentrated in the sagittal model (Figure 41a), which presented a positive peak of 18.86 kPa and a negative peak of 12.43 kPa. However, these values were below the range of threshold for brain injury risk (Gabler et al., 2016; Panzer et al., 2012;

Takhounts, Craig, Moorhouse, Mcfadden, et al., 2013), which are 0.2 m/m, -70 kPa, and 50 kPa for MPS, negative ICP, and positive ICP, respectively.

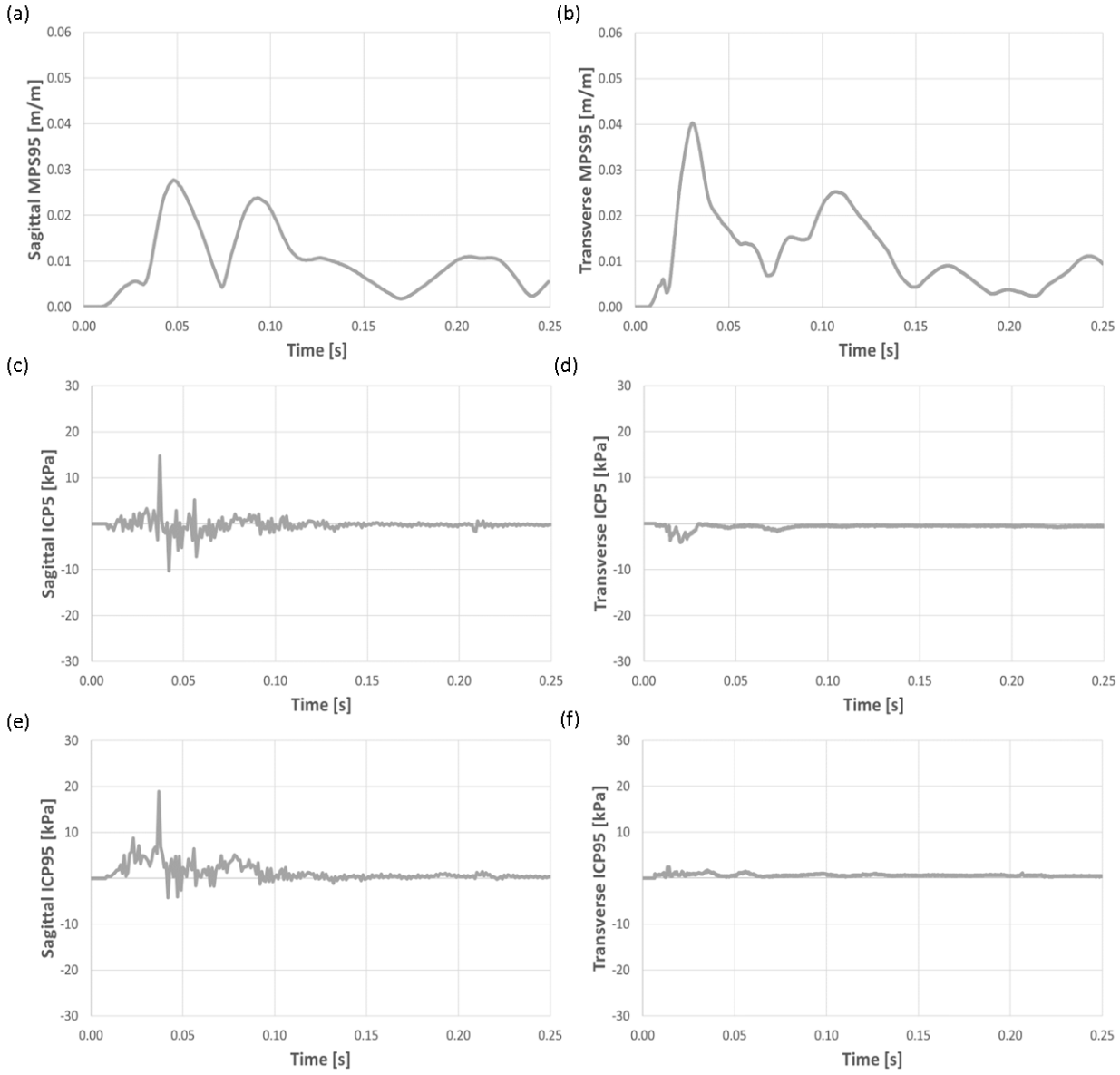


Figure 40: Brain response to the kinematic effect measured using $MPS_{95}$ in the sagittal model (a), $MPS_{95}$ in the transverse model (b), $ICP_5$ in the sagittal model (c), $ICP_5$ in the transverse model (d), $ICP_{95}$ in the sagittal model (e), $ICP_{95}$ in the transverse model and (f).

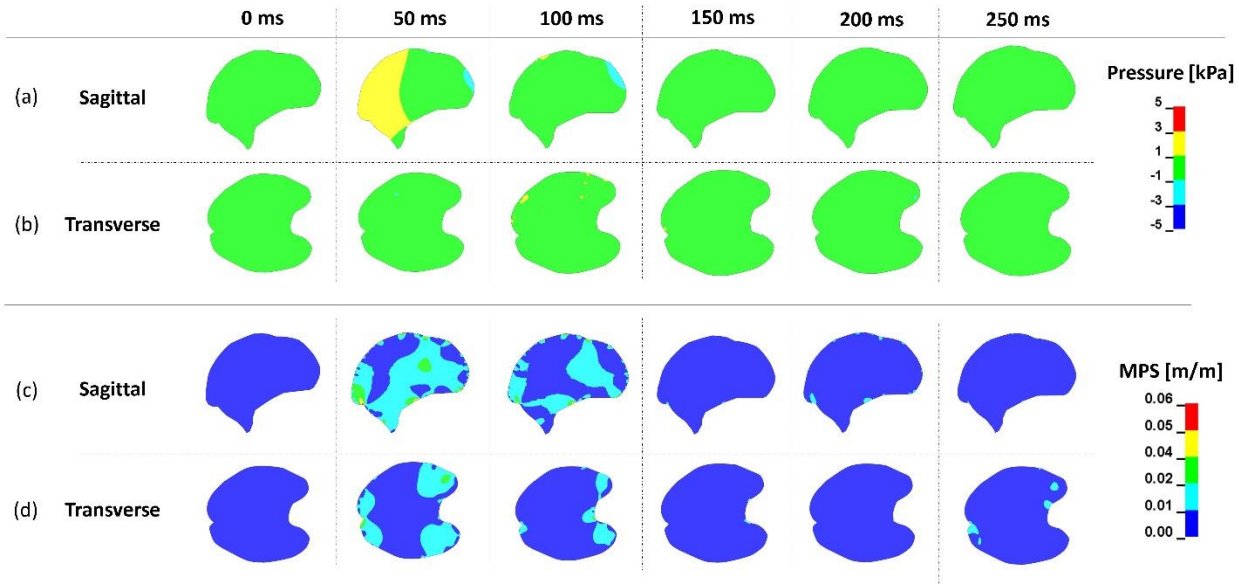


Figure 41: Distribution of pressure and strain produced by the kinematic load on the brain model (50 ms increment). The brain response was measured not only by ICP in sagittal (a) and transverse (b) models but also by MPS in sagittal (c) and transverse (d) models.

## 6.2. Brain response from overpressure in the head model.

The pressure histories of the elements around the four sides of the head (Figure 42) were used to calculate the cross-correlation score between the four experimental datasets and the simulated overpressure, obtaining scores of 0.764, 0.771, 0.758, and 0.762 for the front, right, left and back sides respectively. These results and the visual correspondence between the experimental data and the simulation of the head models (Figure 43) imply a correct overpressure boundary condition applied to the head models.

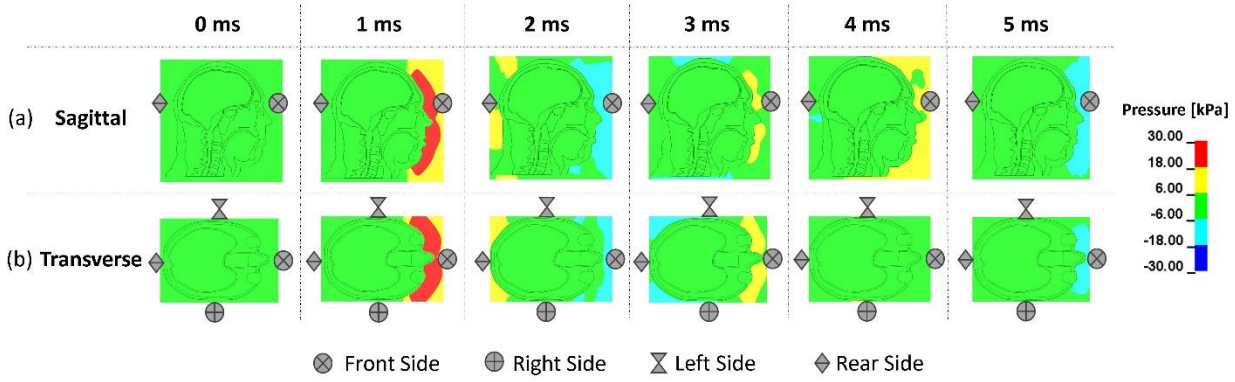


Figure 42: Elements around the head models used to measure the variation in overpressure along the time in the sagittal (a) and transverse (b) models.

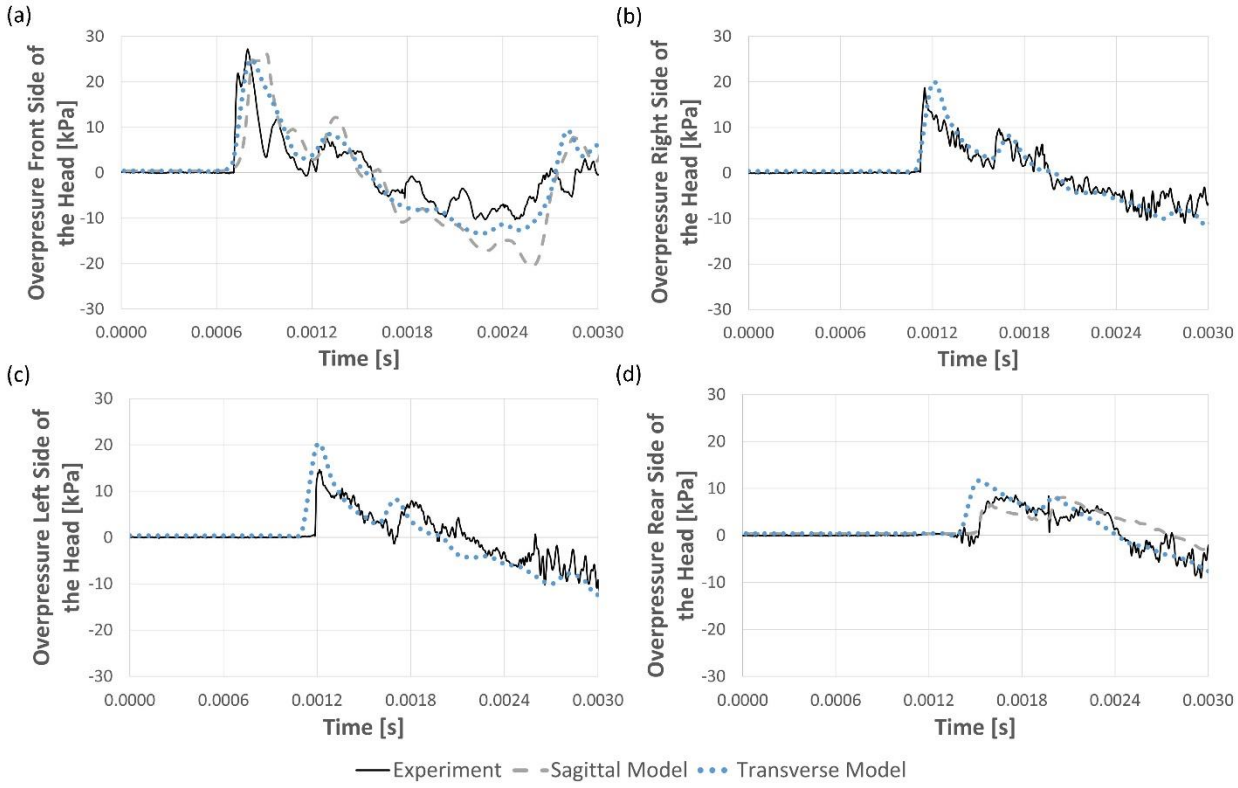


Figure 43: Comparison between the experimental data and the simulated overpressure of the BIPED and head models on the front side (a), right side (b), left side (c), and rear side (d).

Experimental data from a test conducted with a non-suppressor configuration (ONH1D1) served as the input for simulating the response of the brain to the overpressure generated by the LPR. It is important to note that despite Section 4.3 presents the results of four overpressure tests with a non-suppressor configuration, these results presented minimal variation among them, with an average cross-correlation score of 0.963. Consequently, the simulation consolidated the overpressure data into a single test.

In contrast to the kinematic loads discussed in Section 6.2, the overpressure load resulted in noticeable variations in ICP while showing negligible changes in the MPS over time (Figure 45). Specifically, the positive ICP peaks were primarily concentrated in the anterior to posterior regions of the brain, while negative ICP peaks were concentrated in the inferior brain. These positive and negative ICP peaks were measured at 16.09 kPa and -15.32 kPa, respectively, and were predominantly observed in the sagittal section (Figure 45). In contrast, the overpressure load produced no discernible impact on the MPS.

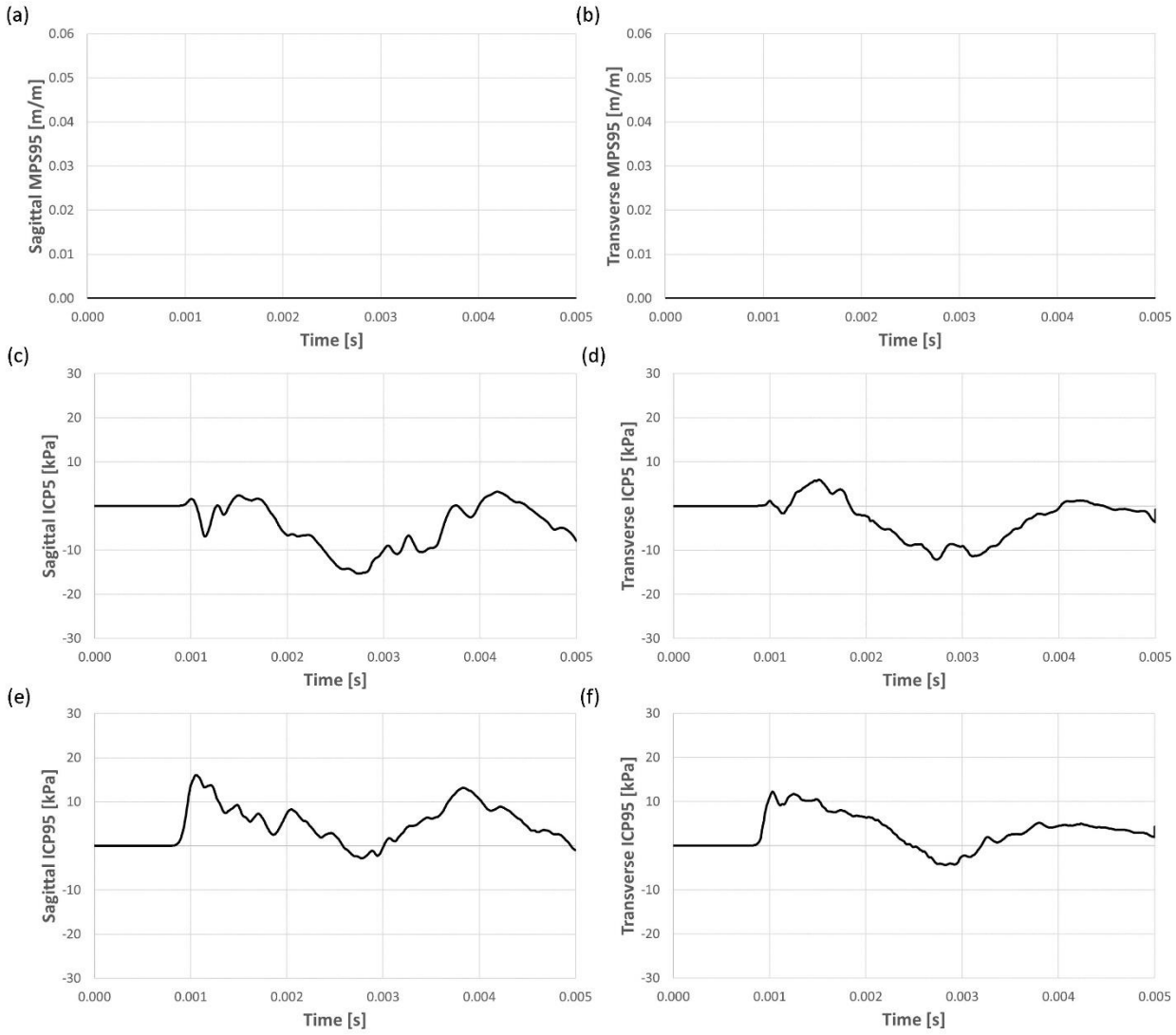


Figure 44: Brain response to the overpressure load measured using $MPS_{95}$ in the sagittal model (a), $MPS_{95}$ in the transverse model (b), $ICP_5$ in the sagittal model (c), $ICP_5$ in the transverse model (d), $ICP_{95}$ in the sagittal model (e), $ICP_{95}$ in the transverse model (f).

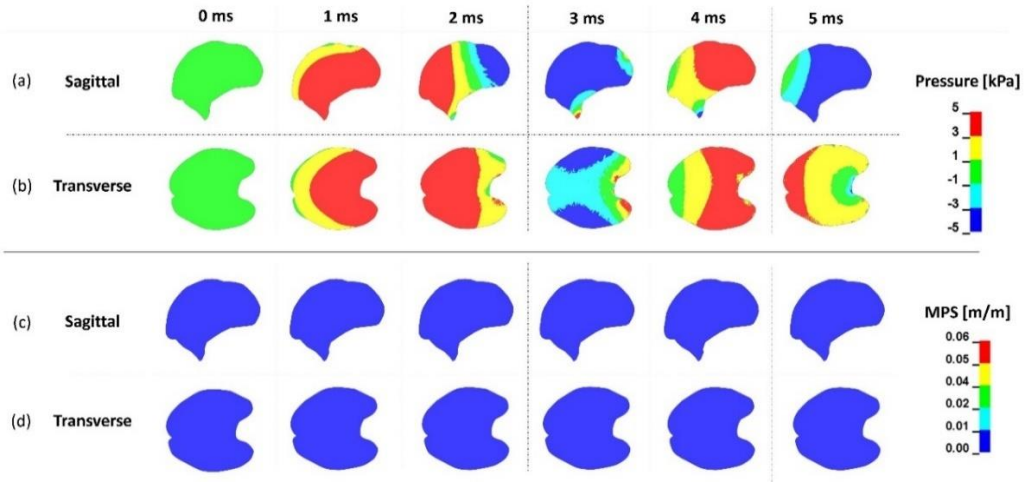


Figure 45: Distribution produced by the overpressure loads on the brain model along the time using a 50 ms increment. The brain response was measured not only by ICP in sagittal (a) and transverse (b) methods but also by MPS in sagittal (c) and transverse (d) methods

## 6.3. Brain response to combined overpressure and kinematic loading, assessed using FE head models

The head models were subjected to combined boundary conditions, resulting in an overpressure load extended by 5 ms, followed by a 7.40 ms delay after the initial overpressure, and concluding with the kinematic load. Although differences were observed between these head models with combined loads and the model with head kinematics loaded, it is noteworthy that the combined load and overpressure-loaded models exhibited identical behavior.

The first appreciable difference between the combined model and the kinematic model was the acceleration peaks produced by the overpressure load in the combined model (Figure 46). These acceleration peaks were notably greater than those produced by kinematics, especially the x-axis that exhibited linear acceleration peaks four times higher than those associated with kinematics. In contrast, rotational velocity showed no variation between the kinematic and combined models.

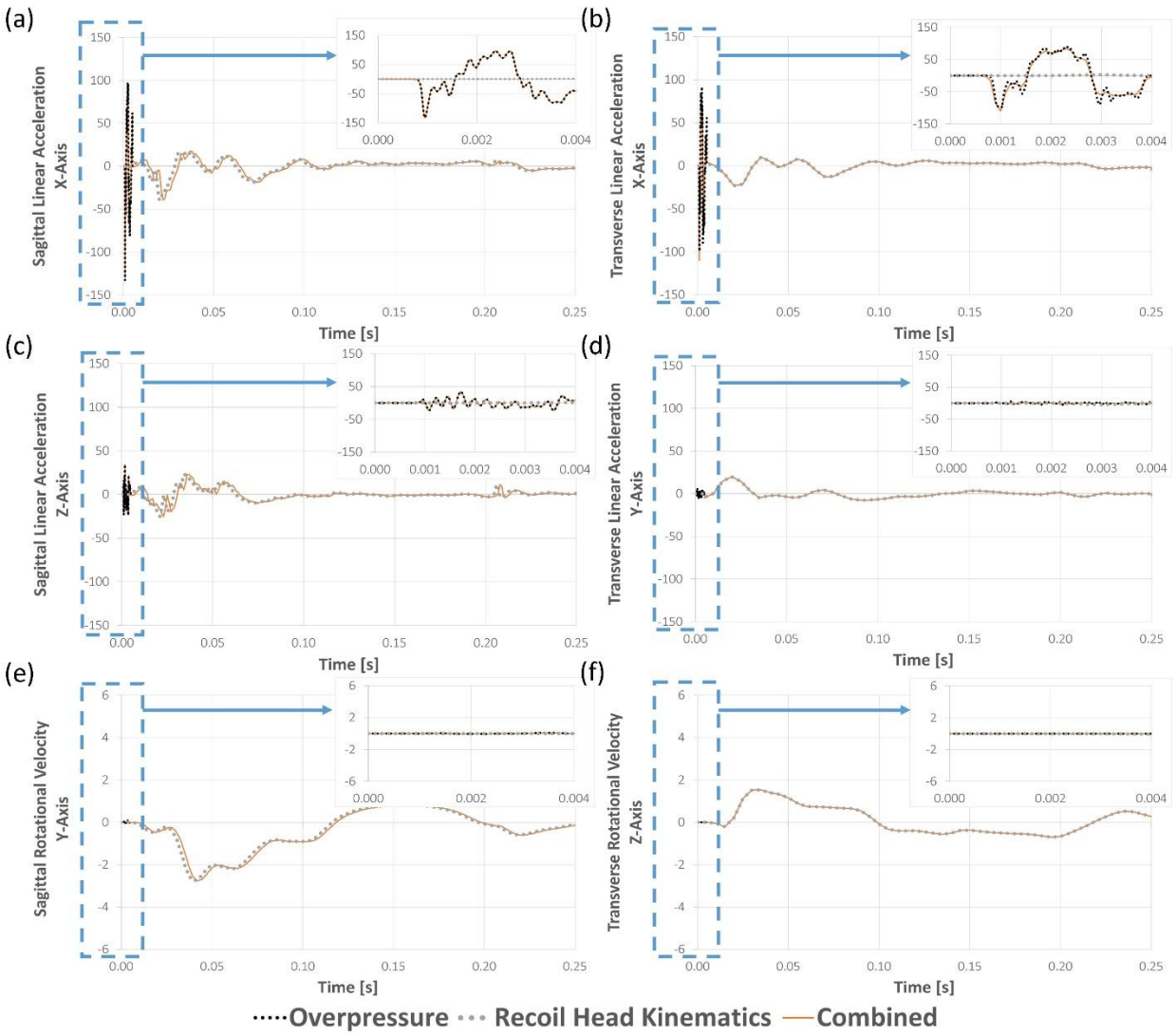


Figure 46: Comparison of kinematics between FE models with overpressure, kinematics and combined loads. Linear acceleration on the x-axis in the sagittal model (a), linear acceleration on the x-axis in the transverse model (b), linear acceleration on the z-axis in sagittal model (c), linear acceleration on the y-axis in the transverse model (d), rotational velocity on the y-axis in the sagittal model (e), and rotational velocity on the z-axis in the transverse model (f).

The HIC-15 (Table 11) was computed for the overpressure, head kinematic, and combined load models, showing a difference between the measurements (CV=23.615-36.212%). The results indicated that the linear acceleration peaks induced by the overpressure contributed to an increase (81-157%) in the HIC-15 value. Nevertheless, it is noteworthy that these HIC-15 values remained below the threshold of 700, associated with a 31% risk of head damage (Schmitt et al., 2019a). This finding suggested that the HIC-15 metric did not capture the injury risk posed by an LPR discharge.

Table 11: HIC-15 calculated in the head models for the three boundary conditions.

| Boundary Condition | HIC-15 | |
|---|---|---|
| | Sagittal | Transverse |
| **Kinematic** | 0.168 | 0.201 |
| **Overpressure** | 0.433 | 0.334 |
| **Combined** | 0.433 | 0.364 |
| **Mean** | 0.345 | 0.300 |
| **Standard Deviation (SD)** | 0.125 | 0.071 |
| **Coefficient of Variation (CV) [%]** | 36.212 | 23.615 |

Moreover, the temporal analysis of brain response in the combined load models revealed a dependency of $MPS_{95}$ on head kinematics, while ICP was influenced by both overpressure and head kinematic loads (Figure 47). The $MPS_{95}$ attributed to the overpressure load was negligible in comparison to the 4.06% of $MPS_{95}$ attributed to the kinematic load, suggesting a dependence of $MPS_{95}$ on head kinematics. Conversely, peaks in ICP were observed during both the overpressure (18.86 kPa) and kinematic phases (16.09 kPa), with the highest dependence on overpressure. However, the kinematics generated the most significant ICP peaks in the combined load models, indicating an interaction between both loads contributing to the overall ICP impact on the brain, even in the absence of temporal overlap.

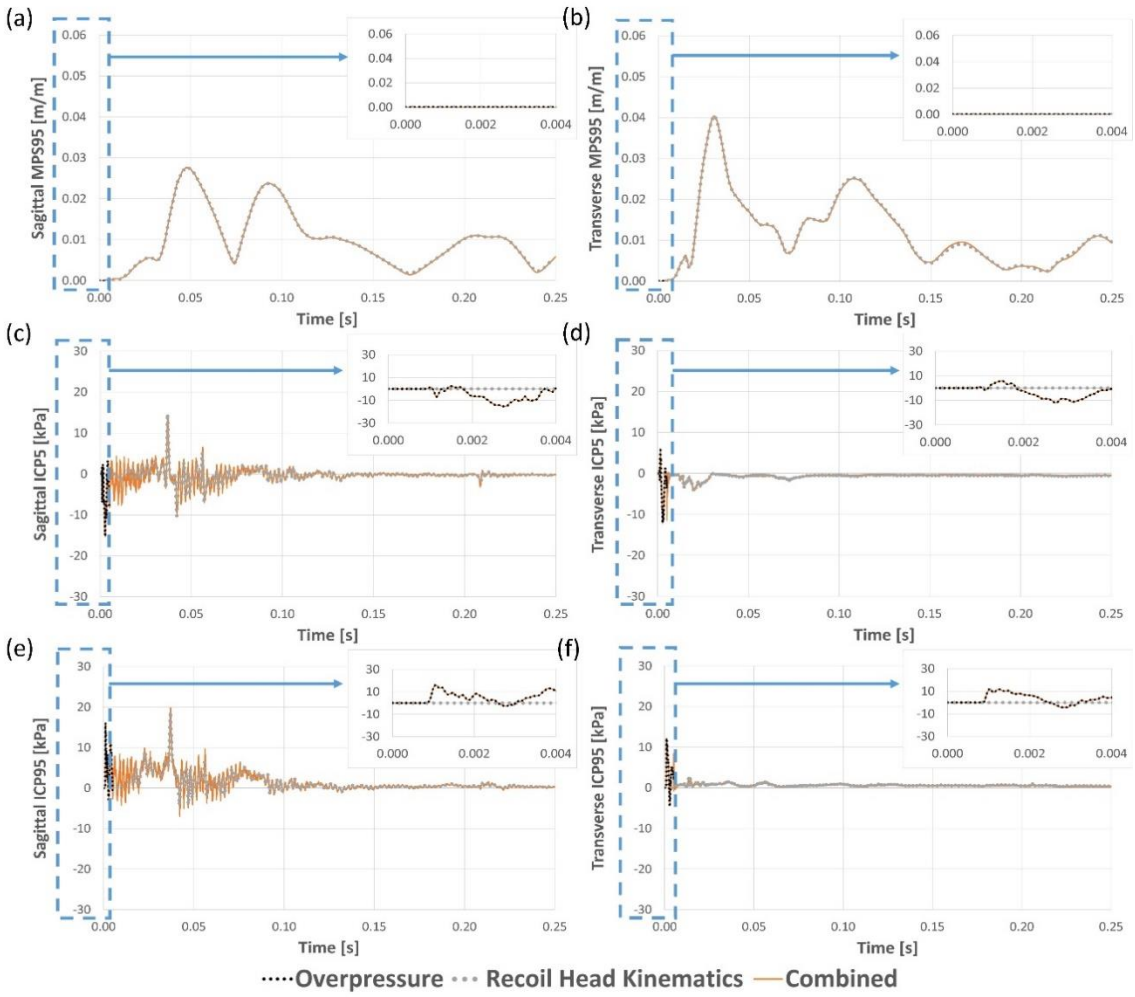


Figure 47: Comparison of MPS and ICP between FE models with kinematic, overpressure and combined loads, using $MPS_{95}$ in sagittal model (a), $MPS_{95}$ in transverse model (b), $ICP_5$ in sagittal model (c), $ICP_5$ in transverse model (d), $ICP_{95}$ in sagittal model (e), $ICP_{95}$ in transverse model (f).

The cumulative brain response reinforced the findings from the temporal analysis of brain response, highlighting both MPS dependency on head kinematics and the interaction of combined loads in ICP (Figure 48). Regarding MPS, the cumulative volume fraction response in the combined load models was similar to the head kinematics model (Figure 48a, b). Conversely, the cumulative volume fraction response to positive ICP in the combined load models exhibited an intermediate behavior, falling between the responses of the head kinematics and overpressure models (Figure 48e, f). the cumulative volume fraction response to negative ICP surpassed that of both the head kinematics and overpressure models, suggesting an interaction of both loads (Figure 48d).

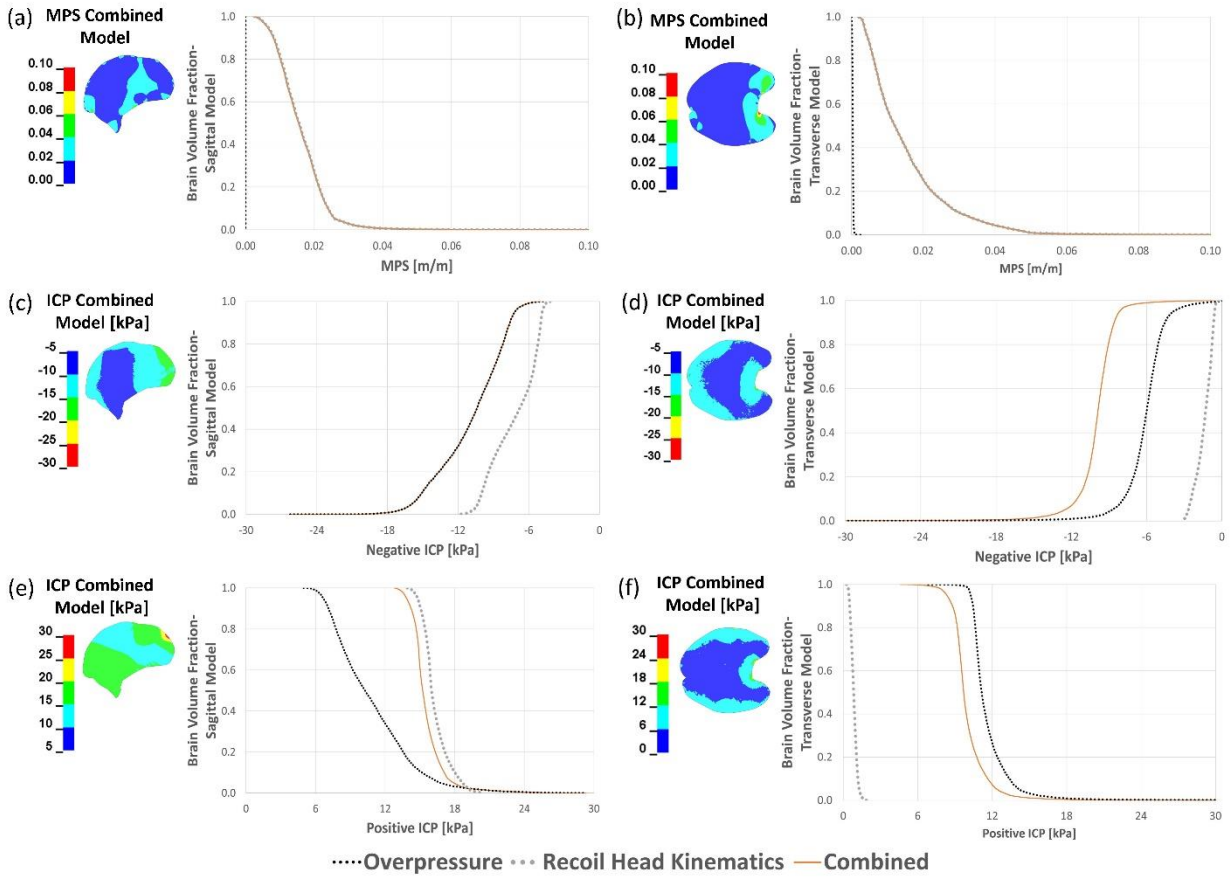


Figure 48: Cumulative brain volume response to MPS and ICP between FE models with kinematic, overpressure and combined loads, using MPS in sagittal model (a), MPS in transverse model (b), negative ICP in sagittal model (c), negative ICP in transverse model (d), positive ICP in sagittal model (e), positive ICP in transverse model (f).

The peak values of MPS and positive ICP were used to calculate the probability of concussion (Lyu et al., 2022) (Table 12), showing low possibility of injury risk (7%) for the sagittal and transverse models. Notably, the kinematic loads produced higher risk by MPS, and the overpressure loads produced higher peaks by ICP.

Table 12: Probability of concussion in sagittal and transverse models based on peaks of MPS and ICP

| Boundary Conditions | Sagittal | | Transverse | |
|---|---|---|---|---|
| | Risk by MPS (%) | Risk by ICP (%) | Risk by MPS (%) | Risk by ICP (%) |
| **Kinematics** | 3.120 | 3.330 | 3.460 | 2.160 |
| **Overpressure** | 1.480 | 3.930 | 1.480 | 7.110 |
| **Combined** | 3.120 | 3.930 | 3.440 | 4.860 |
| **Mean** | 2.573 | 3.730 | 2.793 | 4.710 |
| **Standard Deviation** | 0.773 | 0.283 | 0.929 | 2.024 |
| **Coefficient of Variation** | 30.043 | 7.583 | 33.247 | 42.964 |

It is important to note that the equations for the probability of concussions were developed to study a specific scenario of head accelerations and overpressure, which presented some variations in comparison to the boundary conditions applied in this study.

## 6.4. Sensitivity of the simulation to the delay variation

The HIC-15 values obtained in the transverse and sagittal models with delay variables (Table 13) suggested that the linear acceleration has no dependency on the delay time due to not significant difference (CV=0.008-0.071%). In addition, the HIC-15 values were below the threshold (700) for brain injury (Schmitt et al., 2019a).

Table 13: HIC-15 calculated in the head models for the five variations in delay time between kinematics and overpressure.

| Delay Time Between Boundary Conditions | HIC-15 | |
|---|---|---|
| | Sagittal | Transverse |
| **6.40 ms** | 0.433 | 0.364 |
| **10.65 ms** | 0.433 | 0.365 |
| **14.90 ms** | 0.433 | 0.365 |
| **19.15 ms** | 0.433 | 0.365 |
| **23.40 ms** | 0.433 | 0.365 |
| **Mean** | 0.433 | 0.365 |
| **Standard Deviation** | 0.000 | 0.000 |
| **Coefficient of Variation** | 0.008 | 0.071 |

While the peaks of MPS95 consistently exhibited no dependency on the delay between boundary conditions, the behavior of ICP was more intricate (Figure 49). In the transverse model, both $ICP_5$ and $ICP_{95}$ exhibited no variation in magnitudes with changes in delay time. In contrast, the $ICP_5$ and $ICP_{95}$ in the sagittal model displayed a difference in peaks (20%) due to the modifications in delay time, indicating an interaction between combined loads and the delay time between them.

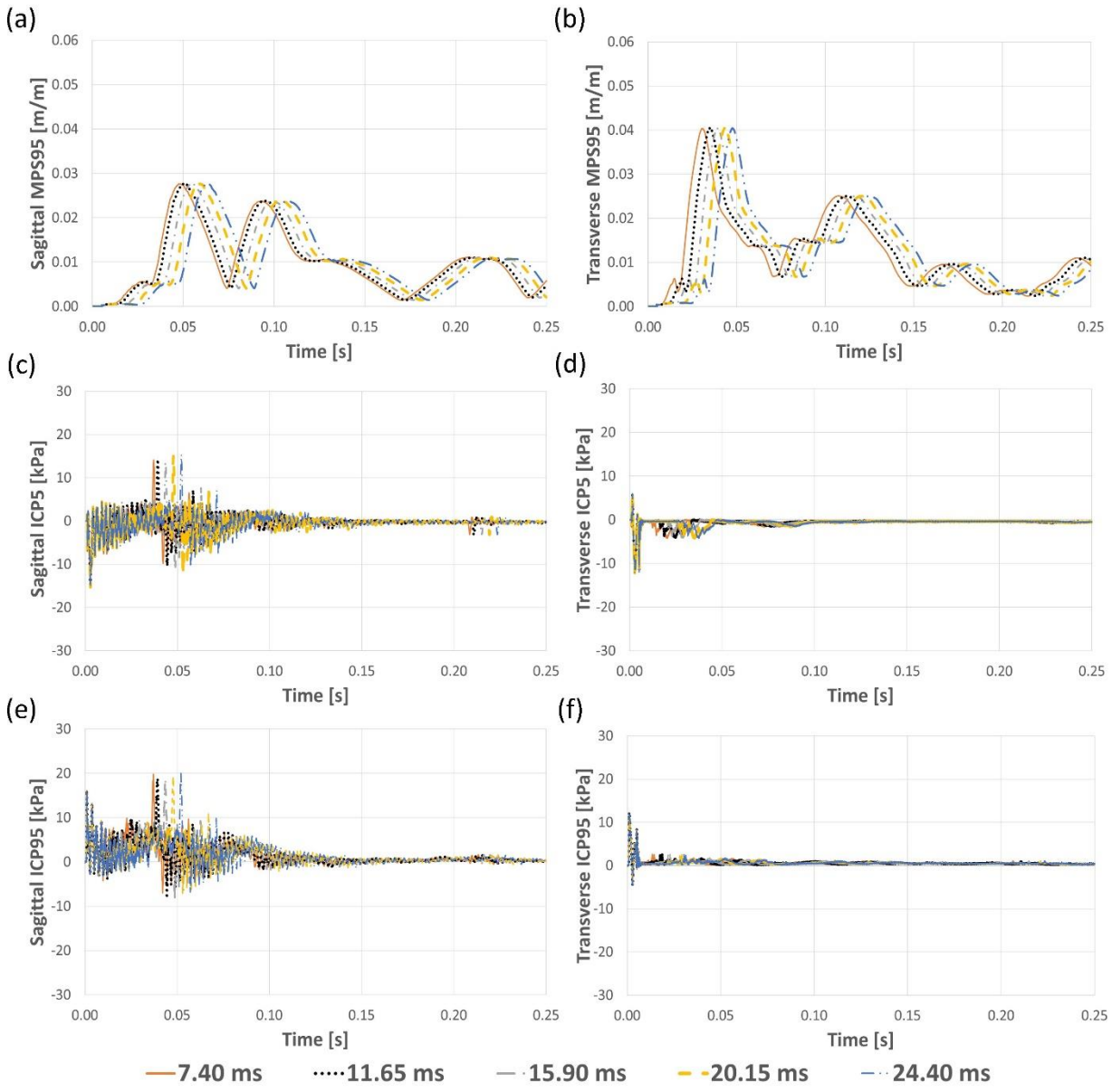


Figure 49: MPS and ICP calculated from the combined load of overpressure and kinematics applying a variation in delay time between boundary conditions. The comparisson used the $MPS_{95}$ in sagittal model (a), $MPS_{95}$ in transverse model (b), $ICP_5$ in sagittal model (c), $ICP_5$ in transverse model (d), $ICP_{95}$ in sagittal model (e), $ICP_{95}$ in transverse model (f).

The cumulative brain volume affected by MPS and ICP confirmed the results obtained over time, supporting the deduction of interaction between boundary conditions and the delay time between boundary conditions (Figure 50). The cumulative fraction volume response to MPS was unaffected in both the sagittal and transverse models, and the ICP in the transverse model exhibited no variations when the delay time was modified. On the contrary, the cumulative fraction volume response to positive ICP in the sagittal model demonstrated dependency on the delay time.

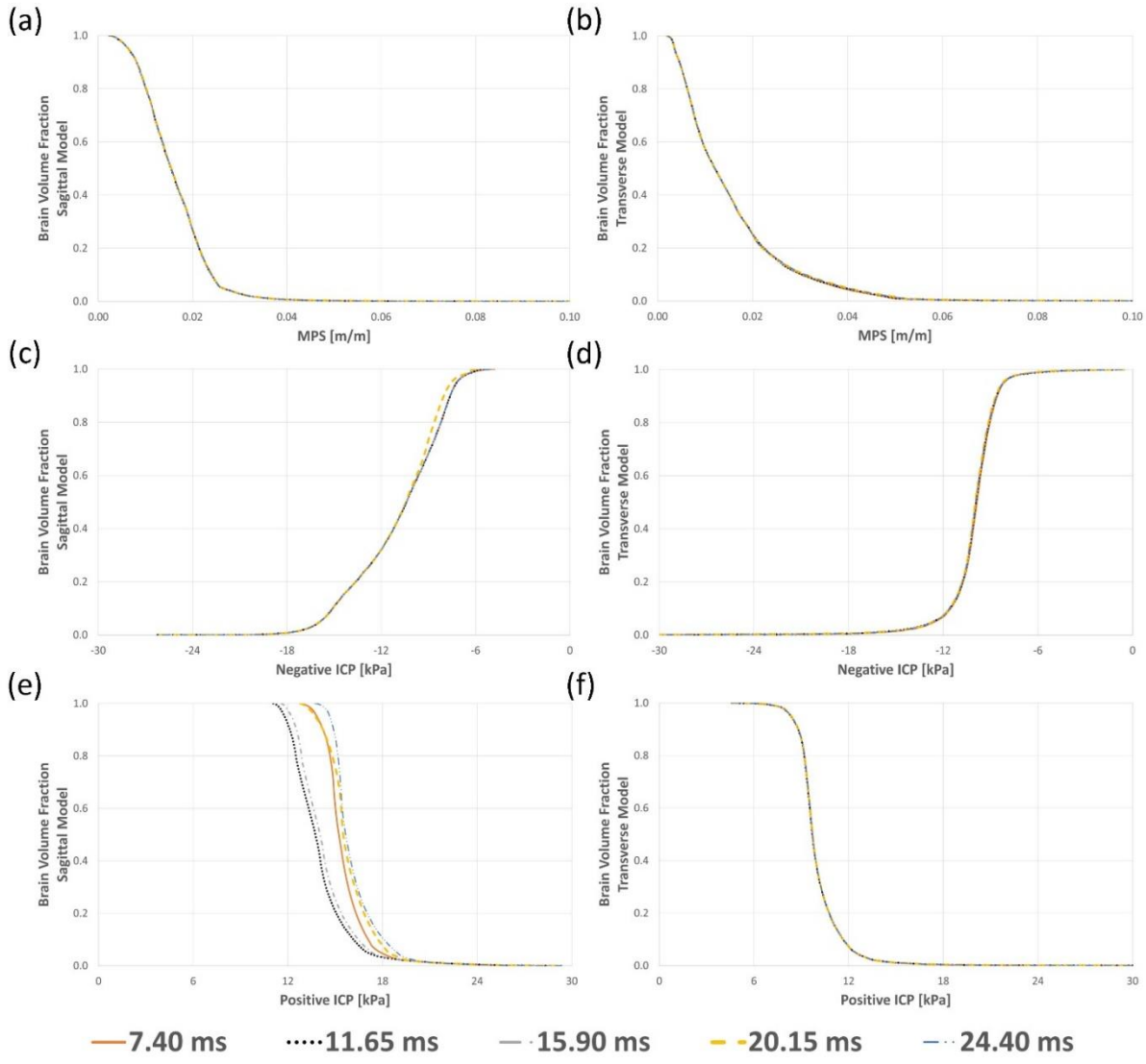


Figure 50: Cumulative volume brain response to the combined load of overpressure and kinematics applying a variation in delay time between boundary conditions. The comparison used the MPS in sagittal model (a), MPS in transverse model (b), negative ICP in sagittal model (c), negative ICP in transverse model (d), positive ICP in sagittal model (e), positive ICP in transverse model (f).

The positive ICP dependency on the delay time was visualized (Figure 51) using the area under the curve (AUC), showing a non-linear behavior. The AUC decreased (7%) from a delay time of 7.40 ms to 11.65 ms and increased (16%) until reached a top of 24.40 ms.

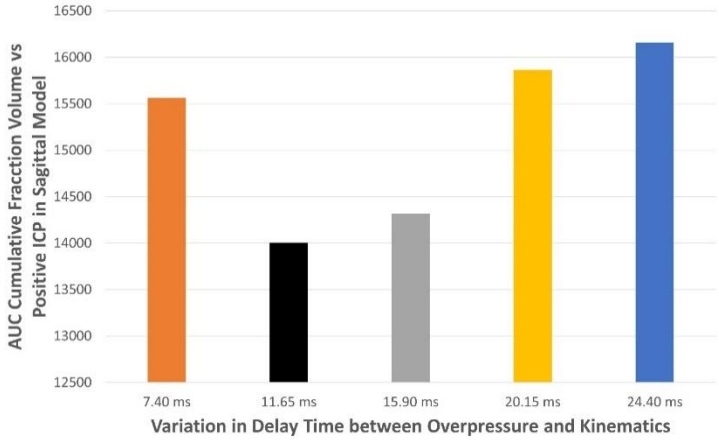


Figure 51: AUC cumulative fraction volume response to the positive ICP in the sagittal model

However, the estimation of concussion probability (Table 14) based on peaks of MPS and ICP showed no significant variation (CV= 0 - 1.468%), suggesting no dependency on the delay time between overpressure and kinematics.

Table 14: Probability of concussion in sagittal and transverse models based on peaks of MPS and ICP

| Delay Time Between Boundary Conditions | Sagittal | | Transverse | |
|---|---|---|---|---|
| | Risk by MPS (%) | Risk by ICP (%) | Risk by MPS (%) | Risk by ICP (%) |
| **7.40 ms** | 3.120 | 3.930 | 3.440 | 4.860 |
| **11.65 ms** | 3.120 | 3.930 | 3.530 | 4.810 |
| **15.90 ms** | 3.120 | 3.930 | 3.580 | 4.760 |
| **20.15 ms** | 3.130 | 3.930 | 3.570 | 4.930 |
| **24.4 ms** | 3.130 | 3.930 | 3.520 | 4.950 |
| **Mean** | 3.124 | 3.930 | 3.528 | 4.862 |
| **Standard Deviation** | 0.005 | 0.000 | 0.050 | 0.071 |
| **Coefficient of Variation** | 0.157 | 0.000 | 1.405 | 1.468 |

## 6.5. The brain response to suppressor effect in the head model

The results from initial discharges of the LPR with both the suppressor (KSO1D1 and OSH1D1) and non-suppressor (KSO1N1 and ONH1D1) configurations consistently revealed brain response patterns (Figure 52). The suppressor configurations incremented the $MPS_{95}$ peaks in both sagittal (148%) and transverse (50%) models compared to the non-suppressor counterpart. On the contrary, the non-suppressor configuration not only resulted in higher positive (62%) and negative peaks (77%) of ICP but also extended the duration of overpressure oscillations.

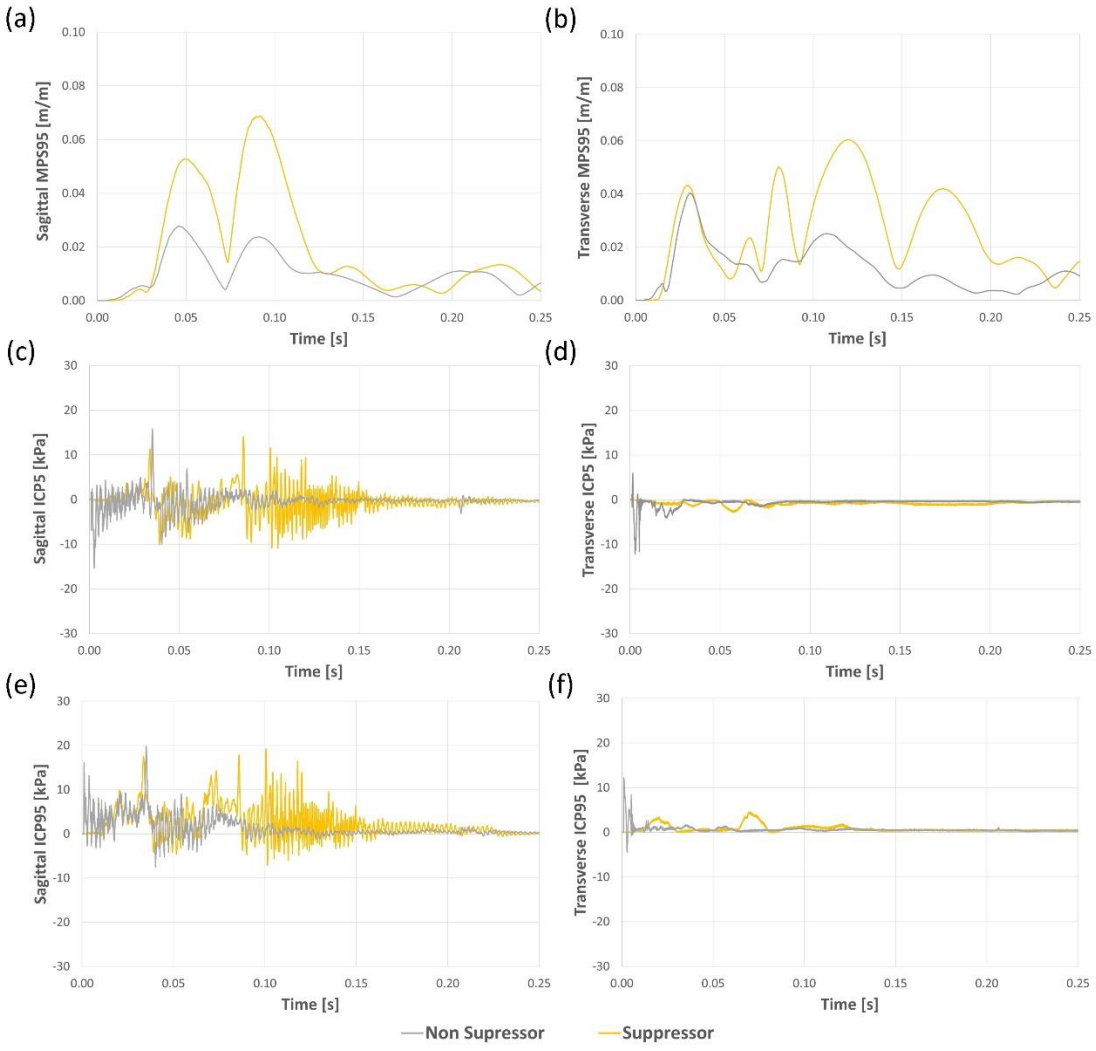


Figure 52: First discharge. Comparison in brain response variation depending on the suppressor or non-suppressor configuration using data from the first operator. The comparison used the $MPS_{95}$ in sagittal model (a), $MPS_{95}$ in transverse model (b), $ICP_5$ in sagittal model (c), $ICP_5$ in transverse model (d), $ICP_{95}$ in sagittal model (e), $ICP_{95}$ in transverse model (f).

In contrast, the results of the second discharges showed variability in the $MPS_{95}$ response to the suppressor (KSO1D2 and OSH1D1) and non-suppressor configurations (KSO1D2 and ONH1D1). While the $MPS_{95}$ in the transverse model presented no significant difference (0.9%) between the suppressor and the non-suppressor configuration (Figure 53a), the $MPS_{95}$ in the sagittal model presented higher peaks than the suppressor configuration (4.5%) (Figure 53b). On the other hand, the ICP kept the trend observed in the initial discharges of the LPR (Figure 53c-f) with higher positive (6.9%) and negative (8.3%) peaks of ICP and extended the duration of overpressure oscillations.

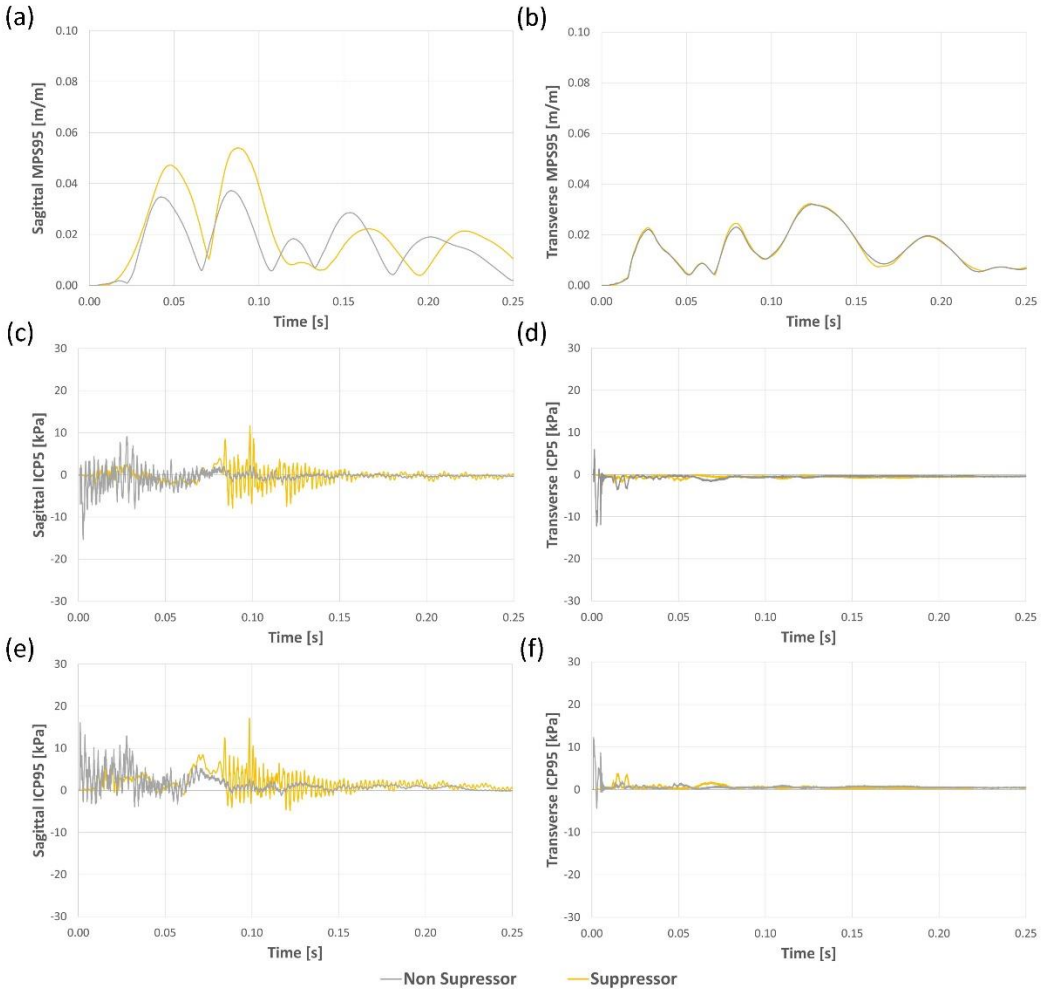


Figure 53: Second discharge. Comparison in brain response variation depending on the suppressor or non-suppressor configuration using data from the second operator. The comparison used the $MPS_{95}$ in sagittal model (a), $MPS_{95}$ in transverse model (b), $ICP_5$ in sagittal model (c), $ICP_5$ in transverse model (d), $ICP_{95}$ in sagittal model (e), $ICP_{95}$ in transverse model (f).

The cumulative brain volume curves for the first discharge was consistent with the metrics along the time results (Figure 54), the suppressor configuration (KSO1D2 and OSH1D1) decreased the entire cumulative brain volume response to the ICP but increased the area affected by the MPS.

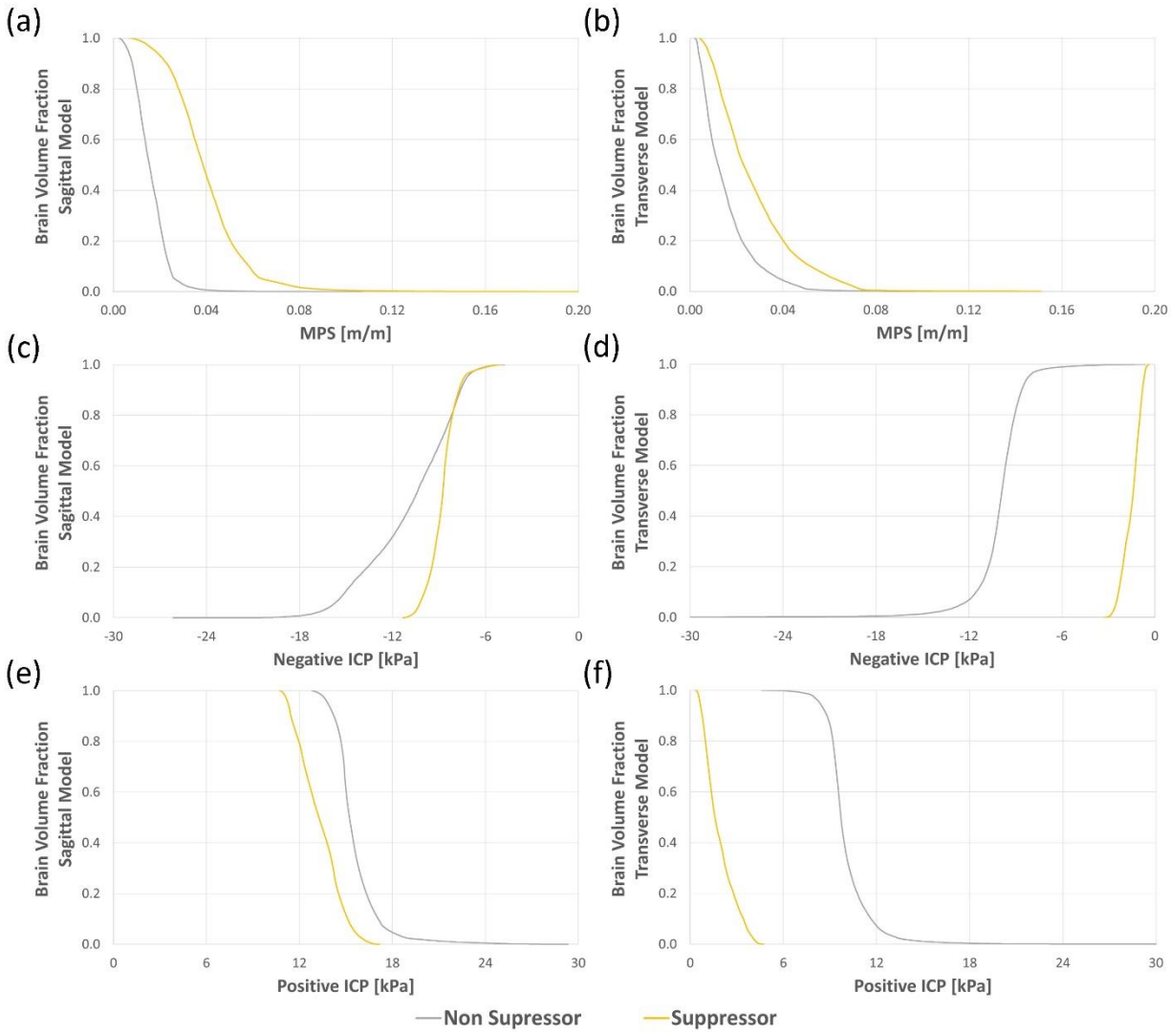


Figure 54: First discharge. Comparison in cumulative brain volume response variation depending on the suppressor or non-suppressor configuration. The brain response was measured using MPS in sagittal model (a), MPS in transverse model (b), negative ICP in sagittal model (c), negative ICP in transverse model (d), positive ICP in sagittal model (e), positive ICP in transverse model (f).

The second discharge presented agreement with the previous results (Figure 55), the suppressor configuration (KSO1D2 and OSH1D1) decreased the entire cumulative brain volume response to the ICP but increased the area affected by the MPS.

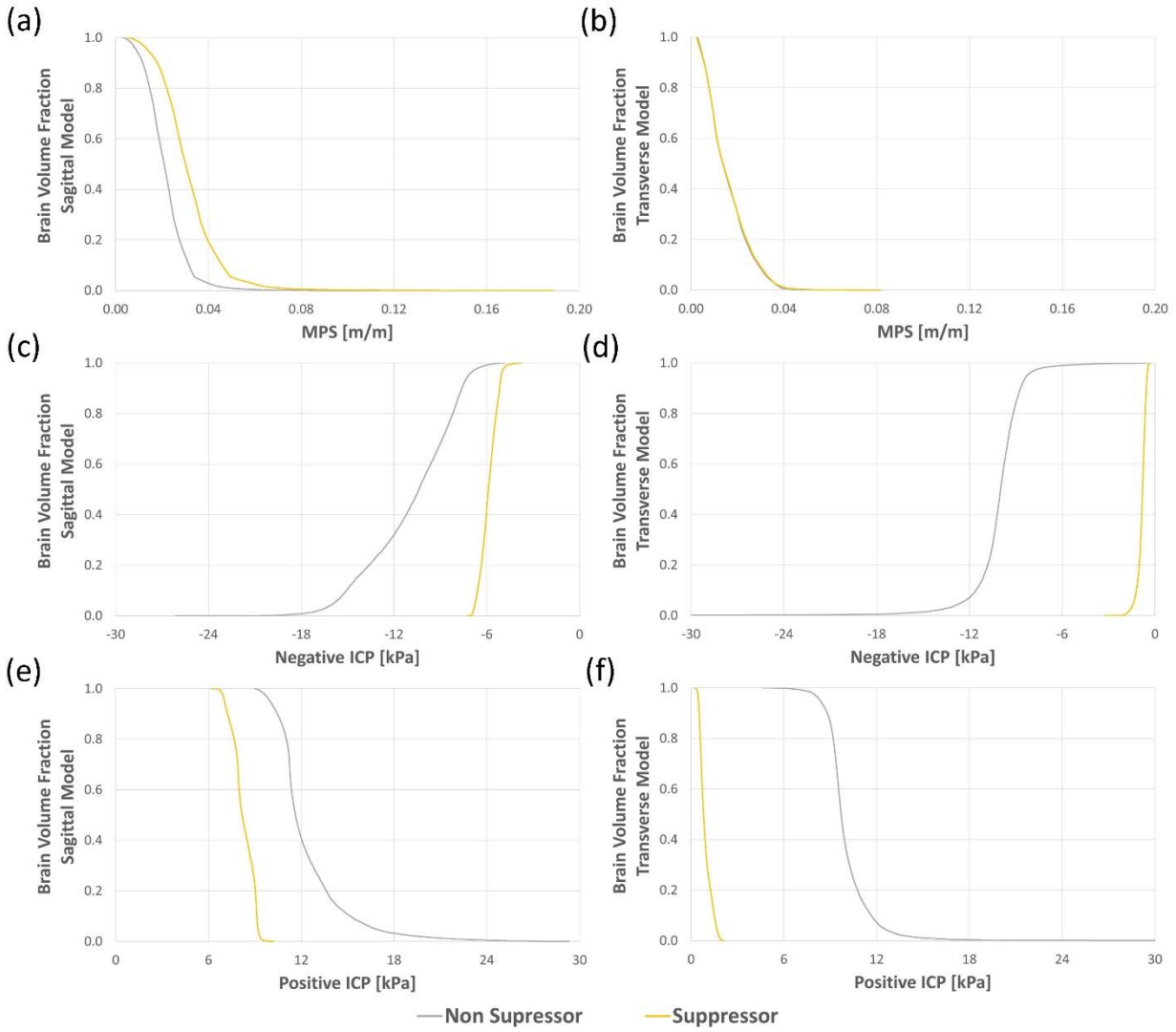


Figure 55: Second discharge. Comparison in cumulative brain volume response variation depending on the suppressor or non-suppressor configuration. The brain response was measured using MPS in sagittal model (a), MPS in transverse model (b), negative ICP in sagittal model (c), negative ICP in transverse model (d), positive ICP in sagittal model (e), positive ICP in transverse model (f).

The distribution of ICP and MPS in both sagittal and transverse models aligned with the numerical findings, indicating that the suppressor reduced the ICP effect and augmented the MPS effect (Figure 56). It is noteworthy that the suppressor configuration increased mean values of HIC-15

by 50 to 130% (Table 15). However, these values of HIC-15 remained below the established thresholds for brain injury (700).

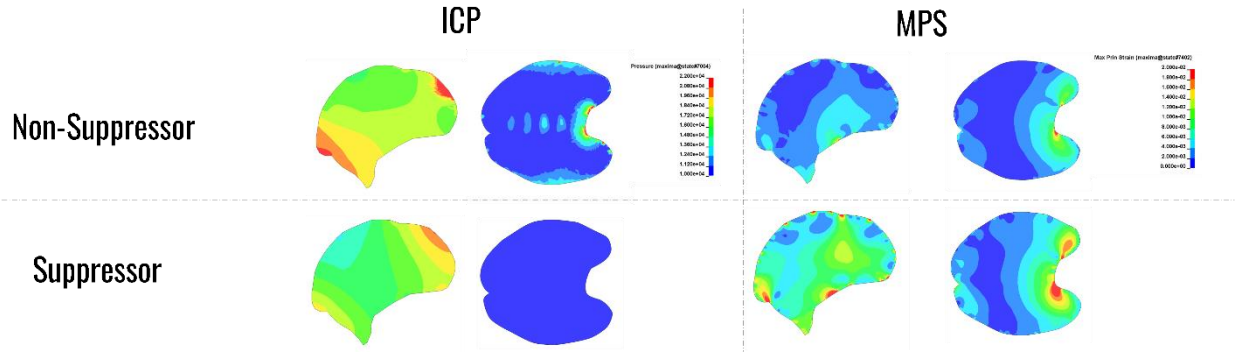


Figure 56: Comparison in brain response distribution in the head model for suppressor and non-suppressor configuration using the data from the first operator.

Table 15: HIC-15 calculated in the head models for the four LPR configurations.

| LPR Configuration | HIC-15 | |
|---|---|---|
| | Sagittal | Transverse |
| **Suppressor 1** | 0.996 | 0.457 |
| **Suppressor 2** | 0.920 | 0.433 |
| **Suppressor Mean** | 0.958 | 0.445 |
| **Non-Suppressor 1** | 0.433 | 0.364 |
| **Non-Suppressor 2** | 0.433 | 0.364 |
| **Non-Suppressor Mean** | 0.433 | 0.364 |

Finally, the probability of concussion based on peaks of MPS and ICP showed that the suppressor reduced the mean risk by ICP in 69.4 to 70.0 % but increased the mean risk by MPS in 36.3 to 69.1 %. Notice that the probability of concussion caused by a single discharge was low, but this can be cumulated with repetitive discharges during training sessions.

Table 16: Probability of concussion in sagittal and transverse models based on peaks of MPS and ICP

| LPR Configuration | Sagittal | | Transverse | |
|---|---|---|---|---|
| | Risk by MPS (%) | Risk by ICP (%) | Risk by MPS (%) | Risk by ICP (%) |
| **Suppressor 1** | 7.180 | 3.070 | 4.530 | 2.300 |
| **Suppressor 2** | 2.890 | 2.160 | 5.720 | 2.610 |
| **Suppressor Mean** | 5.035 | 2.615 | 5.125 | 2.455 |
| **Non-Suppressor 1** | 3.120 | 3.930 | 3.440 | 4.860 |
| **Non-Suppressor 2** | 2.840 | 4.930 | 4.080 | 3.930 |
| **Non-Suppressor Mean** | 2.980 | 4.430 | 3.760 | 4.395 |

# 7. Discussion

This section explores the implications of the estimated brain response to the kinematic and overpressure loads generated by the discharge of an LPR. The results discussed here were obtained by the combination of experimental data and planar FE models, representing the transverse and sagittal sections of the head through these FE models. Furthermore, this study examined the brain response in terms of maximum principal strain (MPS) and intracranial pressure (ICP) when subjected to variations in the LPR configuration and the time delay between the kinematic and overpressure loads.

## 7.1. Experimental kinematics and overpressure

The experiments aimed to address two pivotal questions concerning the LPR discharge: first, determining the sequence of loads resulting from the discharge; second, understanding how variations in the operator and LPR configuration (suppressor and non-suppressor). To solve these questions, this study separated the overpressure and kinematic loads, examining the impact of the variables on each specific load.

In examining the kinematic load, the recorded linear accelerations and angular velocities displayed significant variability. Analysis of four operators discharging LPRs with suppressor configuration revealed operator-dependent kinematic behavior (Section 4.1, Figure 6 - 8), aligning with findings on head kinematics in rifle operators from previous studies (Seeburrun et al., 2023). This operator-specific dependency remained consistent even when comparing the kinematics of one operator discharging LPRs with both suppressor and non-suppressor configurations. Notably, while the suppressor configuration exhibited higher angular velocity compared to its non-suppressor counterpart (65 - 122 % variation in peaks), the linear acceleration did not exhibit a distinct trend (-17 - 58 % variation in peaks). These findings suggest that the operator influences the kinematic response more than the specific LPR configuration.

To analyze the overpressure, a Brain Injury Protection Evaluation Device (BIPED) was utilized to simulate the head of the operator and measure the overpressure generated by both suppressor and non-suppressor configurations of the LPR. The results revealed notable mitigation of overpressure by the suppressor (Section 4.2, Figure 10), aligning with earlier research on suppressor design for

LPRs (Béres & Kovács, 2022; Keith Hudson et al., 1996). Furthermore, consistent overpressure levels were observed across multiple discharges in the non-suppressor configuration (cross-correlation score of 0.963), indicating a consistent association between overpressure and the specific LPR configuration.

An additional significant finding from the preceding results involves the observed time delay between kinematic and overpressure loads induced by LPR discharge. The experiments revealed a sequence of loads: initiating with a kinematic load, followed by a variable delay period (ranging from 7.40 to 24.40 ms, contingent upon the operator), culminating in an overpressure load. Notably, prior researchers (M. R. Miller et al., 2022; Ouellet & St-Onge, 2021; Sherif Said et al., 2018; Skotak et al., 2019) have focused on these loads in isolation, overlooking the sequence and delay observed in this study. Therefore, understanding and estimating this delay is essential in understanding the cumulative impact of both overpressure and kinematic loads on operators.

It is important to note that these findings call for careful interpretation due to limitations in data acquisition, particularly in the sample size concerning overpressure and head kinematics. In the case of the overpressure, the results revealed consistent measurements across four samples, demonstrating no statistically significant differences in the overpressure induced by an LPR. Additionally, the analysis of head kinematic data exposed significant variability among operators, providing valuable insights into the brain response to an LPR discharge but necessitating cautious interpretation.

## 7.2. Brain response to kinematics and overpressure loads

The transverse and sagittal FE models simulated the effects of an LPR discharge on kinematics and overpressure loads. These models demonstrated that while both loads generated ICPs in the brain, only the kinematic load resulted in meaningful MPS. To study these brain effects, element history (metrics over time) and cumulative fraction volume response were employed.

In the case of the kinematic load, the metrics tracked over time revealed an $MPS_{95}$ of 0.04 and ICPs of -12.43 kPa negative and 18.86 kPa positive. However, both $MPS_{95}$ and ICP fall below the injury thresholds, which are 0.20, -70 kPa, and 50 kPa for $MPS_{95}$, negative ICP, and positive ICP, respectively. This finding aligns with a prior study (Zhang et al., 2004), which concluded that it

requires high kinematics to overpass injury risk thresholds. Specifically, Zhang et al. showed that linear accelerations of 17000 $m/s^2$ and rotational velocities of 54 rad/s resulted in $MPS_{95}$ and ICP within the range of 0.20 and 172 kPa, respectively. It is important to note that despite the lower likelihood of injury based on these values, repeated exposure and interaction with overpressure could elevate the risk of injury.

Moreover, both the MPS and ICP exhibited a widespread distribution across the brain. An interesting observation was the localization of MPS in the anatomical region of the brain, contrasting with the location of ICP in the frontal area. This particular finding aligns with (Lyu et al., 2022), which highlighted a similar trend, attributing backward head movements and frontal overpressures to MPS in the medial area of the brain and ICPs in the frontal area, respectively.

In addition, the simulation results showed that the 19 kPa overpressure load had minimal impact on $MPS_{95}$ but significantly affected ICP, resulting in peak values of 16.09 kPa of positive and -15.32 kPa of negative ICP. This aligns with a previous study that simulated a higher range of overpressure between 170 and 326 kPa (Singh et al., 2014) to obtain 273 to 645 kPa of positive ICP and -211 to -760 kPa of negative ICP with an $MPS_{95}$ of 0.02 to 0.15. It is important to note that the increased ICP was concentrated in the frontal area, which is consistent with previous research (Lyu et al., 2022) and our prior study.

## 7.3. Brain response to combine loads

In the scenario of combined loading, the $MPS_{95}$, positive ICP, and negative ICP values did not surpass the peaks calculated from the overpressure and recoil head kinematics loadings individually (Section 6.4, Figure 29). Nevertheless, the cumulative fraction volume analysis revealed a distinct distribution pattern of positive and negative ICP across the brain. These findings suggest that although the combined effect of overpressure and kinematics loadings did not exhibit overlapping magnitudes, the interaction between these loads altered the volume of the brain affected by ICP.

A possible explanation for the interaction between kinematic and overpressure loads might be stress wave interference within the brain. Specifically, under the specified boundary conditions in a non-suppressor configuration with 7.40 ms of delay between loads (section 5.4), the negative

ICP in the transverse model showed increased cumulative fraction volume compared to individual analysis of overpressure and recoil head kinematics loadings (Section 6.4, Figure 34d), indicating constructive interference. Conversely, positive ICP responses suggested destructive interference, reducing the distribution of positive ICP in the combined-loading simulation (Section 6.4, Figure 34e - f).

While the planar nature of these models may be limited in predicting the behavior of the occipital region, their consistent results highlight the frontal area as the primary site for the interplay between overpressure and head kinematics. Prior studies (Panzer et al., 2012; Singh & Cronin, 2019) support utilizing planar models excluding the occipital regions to analyze frontal overpressure and backward movements, considering the typical localization of MPS and ICP in the medial region and frontal area. Thus, despite their limitations, these models still offer a viable means of studying ICP.

## 7.4. Brain response to variation in delay time between kinematics and overpressure

Manipulating the delay time between overpressure and kinematics revealed the occurrence of stress wave interference (Section 6.5, Figure 36). Specifically, the cumulative fraction brain volume curve demonstrated a non-linear variation in the distribution of positive ICP, which could either increase or decrease based on the delay time, showcasing a non-linear trend (Section 6.5, Figure 37). This observation suggests that wave interference can exhibit either destructive or constructive patterns, encompassing a range of 16% variability.

This study accords with an earlier study, which has consistently identified the coup area, essentially the frontal area, as the region with maximum ICP during simulations of backward head movement or frontal overpressure (Lyu et al., 2022). This consistency between studies suggests that the frontal area of the brain is an intriguing focal point for understanding the impact of combined head kinematics and overpressure.

It is important to note that while the $MPS_{95}$ and ICP resulting from the LPR discharge did not exceed proposed mTBI thresholds (20% MPS, 66-172 kPa positive ICP, and -76 kPa negative

ICP (Beckwith et al., 2018; Deck & Willinger, 2008; Gabler et al., 2016b; Huang et al., 2021; Zhang et al., 2004)), investigating their cumulative effects is crucial. Prior studies suggest that repeated accelerative and overpressure exposures can accumulate $MPS_{95}$ and ICP (Huang et al., 2021; Iverson et al., 2023; M. R. Miller et al., 2022; Woodall et al., 2023), hinting at a similar potential for repetitive LPR discharges.

## 7.5. Brain response to the use of a suppressor device

Despite the extended ICP oscillations and high variability in MPS behavior, the suppressor configuration notably decreased both ICP peaks and the cumulative volume fraction affected by ICP, subsequently lowering the concussion probability.

This study observed lower ICP peaks from the LPR with the suppressor configuration compared to the non-suppressor counterpart (Section 6.6, Figure 38c - d, and Figure 39 c - d). These findings signify a decreased likelihood of concussion in the order of 70%, implying the suppressor serves as an effective device in mitigating the adverse effects of LPR on the brain of the operator. Surprisingly, the ICP produced by the suppressor configuration exhibited more extended periods of oscillation (Section 6.6, Figure 38c - d, and Figure 39 c - d), indicating instability attributed to the suppressor. This finding reaffirms the influence of kinematic loads on ICP effects, which is consistent with previous findings from this study.

Both suppressor and non-suppressor configurations exposed significant variability in the MPS resulting from LPR discharges (Section 6.6, Figure 38a, b, and Figure 39a, b), indicating a weak link between the LPR configuration and the MPS effect. This concurs with studies emphasizing the crucial role of the operator in MPS (Seeburrun et al., 2023), suggesting the necessity for future research into particular operator variables influencing head kinematics.

In conclusion, this study advocates for the use of suppressor devices and encourages additional research into operator training as the optimal approach to mitigate the effects of ICP and MPS resulting from LPR discharges.

# 8. Conclusions

This section will outline the key conclusions drawn from the study. However, it is crucial to exercise caution in interpreting these findings due to the specific focus on planar finite elements (FE) models, specifically, sagittal and transverse models. These models were employed to estimate the brain response to kinematic forces and overpressure loads resulting from discharging a Long-LPR. Furthermore, the metrics used to analyze the brain response were centered on intracranial pressure (ICP) and maximum principal strain (MPS).

1. The recoil from the LPR discharge primarily correlates with the operator rather than the specific LPR configuration (suppressor or non-suppressor). Therefore, there was notable variability in head kinematics between operators, indicating a need for further research to understand this variability.
2. The overpressure magnitude demonstrated a dependence on the LPR configuration, resulting in consistent peak overpressures of 0.2 kPa and 27.6 kPa with the suppressor and non-suppressor configurations, respectively.
3. The evidence from this study suggests that there is a variable delay time between the kinematics and overpressure load, and this delay time depends on the operator.
4. This study revealed that the head kinematics resulted in MPS and ICP below literature thresholds proposed for brain injury. However, repetitive discharges during training sessions could potentially elevate the risk of injury.
5. The suppressor configuration effectively diminished the overpressure load generated by an LPR discharge, thereby lowering the risk of injury associated with ICP effects. Additionally, the overpressure did not induce substantial strains in the brain tissue, indicating that MPS is primarily dependent on the kinematic loading.
6. The combination of overpressure and kinematic loads resulted in a wave interference effect on ICP. Moreover, the findings regarding the sensitivity of the brain to the delay time between kinematic and overpressure load variations also indicated the occurrence of wave interference in ICP.

7. The study showed that using a suppressor reduces LPR discharge overpressure but might result in an increased MPS. Nevertheless, it is crucial to note that the variation in MPS was more dependent on the operator rather than the LPR configuration.

# 9. Recommendations

The recommendations for further work in this field of study are listed as follows.

1. This study raises inquiries about the operator-related factors influencing recoil head kinematics. While the experimental findings demonstrate a substantial operator-based influence on kinematics, further controlled trials are necessary to delineate the precise aspects of this dependency.
2. Given the limitation of the study to a single LPR discharge, the potential escalation of injury risk due to repetitive discharges, as noted in prior research, was acknowledged but remained unexplored due to constraints in available experimental data and simulation duration. Consequently, there is a strong recommendation for future investigations to center on understanding injury risk patterns concerning repetitive exposure to both kinematic and overpressure loads.
3. The planar nature of the FE model is appropriate for assessing overpressure propagation through the brain and identifying ICP focalization in the frontal area. Furthermore, incorporating aditional brain planes would enhance understanding of brain-behavior in response to the kinematics and overpressure loads
4. A further study could assess the long-term effects of the brain response to kinematics and overpressure load by contrasting the FE results with medical images and symptomatology over varying periods following LPR discharge sessions.

# Letter of Copyright Permission

## Figure 4 & 5 (Keith Hudson et al., 1996)

Marketplace

This is a License Agreement between Javier Andres Maldonado Echeverria ("User") and Copyright Clearance Center, Inc. ("CCC") on behalf of the Rightsholder identified in the order details below. The license consists of the order details, the Marketplace Permissions General Terms and Conditions below, and any Rightsholder Terms and Conditions which are included below.

All payments must be made in full to CCC in accordance with the Marketplace Permissions General Terms and Conditions below.

| | | | |
|---|---|---|---|
| Order Date | 21-Dec-2023 | Type of Use | Republish in a thesis/dissertation |
| Order License ID | 1430157-1 | | |
| System ID | 454881111 | Publisher | AIAA |
| | | Portion | Image/photo/illustration |

## LICENSED CONTENT

| | | | |
|---|---|---|---|
| Publication Title | 32nd Joint Propulsion Conference and Exhibit | Country | United States of America |
| | | Rightsholder | American Inst of Aeronautics & Astronautics (AIAA) |
| Date | 01/01/1996 | | |
| Language | English | Publication Type | Book |

## REQUEST DETAILS

| | | | |
|---|---|---|---|
| Portion Type | Image/photo/illustration | Distribution | Canada |
| Number of Images / Photos / Illustrations | 2 | Translation | Original language of publication |
| Format (select all that apply) | Print, Electronic | Copies for the Disabled? | No |
| | | Minor Editing Privileges? | No |
| Who Will Republish the Content? | Author of requested content | Incidental Promotional Use? | No |
| Duration of Use | Life of current edition | Currency | CAD |
| Lifetime Unit Quantity | Up to 499 | | |
| Rights Requested | Main product | | |

## NEW WORK DETAILS

| | | | |
|---|---|---|---|
| Title | Brain Response to Overpressure and Recoil Loads from Discharge of Long-Range Precision Rifle | Institution Name | University of Waterloo |
| | | Expected Presentation Date | 2024-01-30 |
| Instructor Name | Duane Cronin | | |

## ADDITIONAL DETAILS

| | | | |
|---|---|---|---|
| Order Reference Number | AIAA | The Requesting Person / Organization to Appear on the License | Javier Andres Maldonado Echeverria |

## REQUESTED CONTENT DETAILS

| | | | |
|---|---|---|---|
| Title, Description or Numeric Reference of the Portion(s) | https://doi.org/10.2514/6.1996-3020; Figure 5 | Title of the Article / Chapter the Portion Is From | CFD approach to firearms sound suppressor design |
| Editor of Portion(s) | AIAA | | |

| | | | |
|---|---|---|---|
| **Volume / Edition** | N/A | **Author of Portion(s)** | Hudson, Mitchell & Luchini, Chris & Clutter, Keith & Shyy, Wei. |
| **Page or Page Range of Portion** | AIAA paper 96-3020 | **Issue, if Republishing an Article From a Serial** | N/A |
| | | **Publication Date of Portion** | 1996-01-01 |

## RIGHTSHOLDER TERMS AND CONDITIONS

Verification of copyright ownership is your responsibility. You should only submit requests for materials that are owned by AIAA. Please review the copyright statement for the source material before submitting a reprint permission request, to ensure that AIAA is the copyright owner: For AIAA meeting papers, journal papers, or books with independently authored chapters (e.g., many Progress Series volumes), look at the bottom of the first full-text page (not the cover page). There will be a footnote indicating who holds copyright. For other books, look at the copyright statement on the back of the title page. If the statement reads "Copyright by the American Institute of Aeronautics and Astronautics, Inc.," then AIAA is the copyright owner, and you may submit your request. If the statement reads otherwise, AIAA does not hold copyright, and cannot grant permission to reprint. You must seek permission from the copyright owner rather than AIAA. Preferred credit line for reprinted material: From [original title and authors]; reprinted by permission of the American Institute of Aeronautics and Astronautics, Inc. Note that the original source also should be cited in full in the reference list.

## Marketplace Permissions General Terms and Conditions

The following terms and conditions ("General Terms"), together with any applicable Publisher Terms and Conditions, govern User's use of Works pursuant to the Licenses granted by Copyright Clearance Center, Inc. ("CCC") on behalf of the applicable Rightsholders of such Works through CCC's applicable Marketplace transactional licensing services (each, a "Service").

1) **Definitions.** For purposes of these General Terms, the following definitions apply:

"License" is the licensed use the User obtains via the Marketplace platform in a particular licensing transaction, as set forth in the Order Confirmation.

"Order Confirmation" is the confirmation CCC provides to the User at the conclusion of each Marketplace transaction. "Order Confirmation Terms" are additional terms set forth on specific Order Confirmations not set forth in the General Terms that can include terms applicable to a particular CCC transactional licensing service and/or any Rightsholder-specific terms.

"Rightsholder(s)" are the holders of copyright rights in the Works for which a User obtains licenses via the Marketplace platform, which are displayed on specific Order Confirmations.

"Terms" means the terms and conditions set forth in these General Terms and any additional Order Confirmation Terms collectively.

"User" or "you" is the person or entity making the use granted under the relevant License. Where the person accepting the Terms on behalf of a User is a freelancer or other third party who the User authorized to accept the General Terms on the User's behalf, such person shall be deemed jointly a User for purposes of such Terms.

"Work(s)" are the copyright protected works described in relevant Order Confirmations.

2) **Description of Service.** CCC's Marketplace enables Users to obtain Licenses to use one or more Works in accordance with all relevant Terms. CCC grants Licenses as an agent on behalf of the copyright rightsholder identified in the relevant Order Confirmation.

3) **Applicability of Terms.** The Terms govern User's use of Works in connection with the relevant License. In the event of any conflict between General Terms and Order Confirmation Terms, the latter shall govern. User acknowledges that Rightsholders have complete discretion whether to grant any permission, and whether to place any limitations on any grant, and that CCC has no right to supersede or to modify any such discretionary act by a Rightsholder.

4) **Representations; Acceptance.** By using the Service, User represents and warrants that User has been duly authorized by the User to accept, and hereby does accept, all Terms.

5) **Scope of License; Limitations and Obligations.** All Works and all rights therein, including copyright rights, remain the sole and exclusive property of the Rightsholder. The License provides only those rights expressly set forth in the terms and conveys no other rights in any Works

6) **General Payment Terms.** User may pay at time of checkout by credit card or choose to be invoiced. If the User chooses to be invoiced, the User shall: (i) remit payments in the manner identified on specific invoices, (ii) unless otherwise specifically stated in an Order Confirmation or separate written agreement, Users shall remit payments upon receipt of the relevant invoice from CCC, either

equity, but in no event to a payment of less than three times the Rightsholder's ordinary license price for the most closely analogous licensable use plus Rightsholder's and/or CCC's costs and expenses incurred in collecting such payment.

14) **Additional Terms for Specific Products and Services.** If a User is making one of the uses described in this Section 14, the additional terms and conditions apply:

a) ***Print Uses of Academic Course Content and Materials (photocopies for academic coursepacks or classroom handouts).*** For photocopies for academic coursepacks or classroom handouts the following additional terms apply:

i) The copies and anthologies created under this License may be made and assembled by faculty members individually or at their request by on-campus bookstores or copy centers, or by off-campus copy shops and other similar entities.

ii) No License granted shall in any way: (i) include any right by User to create a substantively non-identical copy of the Work or to edit or in any other way modify the Work (except by means of deleting material immediately preceding or following the entire portion of the Work copied) (ii) permit "publishing ventures" where any particular anthology would be systematically marketed at multiple institutions.

iii) Subject to any Publisher Terms (and notwithstanding any apparent contradiction in the Order Confirmation arising from data provided by User), any use authorized under the academic pay-per-use service is limited as follows:

A) any License granted shall apply to only one class (bearing a unique identifier as assigned by the institution, and thereby including all sections or other subparts of the class) at one institution;

B) use is limited to not more than 25% of the text of a book or of the items in a published collection of essays, poems or articles;

C) use is limited to no more than the greater of (a) 25% of the text of an issue of a journal or other periodical or (b) two articles from such an issue;

D) no User may sell or distribute any particular anthology, whether photocopied or electronic, at more than one institution of learning;

E) in the case of a photocopy permission, no materials may be entered into electronic memory by User except in order to produce an identical copy of a Work before or during the academic term (or analogous period) as to which any particular permission is granted. In the event that User shall choose to retain materials that are the subject of a photocopy permission in electronic memory for purposes of producing identical copies more than one day after such retention (but still within the scope of any permission granted), User must notify CCC of such fact in the applicable permission request and such retention shall constitute one copy actually sold for purposes of calculating permission fees due; and

F) any permission granted shall expire at the end of the class. No permission granted shall in any way include any right by User to create a substantively non-identical copy of the Work or to edit or in any other way modify the Work (except by means of deleting material immediately preceding or following the entire portion of the Work copied).

iv) Books and Records; Right to Audit. As to each permission granted under the academic pay-per-use Service, User shall maintain for at least four full calendar years books and records sufficient for CCC to determine the numbers of copies made by User under such permission. CCC and any representatives it may designate shall have the right to audit such books and records at any time during User's ordinary business hours, upon two days' prior notice. If any such audit shall determine that User shall have underpaid for, or underreported, any photocopies sold or by three percent (3%) or more, then User shall bear all the costs of any such audit; otherwise, CCC shall bear the costs of any such audit. Any amount determined by such audit to have been underpaid by User shall immediately be paid to CCC by User, together with interest thereon at the rate of 10% per annum from the date such amount was originally due. The provisions of this paragraph shall survive the termination of this License for any reason.

b) ***Digital Pay-Per-Uses of Academic Course Content and Materials (e-coursepacks, electronic reserves, learning management systems, academic institution intranets).*** For uses in e-coursepacks, posts in electronic reserves, posts in learning management systems, or posts on academic institution intranets, the following additional terms apply:

i) The pay-per-uses subject to this Section 14(b) include:

A) **Posting e-reserves, course management systems, e-coursepacks for text-based content,** which grants authorizations to import requested material in electronic format, and allows electronic access to this material to members of a designated college or university class, under the direction of an instructor designated by the college or university, accessible only under appropriate electronic controls (e.g., password);

B) **Posting e-reserves, course management systems, e-coursepacks for material consisting of photographs or other still images not embedded in text,** which grants not only the authorizations described in Section 14(b)(i)(A) above, but also the following authorization: to include the requested material in course materials for use consistent with Section

by delivery or notification of availability of the invoice via the Marketplace platform, and (iii) if the User does not pay the invoice within 30 days of receipt, the User may incur a service charge of 1.5% per month or the maximum rate allowed by applicable law, whichever is less. While User may exercise the rights in the License immediately upon receiving the Order Confirmation, the License is automatically revoked and is null and void, as if it had never been issued, if CCC does not receive complete payment on a timely basis.

7) **General Limits on Use.** Unless otherwise provided in the Order Confirmation, any grant of rights to User (i) involves only the rights set forth in the Terms and does not include subsequent or additional uses, (ii) is non-exclusive and non-transferable, and (iii) is subject to any and all limitations and restrictions (such as, but not limited to, limitations on duration of use or circulation) included in the Terms. Upon completion of the licensed use as set forth in the Order Confirmation, User shall either secure a new permission for further use of the Work(s) or immediately cease any new use of the Work(s) and shall render inaccessible (such as by deleting or by removing or severing links or other locators) any further copies of the Work. User may only make alterations to the Work if and as expressly set forth in the Order Confirmation. No Work may be used in any way that is unlawful, including without limitation if such use would violate applicable sanctions laws or regulations, would be defamatory, violate the rights of third parties (including such third parties' rights of copyright, privacy, publicity, or other tangible or intangible property), or is otherwise illegal, sexually explicit, or obscene. In addition, User may not conjoin a Work with any other material that may result in damage to the reputation of the Rightsholder. Any unlawful use will render any licenses hereunder null and void. User agrees to inform CCC if it becomes aware of any infringement of any rights in a Work and to cooperate with any reasonable request of CCC or the Rightsholder in connection therewith.

8) **Third Party Materials.** In the event that the material for which a License is sought includes third party materials (such as photographs, illustrations, graphs, inserts and similar materials) that are identified in such material as having been used by permission (or a similar indicator), User is responsible for identifying, and seeking separate licenses (under this Service, if available, or otherwise) for any of such third party materials; without a separate license, User may not use such third party materials via the License.

9) **Copyright Notice.** Use of proper copyright notice for a Work is required as a condition of any License granted under the Service. Unless otherwise provided in the Order Confirmation, a proper copyright notice will read substantially as follows: "Used with permission of [Rightsholder's name], from [Work's title, author, volume, edition number and year of copyright]; permission conveyed through Copyright Clearance Center, Inc." Such notice must be provided in a reasonably legible font size and must be placed either on a cover page or in another location that any person, upon gaining access to the material which is the subject of a permission, shall see, or in the case of republication Licenses, immediately adjacent to the Work as used (for example, as part of a by-line or footnote) or in the place where substantially all other credits or notices for the new work containing the republished Work are located. Failure to include the required notice results in loss to the Rightsholder and CCC, and the User shall be liable to pay liquidated damages for each such failure equal to twice the use fee specified in the Order Confirmation, in addition to the use fee itself and any other fees and charges specified.

10) **Indemnity.** User hereby indemnifies and agrees to defend the Rightsholder and CCC, and their respective employees and directors, against all claims, liability, damages, costs, and expenses, including legal fees and expenses, arising out of any use of a Work beyond the scope of the rights granted herein and in the Order Confirmation, or any use of a Work which has been altered in any unauthorized way by User, including claims of defamation or infringement of rights of copyright, publicity, privacy, or other tangible or intangible property.

11) **Limitation of Liability.** UNDER NO CIRCUMSTANCES WILL CCC OR THE RIGHTSHOLDER BE LIABLE FOR ANY DIRECT, INDIRECT, CONSEQUENTIAL, OR INCIDENTAL DAMAGES (INCLUDING WITHOUT LIMITATION DAMAGES FOR LOSS OF BUSINESS PROFITS OR INFORMATION, OR FOR BUSINESS INTERRUPTION) ARISING OUT OF THE USE OR INABILITY TO USE A WORK, EVEN IF ONE OR BOTH OF THEM HAS BEEN ADVISED OF THE POSSIBILITY OF SUCH DAMAGES. In any event, the total liability of the Rightsholder and CCC (including their respective employees and directors) shall not exceed the total amount actually paid by User for the relevant License. User assumes full liability for the actions and omissions of its principals, employees, agents, affiliates, successors, and assigns.

12) **Limited Warranties.** THE WORK(S) AND RIGHT(S) ARE PROVIDED "AS IS." CCC HAS THE RIGHT TO GRANT TO USER THE RIGHTS GRANTED IN THE ORDER CONFIRMATION DOCUMENT. CCC AND THE RIGHTSHOLDER DISCLAIM ALL OTHER WARRANTIES RELATING TO THE WORK(S) AND RIGHT(S), EITHER EXPRESS OR IMPLIED, INCLUDING WITHOUT LIMITATION IMPLIED WARRANTIES OF MERCHANTABILITY OR FITNESS FOR A PARTICULAR PURPOSE. ADDITIONAL RIGHTS MAY BE REQUIRED TO USE ILLUSTRATIONS, GRAPHS, PHOTOGRAPHS, ABSTRACTS, INSERTS, OR OTHER PORTIONS OF THE WORK (AS OPPOSED TO THE ENTIRE WORK) IN A MANNER CONTEMPLATED BY USER; USER UNDERSTANDS AND AGREES THAT NEITHER CCC NOR THE RIGHTSHOLDER MAY HAVE SUCH ADDITIONAL RIGHTS TO GRANT.

13) **Effect of Breach.** Any failure by User to pay any amount when due, or any use by User of a Work beyond the scope of the License set forth in the Order Confirmation and/or the Terms, shall be a material breach of such License. Any breach not cured within 10 days of written notice thereof shall result in immediate termination of such License without further notice. Any unauthorized (but licensable) use of a Work that is terminated immediately upon notice thereof may be liquidated by payment of the Rightsholder's ordinary license price therefor; any unauthorized (and unlicensable) use that is not terminated immediately for any reason (including, for example, because materials containing the Work cannot reasonably be recalled) will be subject to all remedies available at law or in

14(b)(i)(A) above, including any necessary resizing, reformatting or modification of the resolution of such requested material (provided that such modification does not alter the underlying editorial content or meaning of the requested material, and provided that the resulting modified content is used solely within the scope of, and in a manner consistent with, the particular authorization described in the Order Confirmation and the Terms), but not including any other form of manipulation, alteration or editing of the requested material;

C) **Posting e-reserves, course management systems, e-coursepacks or other academic distribution for audiovisual content,** which grants not only the authorizations described in Section 14(b)(i)(A) above, but also the following authorizations: (i) to include the requested material in course materials for use consistent with Section 14(b)(i)(A) above; (ii) to display and perform the requested material to such members of such class in the physical classroom or remotely by means of streaming media or other video formats; and (iii) to "clip" or reformat the requested material for purposes of time or content management or ease of delivery, provided that such "clipping" or reformatting does not alter the underlying editorial content or meaning of the requested material and that the resulting material is used solely within the scope of, and in a manner consistent with, the particular authorization described in the Order Confirmation and the Terms. Unless expressly set forth in the relevant Order Conformation, the License does not authorize any other form of manipulation, alteration or editing of the requested material.

ii) Unless expressly set forth in the relevant Order Confirmation, no License granted shall in any way: (i) include any right by User to create a substantively non-identical copy of the Work or to edit or in any other way modify the Work (except by means of deleting material immediately preceding or following the entire portion of the Work copied or, in the case of Works subject to Sections 14(b)(1)(B) or (C) above, as described in such Sections) (ii) permit "publishing ventures" where any particular course materials would be systematically marketed at multiple institutions.

iii) Subject to any further limitations determined in the Rightsholder Terms (and notwithstanding any apparent contradiction in the Order Confirmation arising from data provided by User), any use authorized under the electronic course content pay-per-use service is limited as follows:

A) any License granted shall apply to only one class (bearing a unique identifier as assigned by the institution, and thereby including all sections or other subparts of the class) at one institution;

B) use is limited to not more than 25% of the text of a book or of the items in a published collection of essays, poems or articles;

C) use is limited to not more than the greater of (a) 25% of the text of an issue of a journal or other periodical or (b) two articles from such an issue;

D) no User may sell or distribute any particular materials, whether photocopied or electronic, at more than one institution of learning;

E) electronic access to material which is the subject of an electronic-use permission must be limited by means of electronic password, student identification or other control permitting access solely to students and instructors in the class;

F) User must ensure (through use of an electronic cover page or other appropriate means) that any person, upon gaining electronic access to the material, which is the subject of a permission, shall see:

- a proper copyright notice, identifying the Rightsholder in whose name CCC has granted permission,
- a statement to the effect that such copy was made pursuant to permission,
- a statement identifying the class to which the material applies and notifying the reader that the material has been made available electronically solely for use in the class, and
- a statement to the effect that the material may not be further distributed to any person outside the class, whether by copying or by transmission and whether electronically or in paper form, and User must also ensure that such cover page or other means will print out in the event that the person accessing the material chooses to print out the material or any part thereof.

G) any permission granted shall expire at the end of the class and, absent some other form of authorization, User is thereupon required to delete the applicable material from any electronic storage or to block electronic access to the applicable material.

iv) Uses of separate portions of a Work, even if they are to be included in the same course material or the same university or college class, require separate permissions under the electronic course content pay-per-use Service. Unless otherwise provided in the Order Confirmation, any grant of rights to User is limited to use completed no later than the end of the academic term (or analogous period) as to which any particular permission is granted.

v) Books and Records; Right to Audit. As to each permission granted under the electronic course content Service, User shall maintain for at least four full calendar years books and records sufficient for CCC to determine the numbers of copies made by User under such permission. CCC and any representatives it may designate shall have the right to audit such books and records at any time during User's ordinary business hours, upon two days' prior notice. If any such audit shall determine that User shall have underpaid for, or underreported, any electronic copies used by three percent (3%) or more, then User shall bear all the costs of any such audit; otherwise, CCC shall bear the costs of any such audit. Any amount determined by such audit to have been underpaid by User shall immediately be paid to CCC by User, together with interest thereon at the rate of 10% per annum from the date such amount was originally due. The provisions of this paragraph shall survive the termination of this license for any reason.

c) ***Pay-Per-Use Permissions for Certain Reproductions (Academic photocopies for library reserves and interlibrary loan reporting) (Non-academic internal/external business uses and commercial document delivery).*** The License expressly excludes the uses listed in Section (c)(i)-(v) below (which must be subject to separate license from the applicable Rightsholder) for: academic photocopies for library reserves and interlibrary loan reporting; and non-academic internal/external business uses and commercial document delivery.

i) electronic storage of any reproduction (whether in plain-text, PDF, or any other format) other than on a transitory basis;

ii) the input of Works or reproductions thereof into any computerized database;

iii) reproduction of an entire Work (cover-to-cover copying) except where the Work is a single article;

iv) reproduction for resale to anyone other than a specific customer of User;

v) republication in any different form. Please obtain authorizations for these uses through other CCC services or directly from the rightsholder.

Any license granted is further limited as set forth in any restrictions included in the Order Confirmation and/or in these Terms.

d) ***Electronic Reproductions in Online Environments (Non-Academic-email, intranet, internet and extranet).*** For "electronic reproductions", which generally includes e-mail use (including instant messaging or other electronic transmission to a defined group of recipients) or posting on an intranet, extranet or Intranet site (including any display or performance incidental thereto), the following additional terms apply:

i) Unless otherwise set forth in the Order Confirmation, the License is limited to use completed within 30 days for any use on the Internet, 60 days for any use on an intranet or extranet and one year for any other use, all as measured from the "republication date" as identified in the Order Confirmation, if any, and otherwise from the date of the Order Confirmation.

ii) User may not make or permit any alterations to the Work, unless expressly set forth in the Order Confirmation (after request by User and approval by Rightsholder); provided, however, that a Work consisting of photographs or other still images not embedded in text may, if necessary, be resized, reformatted or have its resolution modified without additional express permission, and a Work consisting of audiovisual content may, if necessary, be "clipped" or reformatted for purposes of time or content management or ease of delivery (provided that any such resizing, reformatting, resolution modification or "clipping" does not alter the underlying editorial content or meaning of the Work used, and that the resulting material is used solely within the scope of, and in a manner consistent with, the particular License described in the Order Confirmation and the Terms.

15) **Miscellaneous.**

a) User acknowledges that CCC may, from time to time, make changes or additions to the Service or to the Terms, and that Rightsholder may make changes or additions to the Rightsholder Terms. Such updated Terms will replace the prior terms and conditions in the order workflow and shall be effective as to any subsequent Licenses but shall not apply to Licenses already granted and paid for under a prior set of terms.

b) Use of User-related information collected through the Service is governed by CCC's privacy policy, available online at www.copyright.com/about/privacy-policy/.

c) The License is personal to User. Therefore, User may not assign or transfer to any other person (whether a natural person or an organization of any kind) the License or any rights granted thereunder; provided, however, that, where applicable, User may assign such License in its entirety on written notice to CCC in the event of a transfer of all or substantially all of User's rights in any new material which includes the Work(s) licensed under this Service.

d) No amendment or waiver of any Terms is binding unless set forth in writing and signed by the appropriate parties, including, where applicable, the Rightsholder. The Rightsholder and CCC hereby object to any terms contained in any writing prepared by or on behalf of the User or its principals, employees, agents or affiliates and purporting to govern or otherwise relate to the License described in the Order Confirmation, which terms are in any way inconsistent with any Terms set forth in the Order Confirmation,

# Figure 6 (de Vos et al., 2023)

JOHN WILEY AND SONS LICENSE
TERMS AND CONDITIONS

Jan 04, 2024

---

This Agreement between Mr. Javier Maldonado-Echeverria ("You") and John Wiley and Sons ("John Wiley and Sons") consists of your license details and the terms and conditions provided by John Wiley and Sons and Copyright Clearance Center.

| | |
|---|---|
| License Number | 5693820605299 |
| License date | Dec 21, 2023 |
| Licensed Content Publisher | John Wiley and Sons |
| Licensed Content Publication | Magnetic Resonance in Medicine |
| Licensed Content Title | Characterization of concomitant gradient fields and their effects on image distortions using a low-field point-of-care Halbach-based MRI system |
| Licensed Content Author | Andrew G. Webb, Rob F. Remis, Bart Vos |
| Licensed Content Date | Sep 25, 2023 |
| Licensed Content Volume | 91 |
| Licensed Content Issue | 2 |
| Licensed Content Pages | 14 |
| Type of use | Dissertation/Thesis |

| | |
|---|---|
| Requestor type | University/Academic |
| Format | Print and electronic |
| Portion | Figure/table |
| Number of figures/tables | 1 |
| Will you be translating? | No |
| Title of new work | Brain Response to Overpressure and Recoil Loads from Discharge of Long-Range Precision Rifle |
| Institution name | University of Waterloo |
| Expected presentation date | Jan 2024 |
| Order reference number | Wiley2 |
| Portions | Figure 2: Two-dimensional brain phantoms corresponding to transverse, sagittal and coronal brain slabs. With relaxation parameters of the compartments approximately equal to in vivo data at 50 mT |
| Requestor Location | Mr. Javier Maldonado-Echeverria<br>350 Columbia Street West<br>Unit 313<br>Waterloo, ON N2L6P4<br>Canada<br>Attn: Mr. Javier Maldonado-Echeverria |
| Publisher Tax ID | EU826007151 |
| Total | 0.00 CAD |

Terms and Conditions

**TERMS AND CONDITIONS**

WILEY or its licensors is granted hereunder, and you agree that you shall not assert any such right, license or interest with respect thereto

- NEITHER WILEY NOR ITS LICENSORS MAKES ANY WARRANTY OR REPRESENTATION OF ANY KIND TO YOU OR ANY THIRD PARTY, EXPRESS, IMPLIED OR STATUTORY, WITH RESPECT TO THE MATERIALS OR THE ACCURACY OF ANY INFORMATION CONTAINED IN THE MATERIALS, INCLUDING, WITHOUT LIMITATION, ANY IMPLIED WARRANTY OF MERCHANTABILITY, ACCURACY, SATISFACTORY QUALITY, FITNESS FOR A PARTICULAR PURPOSE, USABILITY, INTEGRATION OR NON-INFRINGEMENT AND ALL SUCH WARRANTIES ARE HEREBY EXCLUDED BY WILEY AND ITS LICENSORS AND WAIVED BY YOU.

- WILEY shall have the right to terminate this Agreement immediately upon breach of this Agreement by you.

- You shall indemnify, defend and hold harmless WILEY, its Licensors and their respective directors, officers, agents and employees, from and against any actual or threatened claims, demands, causes of action or proceedings arising from any breach of this Agreement by you.

- IN NO EVENT SHALL WILEY OR ITS LICENSORS BE LIABLE TO YOU OR ANY OTHER PARTY OR ANY OTHER PERSON OR ENTITY FOR ANY SPECIAL, CONSEQUENTIAL, INCIDENTAL, INDIRECT, EXEMPLARY OR PUNITIVE DAMAGES, HOWEVER CAUSED, ARISING OUT OF OR IN CONNECTION WITH THE DOWNLOADING, PROVISIONING, VIEWING OR USE OF THE MATERIALS REGARDLESS OF THE FORM OF ACTION, WHETHER FOR BREACH OF CONTRACT, BREACH OF WARRANTY, TORT, NEGLIGENCE, INFRINGEMENT OR OTHERWISE (INCLUDING, WITHOUT LIMITATION, DAMAGES BASED ON LOSS OF PROFITS, DATA, FILES, USE, BUSINESS OPPORTUNITY OR CLAIMS OF THIRD PARTIES), AND WHETHER OR NOT THE PARTY HAS BEEN ADVISED OF THE POSSIBILITY OF SUCH DAMAGES. THIS LIMITATION SHALL APPLY NOTWITHSTANDING ANY FAILURE OF ESSENTIAL PURPOSE OF ANY LIMITED REMEDY PROVIDED HEREIN.

- Should any provision of this Agreement be held by a court of competent jurisdiction to be illegal, invalid, or unenforceable, that provision shall be deemed amended to achieve as nearly as possible the same economic effect as the original provision, and the legality, validity and enforceability of the remaining provisions of this Agreement shall not be affected or impaired thereby.

- The failure of either party to enforce any term or condition of this Agreement shall not constitute a waiver of either party's right to enforce each and every term and condition of this Agreement. No breach under this agreement shall be deemed waived or excused by either party unless such waiver or consent is in writing signed by the party granting such waiver or consent. The waiver by or consent of a party to a breach of any provision of this Agreement shall not operate or be construed as a waiver of or consent to any other or subsequent breach by such other party.

- This Agreement may not be assigned (including by operation of law or otherwise) by you without WILEY's prior written consent.

- Any fee required for this permission shall be non-refundable after thirty (30) days from receipt by the CCC.

- These terms and conditions together with CCC's Billing and Payment terms and conditions (which are incorporated herein) form the entire agreement between you and WILEY concerning this licensing transaction and (in the absence of fraud) supersedes all prior agreements and representations of the parties, oral or written. This Agreement may not be amended except in writing signed by both parties. This Agreement shall be binding upon and inure to the benefit of the parties' successors, legal representatives, and authorized assigns.

- In the event of any conflict between your obligations established by these terms and conditions and those established by CCC's Billing and Payment terms and conditions, these terms and conditions shall prevail.

- WILEY expressly reserves all rights not specifically granted in the combination of (i) the license details provided by you and accepted in the course of this licensing transaction, (ii) these terms and conditions and (iii) CCC's Billing and Payment terms and conditions.

- This Agreement will be void if the Type of Use, Format, Circulation, or Requestor Type was misrepresented during the licensing process.

- This Agreement shall be governed by and construed in accordance with the laws of the State of New York, USA, without regards to such state's conflict of law rules. Any legal action, suit or proceeding arising out of or relating to these Terms and Conditions or the breach thereof shall be instituted in a court of competent jurisdiction in New York County in the State of New York in the United States of America and each party hereby consents and submits to the personal jurisdiction of such court, waives any objection to venue in such court and consents to service of process by registered or certified mail, return receipt requested, at the last known address of such party.

**WILEY OPEN ACCESS TERMS AND CONDITIONS**

Wiley Publishes Open Access Articles in fully Open Access Journals and in Subscription journals offering Online Open. Although most of the fully Open Access journals publish open access articles under the terms of the Creative Commons Attribution (CC BY) License only, the subscription journals and a few of the Open Access Journals offer a choice of Creative Commons Licenses. The license type is clearly identified on the article.

**The Creative Commons Attribution License**

The Creative Commons Attribution License (CC-BY) allows users to copy, distribute and transmit an article, adapt the article and make commercial use of the article. The CC-BY license permits commercial and non-

**Creative Commons Attribution Non-Commercial License**

The Creative Commons Attribution Non-Commercial (CC-BY-NC)License permits use, distribution and reproduction in any medium, provided the original work is properly cited and is not used for commercial purposes.(see below)

**Creative Commons Attribution-Non-Commercial-NoDerivs License**

## Figure 8 (Demir et al., 2021)

*Requirements to be followed when using an entire IEEE copyrighted paper in a thesis:*

1) The following IEEE copyright/ credit notice should be placed prominently in the references: © [year of original publication] IEEE. Reprinted, with permission, from [author names, paper title, IEEE publication title, and month/year of publication]
2) Only the accepted version of an IEEE copyrighted paper can be used when posting the paper or your thesis on-line.
3) In placing the thesis on the author's university website, please display the following message in a prominent place on the website: In reference to IEEE copyrighted material which is used with permission in this thesis, the IEEE does not endorse any of [university/educational entity's name goes here]'s products or services. Internal or personal use of this material is permitted. If interested in reprinting/republishing IEEE copyrighted material for advertising or promotional purposes or for creating new collective works for resale or redistribution, please go to http://www.ieee.org/publications_standards/publications/rights/rights_link.html to learn how to obtain a License from RightsLink.

If applicable, University Microfilms and/or ProQuest Library, or the Archives of Canada may supply single copies of the dissertation.

**Figure 10 (Bern & Plassmann, 2000)**

JOHN WILEY AND SONS LICENSE
TERMS AND CONDITIONS

Jan 04, 2024

---

This Agreement between Mr. Javier Maldonado-Echeverria ("You") and John Wiley and Sons ("John Wiley and Sons") consists of your license details and the terms and conditions provided by John Wiley and Sons and Copyright Clearance Center.

| | |
|---|---|
| License Number | 5693820605299 |
| License date | Dec 21, 2023 |
| Licensed Content Publisher | John Wiley and Sons |
| Licensed Content Publication | Magnetic Resonance in Medicine |
| Licensed Content Title | Characterization of concomitant gradient fields and their effects on image distortions using a low-field point-of-care Halbach-based MRI system |
| Licensed Content Author | Andrew G. Webb, Rob F. Remis, Bart Vos |
| Licensed Content Date | Sep 25, 2023 |
| Licensed Content Volume | 91 |
| Licensed Content Issue | 2 |
| Licensed Content Pages | 14 |
| Type of use | Dissertation/Thesis |

| | |
|---|---|
| Requestor type | University/Academic |
| Format | Print and electronic |
| Portion | Figure/table |
| Number of figures/tables | 1 |
| Will you be translating? | No |
| Title of new work | Brain Response to Overpressure and Recoil Loads from Discharge of Long-Range Precision Rifle |
| Institution name | University of Waterloo |
| Expected presentation date | Jan 2024 |
| Order reference number | Wiley2 |
| Portions | Figure 2: Two-dimensional brain phantoms corresponding to transverse, sagittal and coronal brain slabs. With relaxation parameters of the compartments approximately equal to in vivo data at 50 mT |
| Requestor Location | Mr. Javier Maldonado-Echeverria<br>350 Columbia Street West<br>Unit 313<br>Waterloo, ON N2L6P4<br>Canada<br>Attn: Mr. Javier Maldonado-Echeverria |
| Publisher Tax ID | EU826007151 |
| Total | 0.00 CAD |

Terms and Conditions

**TERMS AND CONDITIONS**

WILEY or its licensors is granted hereunder, and you agree that you shall not assert any such right, license or interest with respect thereto

- NEITHER WILEY NOR ITS LICENSORS MAKES ANY WARRANTY OR REPRESENTATION OF ANY KIND TO YOU OR ANY THIRD PARTY, EXPRESS, IMPLIED OR STATUTORY, WITH RESPECT TO THE MATERIALS OR THE ACCURACY OF ANY INFORMATION CONTAINED IN THE MATERIALS, INCLUDING, WITHOUT LIMITATION, ANY IMPLIED WARRANTY OF MERCHANTABILITY, ACCURACY, SATISFACTORY QUALITY, FITNESS FOR A PARTICULAR PURPOSE, USABILITY, INTEGRATION OR NON-INFRINGEMENT AND ALL SUCH WARRANTIES ARE HEREBY EXCLUDED BY WILEY AND ITS LICENSORS AND WAIVED BY YOU.

- WILEY shall have the right to terminate this Agreement immediately upon breach of this Agreement by you.

- You shall indemnify, defend and hold harmless WILEY, its Licensors and their respective directors, officers, agents and employees, from and against any actual or threatened claims, demands, causes of action or proceedings arising from any breach of this Agreement by you.

- IN NO EVENT SHALL WILEY OR ITS LICENSORS BE LIABLE TO YOU OR ANY OTHER PARTY OR ANY OTHER PERSON OR ENTITY FOR ANY SPECIAL, CONSEQUENTIAL, INCIDENTAL, INDIRECT, EXEMPLARY OR PUNITIVE DAMAGES, HOWEVER CAUSED, ARISING OUT OF OR IN CONNECTION WITH THE DOWNLOADING, PROVISIONING, VIEWING OR USE OF THE MATERIALS REGARDLESS OF THE FORM OF ACTION, WHETHER FOR BREACH OF CONTRACT, BREACH OF WARRANTY, TORT, NEGLIGENCE, INFRINGEMENT OR OTHERWISE (INCLUDING, WITHOUT LIMITATION, DAMAGES BASED ON LOSS OF PROFITS, DATA, FILES, USE, BUSINESS OPPORTUNITY OR CLAIMS OF THIRD PARTIES), AND WHETHER OR NOT THE PARTY HAS BEEN ADVISED OF THE POSSIBILITY OF SUCH DAMAGES. THIS LIMITATION SHALL APPLY NOTWITHSTANDING ANY FAILURE OF ESSENTIAL PURPOSE OF ANY LIMITED REMEDY PROVIDED HEREIN.

- Should any provision of this Agreement be held by a court of competent jurisdiction to be illegal, invalid, or unenforceable, that provision shall be deemed amended to achieve as nearly as possible the same economic effect as the original provision, and the legality, validity and enforceability of the remaining provisions of this Agreement shall not be affected or impaired thereby.

- The failure of either party to enforce any term or condition of this Agreement shall not constitute a waiver of either party's right to enforce each and every term and condition of this Agreement. No breach under this agreement shall be deemed waived or excused by either party unless such waiver or consent is in writing signed by the party granting such waiver or consent. The waiver by or consent of a party to a breach of any provision of this Agreement shall not operate or be construed as a waiver of or consent to any other or subsequent breach by such other party.

- This Agreement may not be assigned (including by operation of law or otherwise) by you without WILEY's prior written consent.

- Any fee required for this permission shall be non-refundable after thirty (30) days from receipt by the CCC.

- These terms and conditions together with CCC's Billing and Payment terms and conditions (which are incorporated herein) form the entire agreement between you and WILEY concerning this licensing transaction and (in the absence of fraud) supersedes all prior agreements and representations of the parties, oral or written. This Agreement may not be amended except in writing signed by both parties. This Agreement shall be binding upon and inure to the benefit of the parties' successors, legal representatives, and authorized assigns.

- In the event of any conflict between your obligations established by these terms and conditions and those established by CCC's Billing and Payment terms and conditions, these terms and conditions shall prevail.

- WILEY expressly reserves all rights not specifically granted in the combination of (i) the license details provided by you and accepted in the course of this licensing transaction, (ii) these terms and conditions and (iii) CCC's Billing and Payment terms and conditions.

- This Agreement will be void if the Type of Use, Format, Circulation, or Requestor Type was misrepresented during the licensing process.

- This Agreement shall be governed by and construed in accordance with the laws of the State of New York, USA, without regards to such state's conflict of law rules. Any legal action, suit or proceeding arising out of or relating to these Terms and Conditions or the breach thereof shall be instituted in a court of competent jurisdiction in New York County in the State of New York in the United States of America and each party hereby consents and submits to the personal jurisdiction of such court, waives any objection to venue in such court and consents to service of process by registered or certified mail, return receipt requested, at the last known address of such party.

**WILEY OPEN ACCESS TERMS AND CONDITIONS**

Wiley Publishes Open Access Articles in fully Open Access Journals and in Subscription journals offering Online Open. Although most of the fully Open Access journals publish open access articles under the terms of the Creative Commons Attribution (CC BY) License only, the subscription journals and a few of the Open Access Journals offer a choice of Creative Commons Licenses. The license type is clearly identified on the article.

**The Creative Commons Attribution License**

The Creative Commons Attribution License (CC-BY) allows users to copy, distribute and transmit an article, adapt the article and make commercial use of the article. The CC-BY license permits commercial and non-

**Creative Commons Attribution Non-Commercial License**

The Creative Commons Attribution Non-Commercial (CC-BY-NC)License permits use, distribution and reproduction in any medium, provided the original work is properly cited and is not used for commercial purposes.(see below)

**Creative Commons Attribution-Non-Commercial-NoDerivs License**

---

# Figure 14 (Donea et al., 2004)

JOHN WILEY AND SONS LICENSE
TERMS AND CONDITIONS

Jan 04, 2024

---

This Agreement between Mr. Javier Maldonado-Echeverria ("You") and John Wiley and Sons ("John Wiley and Sons") consists of your license details and the terms and conditions provided by John Wiley and Sons and Copyright Clearance Center.

| | |
|---|---|
| License Number | 5693820412155 |
| License date | Dec 21, 2023 |
| Licensed Content Publisher | John Wiley and Sons |
| Licensed Content Publication | Wiley Books |
| Licensed Content Title | Arbitrary Lagrangian–Eulerian Methods |
| Licensed Content Author | Antonio Rodríguez-Ferran, Jean-Philippe Ponthot, Antonio Huerta, et al |
| Licensed Content Date | Dec 15, 2017 |
| Licensed Content Pages | 23 |
| Type of use | Dissertation/Thesis |
| Requestor type | University/Academic |
| Format | Print and electronic |
| Portion | Figure/table |
| Number of figures/tables | 1 |

| | |
|---|---|
| Will you be translating? | No |
| Title of new work | Brain Response to Overpressure and Recoil Loads from Discharge of Long-Range Precision Rifle |
| Institution name | University of Waterloo |
| Expected presentation date | Jan 2024 |
| Order reference number | Wiley1 |
| Portions | Figure 14.1: One-dimensional example of Lagrangian, Eulerian and ALE mesh and particle motion. |
| Requestor Location | Mr. Javier Maldonado-Echeverria<br>350 Columbia Street West<br>Unit 313<br><br>Waterloo, ON N2L6P4<br>Canada<br>Attn: Mr. Javier Maldonado-Echeverria |
| Publisher Tax ID | EU826007151 |
| Total | 0.00 CAD |
| Terms and Conditions | |

**TERMS AND CONDITIONS**

This copyrighted material is owned by or exclusively licensed to John Wiley & Sons, Inc. or one of its group companies (each a"Wiley Company") or handled on behalf of a society with which a Wiley Company has exclusive publishing rights in relation to a particular work (collectively "WILEY"). By clicking "accept" in connection with completing this licensing transaction, you agree that the following terms and conditions apply to this transaction (along with the billing and payment terms and conditions established by the Copyright Clearance Center Inc., ("CCC's Billing and Payment terms and conditions"), at the time that you opened your RightsLink account (these are available at any time at http://myaccount.copyright.com).

**Terms and Conditions**

- The materials you have requested permission to reproduce or reuse (the "Wiley Materials") are protected by copyright.

- You are hereby granted a personal, non-exclusive, non-sub licensable (on a stand-alone basis), non-transferable, worldwide, limited license to reproduce the Wiley Materials for the purpose specified in the licensing process. This license, **and any CONTENT (PDF or image file) purchased as part of your order,** is for a one-time use only and limited to any maximum distribution number specified in the license. The first instance of republication or reuse granted by this license must be completed within two years of the date of the grant of this license (although copies prepared before the end date may be distributed thereafter). The Wiley Materials shall not be used in any other manner or for any other purpose, beyond what is granted in the license. Permission is granted subject to an appropriate acknowledgement given to the author, title of the material/book/journal and the publisher. You shall also duplicate the copyright notice that appears in the Wiley publication in your use of the Wiley Material. Permission is also granted on the understanding that nowhere in the text is a previously published source acknowledged for all or part of this Wiley Material. Any third party content is expressly excluded from this permission.

- With respect to the Wiley Materials, all rights are reserved. Except as expressly granted by the terms of the license, no part of the Wiley Materials may be copied, modified, adapted (except for minor reformatting required by the new Publication), translated, reproduced, transferred or distributed, in any form or by any means, and no derivative works may be made based on the Wiley Materials without the prior permission of the respective copyright owner.**For STM Signatory Publishers clearing permission under the terms of the STM Permissions Guidelines only, the terms of the license are extended to include subsequent editions and for editions in other languages, provided such editions are for the work as a whole in situ and does not involve the separate exploitation of the permitted figures or extracts,** You may not alter, remove or suppress in any manner any copyright, trademark or other notices displayed by the Wiley Materials. You may not license, rent, sell, loan, lease, pledge, offer as security, transfer or assign the Wiley Materials on a stand-alone basis, or any of the rights granted to you hereunder to any other person.

- The Wiley Materials and all of the intellectual property rights therein shall at all times remain the exclusive property of John Wiley & Sons Inc, the Wiley Companies, or their respective licensors, and your interest therein is only that of having possession of and the right to reproduce the Wiley Materials pursuant to Section 2 herein during the continuance of this Agreement. You agree that you own no right, title or interest in or to the Wiley Materials or any of the intellectual property rights therein. You shall have no rights hereunder other than the license as provided for above in Section 2. No right, license or interest to any trademark, trade name, service mark or other branding ("Marks") of WILEY or its licensors is granted hereunder, and you agree that you shall not assert any such right, license or interest with respect thereto

- NEITHER WILEY NOR ITS LICENSORS MAKES ANY WARRANTY OR REPRESENTATION OF ANY KIND TO YOU OR ANY THIRD PARTY, EXPRESS, IMPLIED OR STATUTORY, WITH RESPECT TO THE MATERIALS OR THE ACCURACY OF ANY INFORMATION CONTAINED IN THE MATERIALS, INCLUDING, WITHOUT LIMITATION, ANY IMPLIED WARRANTY OF MERCHANTABILITY, ACCURACY, SATISFACTORY QUALITY, FITNESS FOR A PARTICULAR PURPOSE, USABILITY, INTEGRATION OR NON-INFRINGEMENT AND ALL SUCH WARRANTIES ARE HEREBY EXCLUDED BY WILEY AND ITS LICENSORS AND WAIVED BY YOU.

- WILEY shall have the right to terminate this Agreement immediately upon breach of this Agreement by you.

- You shall indemnify, defend and hold harmless WILEY, its Licensors and their respective directors, officers, agents and employees, from and against any actual or threatened claims, demands, causes of action or proceedings arising from any breach of this Agreement by you.

- IN NO EVENT SHALL WILEY OR ITS LICENSORS BE LIABLE TO YOU OR ANY OTHER PARTY OR ANY OTHER PERSON OR ENTITY FOR ANY SPECIAL, CONSEQUENTIAL, INCIDENTAL, INDIRECT, EXEMPLARY OR PUNITIVE DAMAGES, HOWEVER CAUSED, ARISING OUT OF OR IN CONNECTION WITH THE DOWNLOADING, PROVISIONING, VIEWING OR USE OF THE MATERIALS REGARDLESS OF THE FORM OF ACTION, WHETHER FOR BREACH OF CONTRACT, BREACH OF WARRANTY, TORT, NEGLIGENCE, INFRINGEMENT OR OTHERWISE (INCLUDING, WITHOUT LIMITATION, DAMAGES BASED ON LOSS OF PROFITS, DATA, FILES, USE, BUSINESS OPPORTUNITY OR CLAIMS OF THIRD PARTIES), AND WHETHER OR NOT THE PARTY HAS BEEN ADVISED OF THE POSSIBILITY OF SUCH DAMAGES. THIS LIMITATION SHALL APPLY NOTWITHSTANDING ANY FAILURE OF ESSENTIAL PURPOSE OF ANY LIMITED REMEDY PROVIDED HEREIN.

- Should any provision of this Agreement be held by a court of competent jurisdiction to be illegal, invalid, or unenforceable, that provision shall be deemed amended to achieve as nearly as possible the same economic effect as the original provision, and the legality, validity and enforceability of the remaining provisions of this Agreement shall not be affected or impaired thereby.

- The failure of either party to enforce any term or condition of this Agreement shall not constitute a waiver of either party's right to enforce each and every term and condition of this Agreement. No breach under this agreement shall be deemed waived or excused by either party unless such waiver or consent is in writing signed by the party granting such waiver or consent. The waiver by or consent of a party to a breach of any provision of this Agreement shall not operate or be construed as a waiver of or consent to any other or subsequent breach by such other party.

- This Agreement may not be assigned (including by operation of law or otherwise) by you without WILEY's prior written consent.

- Any fee required for this permission shall be non-refundable after thirty (30) days from receipt by the CCC.

- These terms and conditions together with CCC's Billing and Payment terms and conditions (which are incorporated herein) form the entire agreement between you and WILEY concerning this licensing transaction and (in the absence of fraud) supersedes all prior agreements and representations of the parties, oral or written. This Agreement may not be amended except in writing signed by both parties. This Agreement shall be binding upon and inure to the benefit of the parties' successors, legal representatives, and authorized assigns.

- In the event of any conflict between your obligations established by these terms and conditions and those established by CCC's Billing and Payment terms and conditions, these terms and conditions shall prevail.

- WILEY expressly reserves all rights not specifically granted in the combination of (i) the license details provided by you and accepted in the course of this licensing transaction, (ii) these terms and conditions and (iii) CCC's Billing and Payment terms and conditions.

- This Agreement will be void if the Type of Use, Format, Circulation, or Requestor Type was misrepresented during the licensing process.

- This Agreement shall be governed by and construed in accordance with the laws of the State of New York, USA, without regards to such state's conflict of law rules. Any legal action, suit or proceeding arising out of or relating to these Terms and Conditions or the breach thereof shall be instituted in a court of competent jurisdiction in New York County in the State of New York in the United States of America and each party hereby consents and submits to the personal jurisdiction of such court, waives any objection to venue in such court and consents to service of process by registered or certified mail, return receipt requested, at the last known address of such party.

**WILEY OPEN ACCESS TERMS AND CONDITIONS**

Wiley Publishes Open Access Articles in fully Open Access Journals and in Subscription journals offering Online Open. Although most of the fully Open Access journals publish open access articles under the terms of the Creative Commons Attribution (CC BY) License only, the subscription journals and a few of the Open Access Journals offer a choice of Creative Commons Licenses. The license type is clearly identified on the article.

**The Creative Commons Attribution License**

The Creative Commons Attribution License (CC-BY) allows users to copy, distribute and transmit an article, adapt the article and make commercial use of the article. The CC-BY license permits commercial and non-

**Creative Commons Attribution Non-Commercial License**

The Creative Commons Attribution Non-Commercial (CC-BY-NC)License permits use, distribution and reproduction in any medium, provided the original work is properly cited and is not used for commercial purposes.(see below)

**Creative Commons Attribution-Non-Commercial-NoDerivs License**

The Creative Commons Attribution Non-Commercial-NoDerivs License (CC-BY-NC-ND) permits use, distribution and reproduction in any medium, provided the original work is properly cited, is not used for commercial purposes and no modifications or adaptations are made. (see below)

**Use by commercial "for-profit" organizations**

Use of Wiley Open Access articles for commercial, promotional, or marketing purposes requires further explicit permission from Wiley and will be subject to a fee.

Further details can be found on Wiley Online Library
http://olabout.wiley.com/WileyCDA/Section/id-410895.html

**Other Terms and Conditions:**

**v1.10 Last updated September 2015**

**Questions? customercare@copyright.com.**

---

# References


Aleksander Lukasz Rycman, by. (2022). *Computational Modeling of the Cervical Spinal Cord: Integration into a Human Body Model to Investigate Response to Impact*.

Beckwith, J. G., Zhao, W., Ji, S., Ajamil, A. G., Bolander, R. P., Chu, J. J., McAllister, T. W., Crisco, J. J., Duma, S. M., Rowson, S., Broglio, S. P., Guskiewicz, K. M., Mihalik, J. P., Anderson, S., Schnebel, B., Gunnar Brolinson, P., Collins, M. W., & Greenwald, R. M. (2018). Estimated Brain Tissue Response Following Impacts Associated With and Without Diagnosed Concussion. *Annals of Biomedical Engineering*, *46*(6), 819. https://doi.org/10.1007/S10439-018-1999-5

Béres, S., & Kovács, Á. (2022). Quality Requirements for Front and Rear Support in Relation to the Precision of a Bolt Action, Big Calibre Precision Rifle. *Hadmérnök*, *17*(3), 5–34. https://doi.org/10.32567/HM.2022.3.1

Bern, M., & Plassmann, P. (2000). Mesh Generation. *Handbook of Computational Geometry*, 291–332. https://doi.org/10.1016/B978-044482537-7/50007-3

Brown, D., & Cox, A. J. (2009). Innovative Uses of Video Analysis. *The Physics Teacher*, *47*(3), 145–150. https://doi.org/10.1119/1.3081296

Bruggeman, G. F., Haitsma, I. K., Dirven, C. M. F., & Volovici, V. (2021). Traumatic axonal injury (TAI): definitions, pathophysiology and imaging—a narrative review. *Acta Neurochirurgica*, *163*(1), 31–44. https://doi.org/10.1007/S00701-020-04594-1/FIGURES/3

Bruneau, D. A., & Cronin, D. S. (2020). Head and Neck Response of an Active Human Body Model and Finite Element Anthropometric Test Device During a Linear Impactor Helmet Test. *Journal of Biomechanical Engineering*, *142*(2). https://doi.org/10.1115/1.4043667

Burns, B. P. (2012). *Recoil Considerations for Shoulder-Fired Weapons*.

Bustamante, M. C., Singh, D., & Cronin, D. S. (2018). Polymeric Hopkinson Bar-Confinement Chamber Apparatus to Evaluate Fluid Cavitation. *Experimental*

*Mechanics*, *58*(1), 55–74. https://doi.org/10.1007/S11340-017-0323-X/FIGURES/23

Carroll, C. P., Cochran, J. A., Price, J. P., Guse, C. E., & Wang, M. C. (2010). The AIS-2005 Revision in Severe Traumatic Brain Injury: Mission Accomplished or Problems for Future Research? *Annals of Advances in Automotive Medicine / Annual Scientific Conference*, *54*, 233. /pmc/articles/PMC3242550/

Cecchi, N. J., Vahid Alizadeh, H., Liu, Y., & Camarillo, D. B. (2023). Finite element evaluation of an American football helmet featuring liquid shock absorbers for protecting against concussive and subconcussive head impacts. *Frontiers in Bioengineering and Biotechnology*, *11*. https://doi.org/10.3389/FBIOE.2023.1160387

Chafi, M. S., Ganpule, S., Gu, L., & Chandra, N. (2012). DYNAMIC RESPONSE OF BRAIN SUBJECTED TO BLAST LOADINGS: INFLUENCE OF FREQUENCY RANGES. *Https://Doi.Org/10.1142/S175882511100124X*, *3*(4), 803–823. https://doi.org/10.1142/S175882511100124X

Chaturvedi, E., & Dwivedi, R. K. (2018). Review of various designs and material research studies of muzzle brakes with a proposal of an improved design. *Materials Today: Proceedings*, *5*, 18681–18688. www.sciencedirect.comwww.materialstoday.com/proceedings2214-7853

Cheng, Y., Kheng Leow, W., & Chye Lim, T. (2012). Automatic identification of Frankfurt plane and mid-sagittal plane of skull. *Proceedings of IEEE Workshop on Applications of Computer Vision*, 233–238. https://doi.org/10.1109/WACV.2012.6162994

Corrales, M. A., Gierczycka, D., Barker, J., Bruneau, D., Bustamante, M. C., & Cronin, D. S. (2020). Validation of a Football Helmet Finite Element Model and Quantification of Impact Energy Distribution. *Annals of Biomedical Engineering*, *48*(1), 121–132. https://doi.org/10.1007/s10439-019-02359-1

de Vos, B., Remis, R. F., & Webb, A. G. (2023). Characterization of concomitant gradient fields and their effects on image distortions using a low-field point-of-care Halbach-based MRI system. *Magnetic Resonance in Medicine*. https://doi.org/10.1002/MRM.29879

Deck, C., & Willinger, R. (2008). Improved head injury criteria based on head FE model. *International Journal of Crashworthiness*, *13*(6), 667–678. https://doi.org/10.1080/13588260802411523

Demir, C., Koga, S., & Krstic, M. (2021). *Neuron Growth Control by PDE Backstepping: Axon Length Regulation by Tubulin Flux Actuation in Soma*. http://arxiv.org/abs/2109.14095

Denny-Brown, D. E., & Russell, W. R. (1941). Experimental Concussion: (Section of Neurology). *Proceedings of the Royal Society of Medicine*, *34*(11), 691. /pmc/articles/PMC1998140/?report=abstract

Donea, J., Huerta, A., Ponthot, J.-Ph., & Rodrï¿½ï¿½guez-Ferran, A. (2004). Arbitrary Lagrangian-Eulerian Methods. *Encyclopedia of Computational Mechanics*. https://doi.org/10.1002/0470091355.ECM009

Du, Z., Li, Z., Wang, P., Wang, X., Zhang, J., Zhuang, Z., & Liu, Z. (2022). Revealing the Effect of Skull Deformation on Intracranial Pressure Variation During the Direct Interaction Between Blast Wave and Surrogate Head. *Annals of Biomedical Engineering*, *50*(9), 1038–1052. https://doi.org/10.1007/S10439-022-02982-5

Ern, A., & Guermond, J.-L. (2021). *Finite Elements I. 72*. https://doi.org/10.1007/978-3-030-56341-7

Fargen, K. M. (2021). Basic Brain Anatomy and Physiology. *Idiopathic Intracranial Hypertension Explained*, 3–20. https://doi.org/10.1007/978-3-030-80042-0_2

François, D., Pineau, A., & Zaoui, A. (2012). *Mechanical Behaviour of Materials*. *180*. https://doi.org/10.1007/978-94-007-2546-1

Gabler, L. F., Crandall, J. R., & Panzer, M. B. (2016a). Assessment of Kinematic Brain Injury Metrics for Predicting Strain Responses in Diverse Automotive Impact

Conditions. *Annals of Biomedical Engineering*, *44*(12), 3705–3718. https://doi.org/10.1007/s10439-016-1697-0

Gabler, L. F., Crandall, J. R., & Panzer, M. B. (2016b). Investigating brain injury tolerance in the sagittal plane using a finite element model of the human head. *International Journal of Automotive Engineering*, *7*(1), 37–43. https://doi.org/10.20485/JSAEIJAE.7.1_37

Gabler, L. F., Crandall, J. R., & Panzer, M. B. (2019). Development of a Second-Order System for Rapid Estimation of Maximum Brain Strain. *Annals of Biomedical Engineering*, *47*(9), 1971–1981. https://doi.org/10.1007/S10439-018-02179-9

Galbraith, J. A., Thibault, L. E., & Matteson, D. R. (1993). Mechanical and electrical responses of the squid giant axon to simple elongation. *Journal of Biomechanical Engineering*, *115*(1), 13–22. https://doi.org/10.1115/1.2895464

Gao, X., Deng, P., Xu, Z. C., & Chen, J. (2011). Moderate traumatic brain injury causes acute dendritic and synaptic degeneration in the hippocampal dentate gyrus. *PloS One*, *6*(9). https://doi.org/10.1371/JOURNAL.PONE.0024566

Halabi, C. (2021). Concussion. *Aminoff's Neurology and General Medicine*, 673–680. https://doi.org/10.1016/B978-0-12-819306-8.00037-X

Hardy, C. H., & Marcal, P. V. (1973). Elastic Analysis of a Skull. *Journal of Applied Mechanics*, *40*(4), 838–842. https://doi.org/10.1115/1.3423172

Hazell, P. J. (2021). The Story of the Gun. *The Story of the Gun*. https://doi.org/10.1007/978-3-030-73652-1

HEADQUARTERS, D. O. T. A. U. (1994). *FM 23-10 BASIC FIELD MANUAL*.

Henninger, H. B., Reese, S. P., Anderson, A. E., & Weiss, J. A. (2010). Validation of computational models in biomechanics. *Proceedings of the Institution of Mechanical Engineers. Part H, Journal of Engineering in Medicine*, *224*(7), 801–812. https://doi.org/10.1243/09544119JEIM649

Huang, X., Chang, L., Zhao, H., & Cai, Z. (2022). Study on craniocerebral dynamics response and helmet protective performance under the blast waves. *Materials & Design*, *224*, 111408. https://doi.org/10.1016/J.MATDES.2022.111408

Huang, X., Hu, X., Zhang, L., & Cai, Z. (2021). Craniocerebral Dynamic Response and Cumulative Effect of Damage Under Repetitive Blast. *Annals of Biomedical Engineering*, *49*(10), 2932–2943. https://doi.org/10.1007/S10439-021-02746-7/TABLES/8

Iverson, G. L., Castellani, R. J., Cassidy, J. D., Schneider, G. M., Schneider, K. J., Echemendia, R. J., Bailes, J. E., Hayden, K. A., Koerte, I. K., Manley, G. T., McNamee, M., Patricios, J. S., Tator, C. H., Cantu, R. C., & Dvorak, J. (2023). Examining later-in-life health risks associated with sport-related concussion and repetitive head impacts: a systematic review of case-control and cohort studies. *British Journal of Sports Medicine*, *57*(12), 810–824. https://doi.org/10.1136/BJSPORTS-2023-106890

James, D. R., & Dyer, J. L. (2011). *Rifle Marksmanship Diagnostic and Training Guide*. https://www.researchgate.net/publication/235064576_Rifle_Marksmanship_Diagnostic_and_Training_Guide

Kamimori, G. H., Reilly, L. A., LaValle, C. R., & Olaghere Da Silva, U. B. (2017). Occupational overpressure exposure of breachers and military personnel. *Shock Waves*, *27*(6), 837–847. https://doi.org/10.1007/s00193-017-0738-4

Keith Hudson, M., Luchinh, C., Keith Clutter, J., & Shyys, W. (1996). CFD approach to firearms sound suppressor design. *32nd Joint Propulsion Conference and Exhibit*, 1–12. https://doi.org/10.2514/6.1996-3020

Kenner, V. H., & Goldsmith, W. (1972). Dynamic loading of a fluid-filled spherical shell. *International Journal of Mechanical Sciences*, *14*(9), 557–568. https://doi.org/10.1016/0020-7403(72)90056-2

Khalil, T. B., & Hubbard, R. P. (1977). Parametric study of head response by finite element modeling. *Journal of Biomechanics*, *10*(2), 119–132. https://doi.org/10.1016/0021-9290(77)90075-6

Khaniki, H. B., Ghayesh, M. H., Chin, R., & Amabili, M. (2023). Hyperelastic structures: A review on the mechanics and biomechanics. *International Journal of Non-Linear Mechanics*, *148*, 104275. https://doi.org/10.1016/J.IJNONLINMEC.2022.104275

Kilikevičius, A., Giedraitis, V., Kilikevičienė, K., Matijošius, J., Selech, J., Buckiūnas, G., & Rucki, M. (2023). Performance Analysis of Different Gun Silencers. *Applied Sciences (Switzerland)*, *13*(7). https://doi.org/10.3390/APP13074426

Knowles, B. M., & Dennison, C. R. (2017). Predicting Cumulative and Maximum Brain Strain Measures From HybridIII Head Kinematics: A Combined Laboratory Study and Post-Hoc Regression Analysis. *Annals of Biomedical Engineering*, *45*(9), 2146. https://doi.org/10.1007/S10439-017-1848-Y

Kong, L. Z., Zhang, R. L., Hu, S. H., & Lai, J. B. (2022). Military traumatic brain injury: a challenge straddling neurology and psychiatry. *Military Medical Research*, *9*(1), 1–18. https://doi.org/10.1186/S40779-021-00363-Y/TABLES/3

Koptyug, A., & Ainegren, M. (2015). Experimental measurement of rifle dynamics during the range shooting of biathlon weapons. *Procedia Engineering*, *112*, 349–354. https://doi.org/10.1016/j.proeng.2015.07.261

Labus, K. M., & Puttlitz, C. M. (2016). Viscoelasticity of brain corpus callosum in biaxial tension. *Journal of the Mechanics and Physics of Solids*, *96*, 591–604. https://doi.org/10.1016/J.JMPS.2016.08.010

Li, P. fei, & Zhang, X. bing. (2021). Numerical research on adverse effect of muzzle flow formed by muzzle brake considering secondary combustion. *Defence Technology*, *17*(4), 1178–1189. https://doi.org/10.1016/J.DT.2020.06.019

Li, W., Shepherd, D. E. T., & Espino, D. M. (2021). Investigation of the Compressive Viscoelastic Properties of Brain Tissue Under Time and Frequency Dependent

Loading Conditions. *Annals of Biomedical Engineering*, *49*(12), 3737–3747. https://doi.org/10.1007/S10439-021-02866-0

Lynch, P. J., & Jaffe, C. C. (2006). Skull and brain sagittal section. Multimedia teaching projects by the Yale University School of Medicine, Center for Advanced Instructional Media. Yale University Center for Advanced Instructional Media Medical Illustrations, New Haven, Connecticut, USA.

Liu, J. B., Huang, H. S., Zhu, W. F., Liu, Y., & Zhang, L. (2020). Research on high efficiency muzzle brake technology of small caliber automatic gun. *Journal of Physics: Conference Series*, *1507*(3). https://doi.org/10.1088/1742-6596/1507/3/032003

Lockhart, P. A. (2010). *Primary Blast Injury of the Head: Numerical Prediction and Evaluation of Protection*. https://uwspace.uwaterloo.ca/handle/10012/5422

Lotfy, M., & Ezzeldin, M. (2023). Development of a lightweight mitigation system for severe explosions with small-scaled distances. *Engineering Structures*, *296*, 116932. https://doi.org/10.1016/J.ENGSTRUCT.2023.116932

LS-DYNA ®. (2021). *LS-DYNA® KEYWORD USER'S MANUAL: Vol. Vol 1*. www.lstc.com

Lyu, D., Zhou, R., Lin, C. H., Prasad, P., & Zhang, L. (2022). Development and Validation of a New Anisotropic Visco-Hyperelastic Human Head Finite Element Model Capable of Predicting Multiple Brain Injuries. *Frontiers in Bioengineering and Biotechnology*, *10*. https://doi.org/10.3389/FBIOE.2022.831595

Maas, S. A., Ellis, B. J., Ateshian, G. A., & Weiss, J. A. (2012). FEBio: Finite elements for biomechanics. *Journal of Biomechanical Engineering*, *134*(1). https://doi.org/10.1115/1.4005694/455684

Maddy, K., Harris, D., Costello, M., Araya, N., Pierre, K., & Lucke-Wold, B. (2023). Recent advances in the understanding of the pathophysiology of neurotrauma. In *Horizons in Neuroscience Research. Volume 49* (pp. 115–150). Nova Science Publishers, Inc.

Madhukar, A., & Ostoja-Starzewski, M. (2019). Finite Element Methods in Human Head Impact Simulations: A Review. *Annals of Biomedical Engineering*, *47*(9), 1832–1854. https://doi.org/10.1007/S10439-019-02205-4

Maksimovic, G. (2021). *ISSF National Coach Course Shooting Positions*.

Mathews, A., Iboaya, A., Smith, J. A. D., & Bell, K. R. (2020). Acute Management of Concussion and Diagnostic Criteria. *Concussion: Assessment, Management and Rehabilitation*, 1–12. https://doi.org/10.1016/B978-0-323-65384-8.00001-8

Mcallister, T. W., Ford, J. C., Beckwith, J. G., Flashman, L. A., Paulsen, K., Greenwald, R. M., McAllister, T. W., & Biomed Eng, A. (2012). Maximum Principal Strain and Strain Rate Associated with Concussion Diagnosis Correlates with Changes in Corpus Callosum White Matter Indices HHS Public Access Author manuscript. *Ann Biomed Eng*, *40*(1), 127–140. https://doi.org/10.1007/s10439-011-0402-6

McGowan, A. L., Bretzin, A. C., Anderson, M., Pontifex, M. B., & Covassin, T. (2021). Paired cognitive flexibility task with symptom factors improves detection of sports-related concussion in high school and collegiate athletes. *Journal of the Neurological Sciences*, *428*, 117575. https://doi.org/10.1016/J.JNS.2021.117575

Menorca, R. M. G., Fussell, T. S., & Elfar, J. C. (2013). Peripheral Nerve Trauma: Mechanisms of Injury and Recovery. *Hand Clinics*, *29*(3), 317. https://doi.org/10.1016/J.HCL.2013.04.002

Miller, L. E., Urban, J. E., Davenport, E. M., Powers, A. K., Whitlow, C. T., Maldjian, J. A., & Stitzel, J. D. (2021). Brain Strain: Computational Model-Based Metrics for Head Impact Exposure and Injury Correlation. *Annals of Biomedical Engineering*, *49*(3), 1083–1096. https://doi.org/10.1007/S10439-020-02685-9

Miller, M. R., DiBattista, A., Patel, M. A., Daley, M., Tenn, C., Nakashima, A., Rhind, S. G., Vartanian, O., Shiu, M. Y., Caddy, N., Garrett, M., Saunders, D., Smith, I., Jetly, R., & Fraser, D. D. (2022). A Distinct Metabolite Signature in Military Personnel Exposed to Repetitive Low-Level Blasts. *Frontiers in Neurology*, *13*. https://doi.org/10.3389/fneur.2022.831792

Mollaee, S., Budgett, D. M., Taberner, A. J., & Nielsen, P. M. F. (2023). Hyperelastic constitutive model parameters identification using optical-based techniques and hybrid optimisation. *International Journal of Mechanics and Materials in Design*, 1–17. https://doi.org/10.1007/S10999-023-09673-6/TABLES/5

Morelli, F., Neugebauer, J. M., LaFiandra, M. E., Burcham, P., & Gordon, C. T. (2014). Recoil measurement, mitigation techniques, and effects on small arms weapon design and marksmanship performance. *IEEE Transactions on Human-Machine Systems*, *44*(3), 422–428. https://doi.org/10.1109/THMS.2014.2301715

Mostofi, E., Fatehi, J., & Mostoufi, S. A. (2022). Concussion. *Clinical Guide to Musculoskeletal Medicine: A Multidisciplinary Approach*, 11–15. https://doi.org/10.1007/978-3-030-92042-5_2/TABLES/3

Nakashima, A., Vartanian, O., Rhind, S. G., King, K., Tenn, C., & Jetly, C. R. (2022). Repeated Occupational Exposure to Low-level Blast in the Canadian Armed Forces: Effects on Hearing, Balance, and Ataxia. *Military Medicine*, *187*(1–2), E201–E208. https://doi.org/10.1093/milmed/usaa439

Needham, C. E. (2018). *Blast Waves* (R. A. Graham, Ed.; Second Edition). Springer Cham. http://www.springer.com/series/1774

Nelson, N. W., Davenport, N. D., Sponheim, S. R., & Anderson, C. R. (2015). Blast-Related Mild Traumatic Brain Injury. *Brain Neurotrauma: Molecular, Neuropsychological, and Rehabilitation Aspects*, 451–470. https://doi.org/10.1201/b18126

Nelson, T. J., Wall, D. B., Stedje-Larsen, E. T., Clark, R. T., Chambers, L. W., & Bohman, H. R. (2006). Predictors of mortality in close proximity blast injuries during operation iraqi freedom. *Journal of the American College of Surgeons*, *202*(3), 418–422. https://doi.org/10.1016/J.JAMCOLLSURG.2005.11.011

Ouellet, S., & Philippens, M. (2018). The multi-modal responses of a physical head model subjected to various blast exposure conditions. *Shock Waves*, *28*(1), 19–36. https://doi.org/10.1007/S00193-017-0771-3/FIGURES/25

Ouellet, S., & St-Onge, G. (2021). *Measurement of head kinematics of snipers firing a 0.50 caliber rifle*.

Pal, S., & Mitra, N. (2021). Shock wave propagation through air: A reactive molecular dynamics study. *Proceedings of the Royal Society A: Mathematical, Physical and Engineering Sciences*, *477*(2247). https://doi.org/10.1098/RSPA.2020.0676

Panzer, M. B., Myers, B. S., & Bass, C. R. (2013). Mesh considerations for finite element blast modelling in biomechanics. *Computer Methods in Biomechanics and Biomedical Engineering*, *16*(6), 612–621. https://doi.org/10.1080/10255842.2011.629615

Panzer, M. B., Myers, B. S., Capehart, B. P., & Bass, C. R. (2012). Development of a finite element model for blast brain injury and the effects of CSF cavitation. *Annals of Biomedical Engineering*, *40*(7), 1530–1544. https://doi.org/10.1007/S10439-012-0519-2

Peng, S., Wan, S., Yao, Y., Jia, Y., He, L., & Cai, L. (2023). Experimental research and finite element analysis on blast resistance of RRACFST columns. *Structures*, *57*, 105334. https://doi.org/10.1016/J.ISTRUC.2023.105334

Pešić, M., Miljaković, M., Kočović, V., Pešić, Ž. J., Jović, N., Miljojković, J., & Bodić, A. (2023). *OPTIMIZATION AND EFFICIENCY ANALYSIS OF MUZZLE BRAKE FOR SNIPER RIFLE*.

Popović, D. B., & Sinkjær, T. (2013). Diseases and Injuries of the Central Nervous System Leading to Sensory–Motor Impairment. *Introduction to Neural Engineering for Motor Rehabilitation*, 3–20. https://doi.org/10.1002/9781118628522.CH1

R, G., FP, R., MA, F., & CM, S. (2014). Sports-Related Concussions in Youth: Improving the Science, Changing the Culture. *Sports-Related Concussions in Youth*. https://doi.org/10.17226/18377

Roberts, J. C., Harrigan, T. P., Ward, E. E., Taylor, T. M., Annett, M. S., & Merkle, A. C. (2012). Human head-neck computational model for assessing blast injury. *Journal*

*of Biomechanics*, *45*(16), 2899–2906. https://doi.org/10.1016/J.JBIOMECH.2012.07.027

Russo, M. J., Salvat, F., Kañevsky, A., Allegri, R. F., & Sevlever, G. (2023). Acute and subacute clinical markers after sport-related concussion in rugby union players. *Journal of Science and Medicine in Sport*, *26*(7), 345–350. https://doi.org/10.1016/J.JSAMS.2023.05.007

Schmitt, K.-U., Niederer, P. F., Cronin, D. S., Morrison III, B., Muser, M. H., & Walz, F. (2019a). Head Injuries. *Trauma Biomechanics*, 87–115. https://doi.org/10.1007/978-3-030-11659-0_4

Schmitt, K.-U., Niederer, P. F., Cronin, D. S., Morrison III, B., Muser, M. H., & Walz, F. (2019b). Methods in Trauma Biomechanics. *Trauma Biomechanics*, 15–61. https://doi.org/10.1007/978-3-030-11659-0_2

Seeburrun, T., Hartlen, D. C., Bustamante, M. C., Azar, A., Ouellet, S., & Cronin, D. S. (2023). Application of Measured Head Kinematics to Finite Element Head Model and Assessment of Brain Response in Human Volunteers Subject to Acceleration Events from Rifle Recoil. *ICORBI*, 83–84.

Sherif Said, M., Abdelsalam, O. R., & Aboul, M. H. (2018). Design Optimisation of Muzzle Brake for Sniper Rifle. *Article in Defence Science Journal*, *68*(5), 438–444. https://doi.org/10.14429/dsj.68.12754

Shires, D., Zirilli, J., An, M., Olsen, R., Amato, M., Adams, J., & Breczinski, K. (2020). *Tools and Processes for Assessment of Blast Overpressure-Related Traumatic Brain Injury*.

Shreiber, D. I., Bain, A. C., & Meaney, D. F. (1997). In Vivo Thresholds for Mechanical Injury to the Blood-Brain Barrier. *SAE Technical Papers*. https://doi.org/10.4271/973335

Shugar, T. A. (1975). Transient Structural Response of the Linear Skull-Brain System. *SAE Technical Papers*. https://doi.org/10.4271/751161

Singh, D. (2015). *Investigation of Primary Blast Injury and Protection using Sagittal and Transverse Finite Element Head Models*.

Singh, D., & Cronin, D. (2019). Multi-Scale Modeling of Head Kinematics and Brain Tissue Response to Blast Exposure. *Annals of Biomedical Engineering*, *47*(9), 1993–2004. https://doi.org/10.1007/s10439-018-02193-x

Singh, D., & Cronin, D. S. (2017). Efficacy of visor and helmet for blast protection assessed using a computational head model. *Shock Waves*, *27*(6), 905–918. https://doi.org/10.1007/s00193-017-0732-x

Singh, D., Cronin, D. S., & Haladuick, T. N. (2014). Head and brain response to blast using sagittal and transverse finite element models. *International Journal for Numerical Methods in Biomedical Engineering*, *30*(4), 470–489. https://doi.org/10.1002/CNM.2612

Skotak, M., LaValle, C., Misistia, A., Egnoto, M. J., Chandra, N., & Kamimori, G. (2019). Occupational blast wave exposure during multiday 0.50 caliber rifle course. *Frontiers in Neurology*, *10*(JUL). https://doi.org/10.3389/fneur.2019.00797

Spitzer, V., Ackerman, M. J., Scherzinger, A. L., & Whitlock, D. (1996). The visible human male: a technical report. *Journal of the American Medical Informatics Association*, *3*(2), 118. https://doi.org/10.1136/JAMIA.1996.96236280

Stemper, B. D., Shah, A. S., Pintar, F. A., McCrea, M., Kurpad, S. N., Glavaski-Joksimovic, A., Olsen, C., & Budde, M. D. (2015). Head Rotational Acceleration Characteristics Influence Behavioral and Diffusion Tensor Imaging Outcomes Following Concussion. *Annals of Biomedical Engineering*, *43*(5), 1071. https://doi.org/10.1007/S10439-014-1171-9

Sutar, S., & Ganpule, S. (2022). Evaluation of Blast Simulation Methods for Modeling Blast Wave Interaction With Human Head. *Journal of Biomechanical Engineering*, *144*(5). https://doi.org/10.1115/1.4053059

Sweeney, P. (2017). *The Suppressor Handbook*.

Takhounts, E. G., Craig, M. J., Moorhouse, K., McFadden, J., & Hasija, V. (2013). Development of brain injury criteria (BrIC). *Stapp Car Crash Journal*, *57*(November), 243–266. https://doi.org/10.4271/2013-22-0010

Tierney, G. (2021). Concussion biomechanics, head acceleration exposure and brain injury criteria in sport: a review. *Sports Biomechanics*. https://doi.org/10.1080/14763141.2021.2016929

Tse, K., Lim, S., Tan, V., & Lee, H. (2015). A Review of Head Injury and Finite Element Head Models. *Journal of Engineering and Technology*.

Tse, K. M., Tan, L. Bin, Lee, S. J., Lim, S. P., & Lee, H. P. (2014). Development and validation of two subject-specific finite element models of human head against three cadaveric experiments. *International Journal for Numerical Methods in Biomedical Engineering*, *30*(3), 397–415. https://doi.org/10.1002/CNM.2609

Van Sligtenhorst, C., Cronin, D. S., & Wayne Brodland, G. (2006). High strain rate compressive properties of bovine muscle tissue determined using a split Hopkinson bar apparatus. *Journal of Biomechanics*, *39*(10), 1852–1858. https://doi.org/10.1016/J.JBIOMECH.2005.05.015

Virzi Mariotti, G., Golfo, S., Nigrelli, V., & Carollo, F. (2019). Head Injury Criterion: Mini Review. *Am J Biomed Sci & Res*, *5*, 2019–2024. https://doi.org/10.34297/AJBSR.2019.05.000957

Wang, F., Wu, J., Hu, L., Yu, C., Wang, B., Huang, X., Miller, K., & Wittek, A. (2022). Evaluation of the head protection effectiveness of cyclist helmets using full-scale computational biomechanics modelling of cycling accidents. *Journal of Safety Research*, *80*, 109–134. https://doi.org/10.1016/J.JSR.2021.11.005

Wang, Y., Wang, Y. P., & Xu, C. (2020). Experimental study: Effects of typical man-rifle parameters on aiming performance. *Journal of Physics: Conference Series*, *1507*(10). https://doi.org/10.1088/1742-6596/1507/10/102012

Ward, C., Chan, M., & Nahum, A. (1980). Intracranial Pressure–A Brain Injury Criterion. *SAE Technical Papers*, 161–185. https://doi.org/10.4271/801304

Willinger, R., & Baumgartner, D. (2003). Numerical and physical modelling of the human head under impact - Towards new injury criteria. *International Journal of Vehicle Design*, *32*(1–2), 94–115. https://doi.org/10.1504/IJVD.2003.003239

Wittek, A., & Omori, K. (2003). Parametric study of effects of brain-skull boundary conditions and brain material properties on responses of simplified finite element brain model under angular acceleration impulse in sagittal plane. *JSME International Journal, Series C: Mechanical Systems, Machine Elements and Manufacturing*, *46*(4), 1388–1399. https://doi.org/10.1299/JSMEC.46.1388

Woodall, J. l. a, Sak, J. a, Cowdrick, K. R., Bove Muñoz, B. m, McElrath, J. h, Trimpe, G. r, Mei, Y., Myhre, R. l, Rains, J. k, & Hutchinson, C. r. (2023). Repetitive Low-level Blast Exposure and Neurocognitive Effects in Army Ranger Mortarmen. *Military Medicine*, *188*(3–4). https://doi.org/10.1093/MILMED/USAB394

Wu, T., Hajiaghamemar, M., Giudice, J. S., Alshareef, A., Margulies, S. S., & Panzer, M. B. (2021). Evaluation of Tissue-Level Brain Injury Metrics Using Species-Specific Simulations. *Journal of Neurotrauma*, *38*(13), 1879–1888. https://doi.org/10.1089/NEU.2020.7445

Yang, J., Dai, J., & Zhuang, Z. (2009). Human Head Modeling and Personal Head Protective Equipment: A Literature Review. *Lecture Notes in Computer Science (Including Subseries Lecture Notes in Artificial Intelligence and Lecture Notes in Bioinformatics)*, *5620 LNCS*, 661–670. https://doi.org/10.1007/978-3-642-02809-0_70/COVER

Zhang, L., Yang, K. H., & King, A. I. (2004). A Proposed Injury Threshold for Mild Traumatic Brain Injury. *Journal of Biomechanical Engineering*, *126*(2), 226–236. https://doi.org/10.1115/1.1691446

Zhu, F., Chou, C. C., Yang, K. H., & King, A. I. (2013). Some considerations on the threshold and inter-species scaling law for primary blast-induced traumatic brain injury: A semi-analytical approach. *Journal of Mechanics in Medicine and Biology*, *13*(4). https://doi.org/10.1142/S0219519413500656

Zohdi, T. I. (2015). Accuracy of the finite element method. *SpringerBriefs in Applied Sciences and Technology*, *9783319090351*, 69–74. https://doi.org/10.1007/978-3-319-09036-8_8/FIGURES/1

# Appendix A: Constants for Cross-correlation of Experimental Data

```
##########################################################################################
#
#   CORA v3.6
#
##########################################################################################
#
##########################################################################################
#
#   Global Parameters
#
##########################################################################################
BEGIN GLOBAL_PARAMETERS
  DES_MOD            Test and CAE                  ; Header of the evaluation
  DES_GLO            CORA sample data set loadcase 01 ; Sub-header of the evaluation
#
# Global settings to define the interval of evaluation
  A_THRES            0.030                ; Threshold to set the start of the interval of evaluation [0,...,1]
  B_THRES            0.075                ; Threshold to set the end of the interval of evaluation [0,...,1]
  A_EVAL             0.010                ; Extension of the interval of evaluation [0,...,1]
  B_DELTA_END        0.200                ; Additional parameter to shorten the interval of evaluation (width of the corridor:
A_DELTA_END*Y_NORM) 0 = disabled
  T_MIN/T_MAX        0 250   ; Manually defined start (time) and end (time) of the interval of evaluation (automatic = calculated
for each channel)
#
# Global settings of the corridor method
  K                  1                    ; Transition between ratings of 1 and 0 of the corridor method [-] (1 = linear, 2 = quadratic ...)
  G_1                0.50                 ; Weighting factor of the corridor method [-]
  a_0/b_0            0.05    0.50         ; Width of the inner and outer corridor [-]
  a_sigma/b_sigma    0       0            ; Multiples of the standard deviation to widen the inner and outer corridor [-]
# Global settings of the cross correlation method
  D_MIN              0.0                  ; delta_min as share of the interval of evaluation [0,...,1]
  D_MAX              0.0                  ; delta_max as share of the interval of evaluation [0,...,1]
  INT_MIN            1.0                  ; Minimum overlap of the interval [0,...,1]
  K_V                1                    ; Transition between ratings of 1 and 0 of the progression rating [-] (1 = linear, 2 = quadratic ...)
  K_G                1                    ; Transition between ratings of 1 and 0 of the size rating [-] (1 = linear, 2 = quadratic ...)
  K_P                1                    ; Transition between ratings of 1 and 0 of the phase shift rating [-] (1 = linear, 2 = quadratic ...)
  G_V                0.50                 ; Weighting factors of the progression rating [-]
  G_G                0.50                 ; Weighting factors of the size rating [-]
  G_P                0.00                 ; Weighting factors of the phase shift rating [-]
  G_2                0.50                 ; Weighting factors of the cross correlation method [-]
# Normalisation of the the weighting factors
  WF_NORM            YES                  ; Normalisation of the weighting factors [YES/NO]?
# Signal settings
  ISONAME_1-2/11-12   YES YES             ; Consideration of the position 1/2 (test object, seating position) and 11/12 (fine
location 3 - dummy) of the ISO code [YES/NO]
  MIN_NORM           0.00                 ; Threshold (as fraction of the global absolute maximum amplitude) to start special
treatment of secondary axis [0,...,1]
  Y_NORM             extremum             ; Type of calculation of Y_NORM (extremum or value)
#
# Format settings of the html report
  OUTPUT_FORMAT      Hypergraph           ; Export format (LSPOST, PAMVIEW or Hypergraph)
# Layout of the html report
  FONT_SMALL         12                   ; Size of the small font
  FONT_LARGE         14                   ; Size of the large font
  PreT_LC/PostT_LC   -1  -1               ; Expansion of the plotted interval of the curves (-1: complete curve)
END GLOBAL_PARAMETERS
#
```

# Appendix B: Cumulative Fraction Volume for MPS

```
%%%%%%%%%%%%%%%%%%%%%%%%%%%%%%%%%%%%
%MPS
%%%%%%%%%%%%%%%%%%%%%%%%%%%%%%%%%%%%

%Read data of Strain (Var2), Element ID (x_Eid_), and Volume(Volume)

Data=readtable('Time_Element_MPS_Global.csv');
Data=Data(3:end,2:end);
Data=renamevars(Data,("Var2"),("x_Eid_"));
opts2 = detectImportOptions('Volume');
opts2.SelectedVariableNames = ["x_Eid_","Volume"];
Data2=readtable('Volume',opts2);
Data2=Data2(1:end-2,1:2);

%Organize data in a single table

Data_full=join(Data2,Data);
Data_full=table2array(Data_full);

%Calculate maximum MPS by Element and simplified table

MaxMPS=max(Data_full(:,3:end),[],2);
Data_pro(:,1)=Data_full(:,1);
Data_pro(:,2)=Data_full(:,2);
Data_pro(:,5)=MaxMPS;

%Sort table by MPS

Data_pro=sortrows(Data_pro,5);

%Calculate total volume and volume fractions by element

Total_Vol=sum(Data_pro(:,2));
lim=length(Data_pro(:,1));
for i=1:lim
   Data_pro(i,3)=Data_pro(i,2)/Total_Vol;
end

%Calculate cumulative volume fraction

Data_pro(1,4)=1-Data_pro(1,3);
for i=2:lim
   Data_pro(i,4)=Data_pro(i-1,4)-Data_pro(i,3);
end

%Write results

Data_pro=array2table(Data_pro);
Data_pro=renamevars(Data_pro,["Data_pro1","Data_pro2","Data_pro3","Data_pro4","Data_pro5"],["E_ID","Vol","VF","CVF",
"MPS"]);
writetable(Data_pro,"CFV_MPS.xlsx")
```

# Appendix C: Cumulative Fraction Volume for ICP

```
%%%%%%%%%%%%%%%%%%%%%%%%%%%%%%%%%%%%
%Negative ICP
%%%%%%%%%%%%%%%%%%%%%%%%%%%%%%%%%%%%

%Read data of ICP (Var2), Element ID (x_Eid_), and Volume(Volume)

Data=readtable('Time_Element_Pressure_Global.csv');
Data=Data(3:end,2:end);
Data=renamevars(Data,("Var2"),("x_Eid_"));
opts2 = detectImportOptions('Volume');
opts2.SelectedVariableNames = ["x_Eid_","Volume"];
Data2=readtable('Volume',opts2);
Data2=Data2(1:end-2,1:2);

%Organize data in a single table

Data_full=join(Data2,Data);
Data_full=table2array(Data_full);
MinICP=min(Data_full(:,3:end),[],2);
Data_pro(:,1)=Data_full(:,1);
Data_pro(:,2)=Data_full(:,2);

%Calculate maximum ICP by Element and simplified tab

Data_pro(:,5)=MinICP;

%Sort table by MPS

Data_pro=sortrows(Data_pro,5,'descend');

%Calculate total volume and volume fractions by element

Total_Vol=sum(Data_pro(:,2));
lim=length(Data_pro(:,1));
for i=1:lim
   Data_pro(i,3)=Data_pro(i,2)/Total_Vol;
end

%Calculate cumulative volume fraction

Data_pro(1,4)=1-Data_pro(1,3);
for i=2:lim
   Data_pro(i,4)=Data_pro(i-1,4)-Data_pro(i,3);
end

%Write results

Data_pro=array2table(Data_pro);
Data_pro=renamevars(Data_pro,["Data_pro1","Data_pro2","Data_pro3","Data_pro4","Data_pro5"],["E_ID","Vol","VF","CVF",
"NegativeICP"]);
writetable(Data_pro," CFV_NICP.xlsx")
```

```
%%%%%%%%%%%%%%%%%%%%%%%%%%%%%%%%%%%%
%Positive ICP
%%%%%%%%%%%%%%%%%%%%%%%%%%%%%%%%%%%%


%Read data of ICP (Var2), Element ID (x_Eid_), and Volume(Volume)

Data=readtable('Time_Element_Pressure_Global.csv');
Data=Data(3:end,2:end);
Data=renamevars(Data,("Var2"),("x_Eid_"));
opts2 = detectImportOptions('Volume');
opts2.SelectedVariableNames = ["x_Eid_","Volume"];
Data2=readtable('Volume',opts2);
Data2=Data2(1:end-2,1:2);

%Organize data in a single table

Data_full=join(Data2,Data);
Data_full=table2array(Data_full);
MaxICP=max(Data_full(:,3:end),[],2);
Data_pro(:,1)=Data_full(:,1);
Data_pro(:,2)=Data_full(:,2);

%Calculate maximum ICP by Element and simplified tab

Data_pro(:,5)=MaxICP;

%Sort table by MPS

Data_pro=sortrows(Data_pro);

%Calculate total volume and volume fractions by element

Total_Vol=sum(Data_pro(:,2));
lim=length(Data_pro(:,1));
for i=1:lim
   Data_pro(i,3)=Data_pro(i,2)/Total_Vol;
end

%Calculate cumulative volume fraction

Data_pro(1,4)=1-Data_pro(1,3);
for i=2:lim
   Data_pro(i,4)=Data_pro(i-1,4)-Data_pro(i,3);
end

%Write results

Data_pro=array2table(Data_pro);
Data_pro=renamevars(Data_pro,["Data_pro1","Data_pro2","Data_pro3","Data_pro4","Data_pro5"],["E_ID","Vol","VF","CVF",
"PositiveICP"]);
writetable(Data_pro," CFV_PICP.xlsx")
```

# Appendix D: Concussion Probability based on MPS and ICP

```
%%%%%%%%%%%%%%%%%%%%%%%%%%%%%%
% Concussion Probability based on MPS and ICP
%%%%%%%%%%%%%%%%%%%%%%%%%%%%%%



%Directory

file1='CumulativeMPS\CSV.xlsx';
file2='CumulativePressure\CPPV.xlsx';

%Extract maximum MPS

opts = detectImportOptions(file1);
opts.SelectedVariableNames = ("MPS");
Read=readtable(file1,opts);
Read=table2array(Read);
val=height(Read);
Data(:,1)=Read(val-9:val);

%Extract maximum positive ICP

opts2 = detectImportOptions(file2);
opts2.SelectedVariableNames = ("PositiveICP");
Read2=readtable(file2,opts2);
Read2=table2array(Read2);
val2=height(Read2);
Data(:,2)=Read2(val2-9:val2);

%Maximum Average

M=mean(Data,1);

%Concussion probability based on MPS

MPS_Concussion=1/(1+exp(-9.184*M(1)+4.195));

%Concussion probability based on ICP

ICP_Concussion=1/(1+exp(-0.02394*(M(2)/1000)+3.8606));
```

# Appendix E: Kinematic Transformation between Coordinate Systems

```
%%%%%%%%%%%%%%%%%%%%%%%%%%%%%%%%%%%%
% Kinematic Transformation between Coordinate Systems
%%%%%%%%%%%%%%%%%%%%%%%%%%%%%%%%%%%%

%Read values, note that the data was reduced to 250 ms (row 259952)

ax=readtable('TIR_8_Ax.csv');
ay=readtable('TIR_8_Ay.csv');
az=readtable('TIR_8_Az.csv');
wx=readtable('TIR_8_Wx.csv');
wy=readtable('TIR_8_Wy.csv');
wz=readtable('TIR_8_Wz.csv');
t=table2array(ax(1:259952,1));
ax=table2array(ax(1:259952,2));
ay=table2array(ay(1:259952,2));
az=table2array(az(1:259952,2));
omega_x=table2array(wx(1:259952,2));
omega_y=table2array(wy(1:259952,2));
omega_z=table2array(wz(1:259952,2));

%Initial conditions

theta(1)=0;
beta(1)=0;
alpha(1)=0;
delta_T=0.000001;
for i=1:259951

%Integrate angle

m_omega_x=((omega_x(i)+omega_x(i+1))/2)*delta_T;
m_omega_y=((omega_y(i)+omega_y(i+1))/2)*delta_T;
m_omega_z=((omega_z(i)+omega_z(i+1))/2)*delta_T;
theta(i+1)=theta(i)+m_omega_x;
beta(i+1)=beta(i)+m_omega_y;
alpha(i+1)=alpha(i)+m_omega_z;

%Rotational matrix

Rz=[1 0 0; 0 cos(theta(i+1)) -sin(theta(i+1));0 sin(theta(i+1)) cos(theta(i+1))];
Ry=[cos(beta(i+1)) 0 sin(beta(i+1));0 1 0; -sin(beta(i+1)) 0 cos(beta(i+1))];
Rx=[cos(alpha(i+1)) -sin(alpha(i+1)) 0; sin(alpha(i+1)) cos(alpha(i+1)) 0; 0 0 1];
R=Rx*Ry*Ry;

%Rotate the linear accelerations and rotational velocities

a=[ax(i) ay(i) az(i)];
omega=[omega_x(i) omega_y(i) omega_z(i)];
a=transpose(a);
omega=transpose(omega);
Ra=R*a;
Ra=transpose(Ra);
Rw=R*omega;
Rw=transpose(Rw);
ac(i,1)=t(i);
ac(i,2)=Ra(1);
```

```
ac(i,3)=Ra(2);
ac(i,4)=Ra(3);
ac(i,5)=Rw(1);
ac(i,6)=Rw(2);
ac(i,7)=Rw(3);
end

%Filter results

c=0;
for i=1:518
c=c+1;
R(c,1)=t(c*500,:)+0.009;
R(c,2)=ax(c*500,:);
R(c,3)=ay(c*500,:);
R(c,4)=az(c*500,:);
R(c,5)=omega_x(c*500,:);
R(c,6)=omega_y(c*500,:);
R(c,7)=omega_z(c*500,:);
R(c,8)=ac(c*500,2);
R(c,9)=ac(c*500,3);
R(c,10)=ac(c*500,4);
R(c,11)=ac(c*500,5);
R(c,12)=ac(c*500,6);
R(c,13)=ac(c*500,7);
end

%WriteTable

R=array2table(R);
R=renamevars(R,"R1","Time");
R=renamevars(R,"R2","ExpLax");
R=renamevars(R,"R3","ExpLay");
R=renamevars(R,"R4","ExpLaz");
R=renamevars(R,"R5","rvx");
R=renamevars(R,"R6","rvy");
R=renamevars(R,"R7","rvz");
R=renamevars(R,"R8","RotLax");
R=renamevars(R,"R9","RotLay");
R=renamevars(R,"R10","RotLaz");
R=renamevars(R,"R11","Rotrvx");
R=renamevars(R,"R12","Rotrvy");
R=renamevars(R,"R13","Rotrvz");
writetable(R,'ExpKinematics.xlsx')
```

# Appendix F: Calculating Nodal Forces

```
%%%%%%%%%%%%%%%%%%%%%%%%%%%%%%%%%%%%%%%%%%%%%%%%%%
%Calculating Nodal Forces - Sagittal
%%%%%%%%%%%%%%%%%%%%%%%%%%%%%%%%%%%%%%%%%%%%%%%%%%

%Initial variables

lax=ac(:,2); %Linear acceleration X
laz=ac(:,4); %Linear acceleration Z
av=omega_y;  %Rotational velocity Y
m=0.0589;    %Mass Sagittal model
I=0.000497;  %Inertia Sagittal model
r1=0.1315;   %First Distance Sagittal model
r2=0.0585;   %Second Distance Sagittal model
Nod=966;     %Nodes to apply force in X
Nod2=13228;  %Nodes to apply force in Z

%derivate angular acceleration

aa=diff(av)./diff(t);
aa(259952,:)=aa(259951,:);
c=0;
for i=1:259
c=c+1;
tt=t(c*1000,:)+0.009;

%Calculate forces

Fx1=((m*lax(c*1000,:)*r1-I*aa(c*1000,:))/(3*r1+r2));
Fx2=(m*lax(c*1000,:)-3*Fx1);
Fzz=(laz(c*1000,:)*m)*(-1);
F(c,1)=round(tt,4);
F(c,2)=round(Fx1,6);
F(c,3)=round(Fx2,6);
F(c,4)=round(Fzz,2);
end

%Write Table

Fdown=[F(:,1),F(:,2)/Nod];
Fup=[F(:,1),F(:,3)/Nod];
Fz=[F(:,1),F(:,4)/Nod2];
writematrix(F,'Forces.xlsx')
```

```
%%%%%%%%%%%%%%%%%%%%%%%%%%%%%%%%%%%%%%%%%%%%%%%%%%%%%%%%%%%%%%%%%%%%%%%%
%Calculating Nodal Forces - Transverse
%%%%%%%%%%%%%%%%%%%%%%%%%%%%%%%%%%%%%%%%%%%%%%%%%%%%%%%%%%%%%%%%%%%%%%%%

%Initial variables

lay=ac(:,3); %Linear Acceleration Y
rv=omega_z;  %Rotational Velocity Z
m2=0.0236;   %Mass Transverse model
I2=0.000091; %Inertia Transverse model
r12=0.09845; %First Distance Transverse model
r22=0.08645; %Second Distance Transverse model
Nod2=350;    %Nodes to apply force in Y
Nod3=7034;   %Nodes to apply force in X

%derivate angular acceleration

aa2=diff(rv)./diff(t);
aa2(259952,:)=aa2(259951,:);

%Calculate forces

c=0;
for i=1:259
c=c+1;
tt=t(c*1000,:)+0.009;
Fy1=(m2*lay(c*1000,:)*r22+I2*aa2(c*1000,:))/(3*r22+r12);
Fy2=m2*lay(c*1000,:)-3*Fy1;
Fxx=(lax(c*1000,:)*m2);
F(c,1)=round(tt,4);
F(c,2)=round(Fy1,6);
F(c,3)=round(Fy2,6);
F(c,4)=round(Fxx,2);
end

%Write Table

FF=[F(:,1),F(:,2)/Nod2];
FB=[F(:,1),F(:,3)/Nod2];
Fx=[F(:,1),F(:,4)/Nod3];
writematrix(F,'Forces2.csv')
```